UNIVERSITY OF CALIFORNIA

Santa Barbara

Probing Quantum Condensed Matter Through the Polarimetry of High-Order Sidebands

A dissertation submitted in partial satisfaction of the

requirements for the degree Doctor of Philosophy

in Physics

by

Seamus D. O'Hara

Committee in charge:

Professor Mark S. Sherwin, Chair

Professor Andrea Young

Professor Cenke Xu

June 2023

The dissertation of Seamus O'Hara is approved.

_____

Prof. Andrea Young

_____

Prof. Cenke Xu

_____

Prof. Mark S. Sherwin, Committee Chair

Dedicated to the loving memory of Michael James Gade,

who taught me science without heart and joy is not science

worth pursuing.

Forever 57

Acknowledgements

To Beau, the best writing partner I could imagine.

To Demi - Σ'αγαπώ αγάπη-μου

To my parents, who always let me dream.

To (Dr!) Joe Costello, the Lennon to my McCartney.

The work in this thesis would not be possible without the leadership and insight of my advisor, Prof. Mark Sherwin, and our theoretical collaborator, Dr. Qile Wu. We wouldn't be able to see all of the wonderful sidebands presented in this thesis without the FEL, which was lovingly maintained by Dr. Nick Agladze and Dave Enyeart during my tenure at the ITST. Lab wouldn't have been half as rewarding if it were not for my wonderful lab mates throughout the years: Moonsuk Jang, Brad Price, Mathilde Papillion, Dr. Antonín (Tonda) Sojka, Dr. Blake Wilson, Dr. Darren Charles Valovcin, Dr. Xiaoling (Cocoa) Wang, Dr. Marzeih Kavand, and Dr. Changyun Yoo. During my time I had the honor of working with some gifted undergraduate and high-school students. The work of Alex Peñaloza, Audi Sewal, and Kara Chatterton helped make this thesis possible.

Moon, the future belongs to you. Let it rip.

As California has become the home for me and Demi over the past six years, so many people have been major parts of our lives. Thank you all for making our time here so pleasant. Thank you in particular to my PhD cohort; we all made it through together, and are stronger because of it.

Before my time at UCSB, the care and attention of Profs. Jie Shan, Kin Fai Mak, and Jieun Lee helped me develop into someone who was moderately useful in a lab. Along with the mentorship of the Shan/Mak group at Penn State, these three helped me prepare for graduate school, allowing me to contribute to all the research presented in this thesis. My graduate studies, the work presented in this thesis, and my future scientific career would not be possible without their generosity.

Finally, thank you to my original Physics teachers, Mr. Hermann and Mr. Celona, who helped me channel my energy and curiosity into what is now my career. Thank you

to the many other teachers in the Springfield public school system who helped me grow into the scientist and person I am today. Thank you to my original lab mates: Mike Gade (MUG, EDP, Dream Team), Alex Poplowski (Dream Team), and Capt. Michael Astrino (MUG, EDP).

Curriculum Vitæ

Born — May 12th, 1995

Bryn Marw Hospital, PA

Education:

B.S., Physics and Mathematics (Aug 2013 – May 2017) The Pennsylvania State University

Cum Laude, Schreyer Honors Scholar

Thesis: "The Optical Observation of Charge Carriers in Tungsten Diselenide"

Advisors: Jie Shan and Kin Fai Mak

PhD, Physics – (Sept 2017 – June 2023) University of California, Santa Barbara

Advisor: Prof. Mark Sherwin

Experience:

Instructor —

Physics 23 (Summer 2022) Mechanical waves, sound, and electrostatics.

Physics 106 (Spring 2023) An introduction to nonlinear phenomena and chaos.

Graduate Research Assistant (2018 – present)

Teaching Assistant (2017 – 2018)

Undergraduate Research Assistant – (2015 – 2017) Worked with Profs. Jie Shan and Kin Fai Mak in their Experimental Condensed Matter group at PSU, using optical and electrical measurements to observe properties of charge carrier in two dimensional Transition Metal Dichalcogenides.

Publications:

S. O'Hara et al. "Bloch Wavefunction interferometry of driven quasiparticles in bulk GaAs" *Submitted* https://arxiv.org/abs/2305.12245

J. Costello*, S. O'Hara*, Q. Wu*, et al. "Reconstruction of Bloch wavefunctions of holes in a semiconductor" *Nature*, **599**, 57-61, (2021)

Press:

"In a First, Physicists Glimpse a Quantum Ghost" *Scientific American* (Dec 8th, 2021)

"Measuring Bloch Waves" *Research in 60 seconds, UCSB* (May 17th, 2022)

J. Costello, S. O'Hara et al. "Temperature dependent characterization of quasiparticle dephasing in semiconductors" *Prepared for Submission*

S. O'Hara et al. "Dynamical gap measurement of quasiparticles in a semiconductor" *In Preparation*

Fellowships:

Intelligence Community Post-Doctoral Research Fellowship —(Oct 2023 — Oct 2025) Amount awarded: $102,000 annually.

Supports unclassified basic research in areas of interest to the IC. Funded primarily by the Office of the Director of National Intelligence, the Program annually supports several Postdoctoral Fellows from U.S. accredited colleges, universities, and U.S. Government laboratories across the country.

Conference Proceedings:

J. Costello*, S. O'Hara*, Q. Wu*, et al. "Experimental Hamiltonian Reconstruction via Polarimetry of High-order Sidebands in a Semiconductor" Conference on Lasers and Electro-Optics (CLEO), *OSA Technical Digest* (Optical Society of America, 2022), **FTu5B.3**

S. O'Hara et al. "Measuring Luttinger Parameters Directly form Quasiparticle Dynamics" in CLEO, *OSA Technical Digest* (Optical Society of America, 2021), **paper JTu3A.62**

S. O'Hara, J. Costello, Q. Wu, et al., "Reconstructing Bloch Wavefunctions in GaAs through High-Order Sideband Polarimetry," CLEO, *OSA Technical Digest* (Optical Society of America, 2020), **paper FF2Q.3.**

Presentations:

NSF Quantum Foundry Seminar – "Polarization of High Order Sidebands: Probing the Dynamics and Interference of Coexisting Quantum States" (peer-to-peer seminar, *2022*)

Optical Terahertz Sciences and Technology Conference (OTST) – "Reconstruction of the Effective Hamiltonian of Holes in Bulk GaAs" (talk, *2022*)

APS March Meeting – "Reconstructing the Effective Hamiltonian of Hole in Bulk GaAs from Polarization of High Order Sidebands" (talk, *2022*)

CLEO – "Measuring Luttinger Parameters Directly from Quasiparticle Dynamics" (poster, *2021*)

Lunch and Learn – "Reconstructing the Quantum Behavior of Particles in Materials" (Graduate student peer-to-peer talk, *2021*) https://vimeo.com/524025092

CLEO – "Colliding Electrons and Holes to Reconstruct Their Bloch Wavefunctions" (talk, *2020*)

OTST – "Sensitivity of High Order Sideband Generation to Strain" (poster, *2019*)

Mentorship:

NSF Quantum Foundry Internship Program (Summer 2021) – Assembled a 10 week research project for a college student. During the 10 weeks Audri Sewal developed a Python analysis package for new experiments being conducted in the summer of 2021, and shadowed experiments.

Apprentice Researchers (Summer 2019) – Mentored a high school student for 6 weeks in an effort for the student to become familiarized with a university research lab.

Alex Peñaloza (2019 – '20) – Oversaw and worked alongside Alex with the task of machining and installing a new cryogenic test chamber for the HSG experimental setup.

Abstract

Probing Quantum Condensed Matter Through the Polarimetry of High-Order Sidebands

By Seamus D. O'Hara

Quantum mechanics views particles as matter waves rippling through space, and when there are many of these waves present in the same system, they can interfere with one another. While quantum mechanics make the direct measurement of a particular wave function's phase impossible, clever experiments can probe the interference of wave functions with different phases. High Order Sideband Generation (HSG) is an optical method which uses two frequencies of light to both excite quasiparticle-antiquasiparticle pairs and accelerate them through the Brillouin Zone. In the experiments detailed in this thesis, a near infrared (NIR) laser creates electron-hole (e-h) pairs in bulk Gallium Arsenide (GaAs). A strong Terahertz (THz) electric field ionizes the e-h pair, accelerates the pair to a higher energy, and slams the pair back together to have the e-h pair annihilate and emit a photon. Because the pair will gain energy from the THz acceleration process, the photon emitted by their annihilation will be offset in energy from the initial NIR excitation energy; a high order sideband.

While the THz is accelerating the e-h pairs, the holes can be in one of four angular momentum eigenstates which exists in the valence band of bulk GaAs. The distribution of e-h pairs in the four states is determined by the Bloch wave functions and effective Hamiltonian of the valence band, called the Luttinger Hamiltonian. By the conservation

of angular momentum, a given hole will produce a sideband with a specific polarization, and the total polarization of sideband photons at a given energy can be related to the Bloch wave functions. The reconstruction of Bloch wave functions in bulk GaAs is detailed in this thesis. The change in polarization as a function of sideband energy is presented as an interferogram. Analogous to a Michelson interferometer for Bloch waves, signal is connected to the difference in dynamical phase accrued by different quasiparticles being accelerated by the THz field. A classical model of the quasiparticle trajectories leads to an analytical theoretical calculation of the sideband polarization, which is in good quantitative agreement with experiment. The sideband polarization dependence on the initial energy of the NIR excitation photons is probed, and preliminary analysis of the dynamical gap of the driven quasiparticles yields a value of $E_g = 1.511$ eV. In addition, the sideband polarization can be related to the effective Hamiltonian and the dispersion relation of the quasiparticles in bulk GaAs.

Beyond the experiments detailed in this thesis, HSG offers the opportunity to characterize the Bloch wave functions, effective Hamiltonians, and dynamical phases of more exotic quasiparticles and more exotic materials. With this thesis acting as a proof-of-concept for the HSG polarimetery methodology, the ambition is to extend this method to highly correlated systems or semiconductors with large spin-orbit coupling, or to measure geometric phases, indicative of non-trivial topologies.

Chapter 1 — Introduction

Quantum mechanics describes all matter as waves, propagating through space and time. Mathematically, we would express the oscillating, wave-like features of a particle's propagation with complex numbers and exponentials, writing an expression like

$$\Psi(x,t) = \psi(x)e^{i\phi(t)} \tag{1.1}$$

Here we express the function which determines the probability of finding a particle at position x at a time t with Ψ, representing it as a product of function dependent on position $\psi(x)$ and a complex exponential expression $\exp[i\phi(t)]$ [1]. We would call $\phi(t)$ the phase of this wavefunction. This phase does most of the work describing the propagation of the overall wave Ψ relative to itself and other waves. In the process of a quantum measurement, this phase gets ironed out. Along with the collapse of the

wavefunction, this loss of phase is one of the more frustrating differences between how we theorize and explain the behavior of particles and what we can actually observe.

Whereas the quantum wavefunction phase is frustratingly inaccessible to experimentalists, measuring the phase of an electromagnetic wavefront, or light, is a classical one. This experimental method of resolving the polarization of an electric field is called *polarimetry*, and will be utilized in all the experiments presented in this thesis. Experimentalists are able to measure the magnitude and phase of an electromagnetic field up to some arbitrary phase, which is the gauge freedom of the electric field.

If there was a quantum process which ends with the emission of a photon, we could measure the phases of electromagnetic fields through well established methods and try to connect this to the phase of the wavefunctions producing the light. To do this, there needs to be a theory connecting the two. Additionally, multiple wavefunctions and multiple electromagnetic fields need to be present in the system in order to measure the interference of these waves. In this way we propose a simple solution to the impossible problem.

> *Simple Solution* — Interfere two or more wavefunctions, and use well established optical methods, which can clearly resolve the phase of an electromagnetic wave, to measure this interference. In this way we can access phases information about the wavefunction, a seemingly impossible problem.

In solids, where there are 10^{23} wavefunctions, there are many opportunities for these waves to interfere. The question becomes how to observe systematic inference patterns among these waves, or induce states in the solid where there is clearly resolvable interference pattern. STM experiments reported observations of interference between matter waves in solids [2-4]. Effects resulting from weak Anderson localization also demonstrate interference phenomena among solids [5]. While these experiments provide insight into the collective behaviors of electrons in solids near the equilibrium state, we are limited in what we can learn about individual electronic wavefunctions.

In solids the particle-to-crystal lattice dephasing decreases the fidelity of electronic wavefunctions on timescales much faster than conventional consumer electronics ($\omega < 5\text{GHz}$). If we want to measure the quantum states with a high fidelity, we need experiments which occur on timescales faster than dephasing processes. In the first section of this introduction, I will outline ultrafast experiments in solids which are conducted on timescales faster than these dephasing processes. However, the large laser fields in these experiments excite many, many wavefunctions for a given experiment, making it difficult for any one experiment to give us a clear measurement of the single-particle wavefunction.

In order to for optical experiments and polarimetry to play a role in our quantum experiment, there needs to be some physical process which produces light. This thesis focuses on one such phenomena occurring in solids, called High-order sideband generation (HSG). In the second section of this introduction, I will build a model for how we generate photons from a non-equilibrium condensed matter experiment, and how the

microscopic physics of the particles driven from equilibrium is embedded in the outgoing sideband polarization.

To conclude this chapter, I describe the source of THz radiation used in all these experiments. The free electron laser (FEL) at UCSB is a unique source of THz radiation which enabled the particulars and subtleties of experiments detailed in this thesis. As the upkeep and operation of the FEL has fallen more and more on graduate students, outlining the art of FEL maintenance is essential for the continuation of experimentation by future graduate students.

1.1 DRIVEN QUANTUM MATTER

Before the experiments detailed in this thesis, there were many reported examples of interferometry in solid state systems. For example, the advent of strong, ultrafast electromagnetic field enabled experiments like High Harmonic Generation (HHG) in solids [6-8]. Strong, periodic driving is also the focus of Floquet engineered systems, which manifest new collective phases of matter under this driving force. While both types of experiments illuminate the behavior of condensed matter systems far from equilibrium, [9] both are difficult to understand in the single-particle picture. While non-equilibrium quantum matter comes in many forms, the focus of this thesis is the ability of experiments to tell us more about the constituent wavefunctions of the system and their effective Hamiltonian. The control of the wavefunction is the next major task of the quantum age; first scientists must learn more about the wavefunctions we are attempting to control to achieve success.

1.1.1 Ultrafast Experiments in Matter

Developments in strong laser field experimentation have allowed for the coherent acceleration of quasiparticles in solids on the attosecond to picosecond timescale [10, 11], faster than dephasing processes in solids. HHG is an all-optical probe which employs a single frequency laser with a high field strength, exciting states in a system and accelerating them to higher energies, which leads to the emission of harmonics. In solids [12-22] HHG allows for attosecond sensitivity to dynamics of electrons in these systems [23, 24], and has demonstrated sensitivity to quasiparticle/crystal interactions [7, 8, 25, 26].

The large laser fields used to generate these harmonics produce interband and intraband currents, both of which contribute to the HHG signal [27-29]. HHG is a fantastic demonstration of ultrafast light-matter interaction as a probe for quantum systems, however, the high laser fields which enable this probe ultimately complicate the physical picture of the system. This limits its effectiveness in resolving contributions from individual wavefunctions. As will be demonstrated in the subsequent chapters, the two frequency nature of HSG avoids this problem.

1.1.2 Floquet Engineered Quantum States

Driven quantum systems have occupied the attention of the experimental and theoretical community [9, 30] for the ability to manifest non-trivial, non-equilibrium phases of matter [31]. Driven Floquet-Bloch bands as the result of ultrafast drives have been observed in topological insulators [32, 33], and flat bands have been theorized to exist in driven graphene systems [34].

In general, these systems form non-equilibrium Fermi-seas, which produce emergent phenomena for collective quantum states. While the phenomena induced by this Floquet engineering cannot be observed in the equilibrium state of a system, these experiments do not provide insight to the single particle wavefunctions. Experiments with greater control over constituent wavefunctions are necessary for the next-generation quantum systems to be built. In the next section, I will detail HSG as one of these systems, and use the rest of the thesis to elaborate what can be learned from experimentation.

1.2 HSG IN BULK SEMICONDUCTORS

In condensed matter systems, as in many physical systems, there exists more than one relevant energy scale. For example, the energy required to create an excited state for a conventional semiconductor normally resides in the optical region, but the energy scale for the dispersion relation of quasiparticles in this semiconductor is in the μeV to meV region. Experiments like HHG, which only use one frequency of light, are limited to focusing on only one of these scales. However, an experiment which uses two frequencies, like High-order sideband generation, is able to probe these energy scales of disparate size.

Like HHG, HSG can be broken down into three steps [35-37]. There is a general description of the phenomena, and a more specific description of the experiments conducted in this thesis, and I will outline both in this section. The general case is intentionally broad in an effort to emphasize the large number of systems on which HSG

experimentation *could* be conducted. The specific case will provide a more detailed picture and intuition for the experiments included in this thesis. After this section, the specific nature of the HSG experiments conducted will dominate the text. The general case of HSG will be revisited at the end of the thesis

1.2.1 Three Step Model

Generally, the phenomena of HSG in a condensed matter system can be described in the three steps: excitation, acceleration, and annihilation.

Excitation: Laser light with photon energy $\hbar\Omega$ creates an excited state in the system with the same creation energy. I will call this the creation field. This ground state will consist of the excited quasiparticle and an anit-quasiparticle left behind in the vacated state.

Acceleration: A second laser, with photon energy $\hbar\omega$ and significantly greater peak field strength, rips apart the bound state of the quasiparticle pair. I will call this the acceleration field because it accelerates the quasiparticle and anti-particle. The two move in opposite directions due to their opposite charge. During this acceleration process, the effective Hamiltonian of the system will govern how the quasiparticle wavefunctions move through the condensed matter system.

Annihilation: The polarity (sign) of the acceleration field changes sign, driving the quasiparticle and anti-quasiparticle back together, where they annihilate. The pair will have gained kinetic energy during the acceleration process, meaning the photon they emit upon annihilation will be offset from the initial creation energy,

$\hbar\Omega$, by a multiple of the acceleration field's photon energy, $n\hbar\omega$, for a photon energy with total energy $\hbar(\Omega + n\omega)$.

This model sets specifications of what lasers can be used for HSG experimentation in a particular system. Constraints on the creation field are mostly to simplify the physics of the systems probed. For all the data presented in this thesis, we assume no Coulomb interactions between the different quasiparticle pairs created by the creation field. For this to be true, the field strength must be low enough for HSG experiments to be in the *linear response regime* of the creation field. This is verified experimentally by measuring the intensity of low order sidebands with respect to creation field strength. If the increases in field strength leads to a proportional increase in sideband signal, then the increasing number of quasiparticle pairs created by stronger and stronger creation fields does not dampen the sideband signal [38]. For materials with larger binding energy like two dimensional semiconductors, Coulomb interaction is an important force to consider [39-41]. However, we can say Coulomb interaction is not relevant to the HSG experiments presented in this thesis and other HSG works.

With this enforced maximum on the creation field, we can say most of the quasiparticle excitation processes are single photon processes. This is a distinction between HSG and HHG. Later on, when we examine the sideband data and develop a theoretical model to describe the experimental data, we shall see this single photon creation process will greatly simplify the non-equilibrium physics at hand, to the point

where analytical models will provide a strong quantitative agreement between experiment and theory.

1.2.2 Solids in Large, Fast Electric Fields

The field strength of the acceleration field must be large enough to ionize the pair and drive the two around the crystalline lattice. For an oscillating electric field, the average kinetic energy imparted on a particle with fundamental charge *e* in a single cycle is called the *ponderomotive energy*, U_p, derived from the expression

$$U_p = \left\langle \frac{1}{2}\mu v^2 \right\rangle \tag{1.2}$$

Here μ is the reduced mass of the quasiparticle pair. Using the kinematic expression $\dot{v}(t) = a(t) = F(t)/\mu$, the expression for the electrostatic force, and representing the electric field of the accelerating field as $E_{acc}(t) = F_{acc}\sin(\omega t)$, where F_{acc} is the peak field strength of the accelerating field, we can derive an expression for the velocity of the charged particle

$$v(t) = \frac{e^2 F_{acc}^2}{\mu\omega^2}\cos(\omega t) \tag{1.3}$$

Here *e* is the charge of the particle being accelerated. With this expression, we can express U_p as

$$U_p = \frac{e^2 F_{acc}^2}{2\mu\omega^2}\left(\frac{\omega}{2\pi}\int_{-\pi/\omega}^{\pi/\omega}\sin^2(\omega t')dt'\right) = \frac{e^2 F_{acc}^2}{4\mu\omega^2} \tag{1.4}$$

The expression in parenthesis evaluates to 1/2. With this expression for ponderomotive energy in terms of the accelerating field parameters, F_{acc} and ω, and the quasiparticle pair

parameters, μ and e, we can set an explicit condition for the field strength of the accelerating field. As a general rule, the quasiparticle pair will not be accelerated semi-classically through the crystal, and thus not produce high-order sidebands, unless $U_p > 2 \cdot E_{bind}$, [42, 43] therefore,

$$F_{acc} > \sqrt{\frac{8E_b \mu \omega^2}{e^2}} \tag{1.5}$$

For HHG, this expression is also true, however, due to the single-frequency nature of HHG experimentation, this field strength is also the creation field, which normally implies the creation field is not in the single-photon excitation regime.

There are a few features of Eq. 1.5 which are worth dwelling on, as they provide insight onto the types of condensed matter systems and lasers which are conducive to HSG experimentation. For the following analysis, consider F_{acc} is constant:

The dependence on μ - The larger the effective mass of the quasiparticle pair, the larger the required F_{acc}.

The dependence on ω - The higher the frequency, the higher the requisite F_{acc}. This creates an upper-bound on the frequencies used for HSG experimentation, assuming a constant F_{acc}.

The dependence on binding energy - As one might expect, the binding energy sets a minimum threshold for F_{acc} required to observe sidebands. For systems, such as two dimensional semiconductors, which hosts excitons with binding

energies an order of magnitude larger than their III-V counterparts [44-52], HSG experimentation requires larger F_{acc}.

With these conditions met, the accelerating field drives the quasiparticle pair to higher energies non-perturbativly, i.e subsequent pairs which are driven to higher energies decrease in population sub-exponentially. This manifests in the resulting sideband spectrum with decreasing peak intensities as a function of sideband order less rapidly than perturbation theory would predict [35, 36, 53-55]. Semiclassical propagators, as will be introduced in Chapter 3, better model the population of quasiparticle pairs driven to higher energies. Because of this, HSG is considered a non-equilibrium, non-linear, non-perturbative process.

1.2.3 Experimentally Specific Three-Step Model

Now that we have a general intuition for the constraints on HSG experimentation, it is time to discuss the three step method for specific experiments conducted in this thesis. This begins by looking at the crystalline system used to generate the sidebands, bulk Gallium Arsenide (GaAs).

GaAs has a direct band gap at the zero quasi-momenta (k) point in the Brillouin Zone (BZ), labeled the Γ point. There is an energy gap of 1.519 eV between the lowest energy unfilled band (conduction band) and the highest energy fully-filled band (valence band) at the Γ point at 0 Kelvin [44]. Furthermore, the valence band at the Γ point is doubly degenerate, with the two bands often labeled heavy hole (hh) or light hole (lh), due to the different dispersion relations and effective masses the bands posses moving

away from the Γ point. Like all crystalline materials, quantum mechanics in the form of Bloch's theorem well-describes the behavior of quasiparticles in these bands. However, scattering induced by phonons and crystal impurities cause these pure quantum states to decohere on the order of picosecond (10^{-12}). Therefore, we need an acceleration field which produces high-order sidebands on timescales shorter or comparable to this dephasing timescale. This leads to the following picture for HSG experiments conducted in our lab:

Excitation: We use near-infrared (NIR) lasers tuned to the energy gap of bulk GaAs in order to resonantly excite electrons from the valence band to the conduction band. In the valence band, the recently vacated electron state now behaves like a positively charged electron, called an electron-hole (hole). Due to the degeneracy at the Γ point, both hh and lh states are formed by this excitation. The electron (e) excited to the conduction band forms a bound, excitonic state with its partner hole state.

Acceleration: We ionize the excitons with a large terahertz (THz) field generated by the UCSB Free Electron Laser (FEL) facility. The details of this THz field and the FEL will be detailed in the next section. Due to their opposite charge, the electron and hole will be accelerated in opposite directions by the THz field. While they are no longer in an excitonic state, the electron and hole's dynamics are still correlated, and from this point are referred to as an *electron-hole pair* (e-h pair). The dynamics of the e-h pair through the GaAs are determined by their

effective Hamiltonian. The specific Hamiltonian of e-h pairs in bulk GaAs will be explained further in the next section.

Annihilation: Due to the ultrafast nature of the quasiparticle acceleration by the THz field, compared to the timescale of scattering dynamics in bulk GaAs, many e-h pairs will be driven apart and back together before their wavefunctions dephase. These quasiparticles produce sidebands, which in turn can be studied to reconstruct the dynamics and quantum properties of these quasiparticles in the GaAs crystals.

From this specific picture we can start to see how HSG provides a platform for ultrafast, all-optical, non-equilibrium experimental probe of the quantum behavior of electronic states in condensed matter systems. A large portion of this quantum behavior is parameterized by the effective Hamiltonian of the quasiparticle/crystalline system, which, for the conduction electrons, hh, and lh states in bulk GaAs, is the Luttinger Hamiltonian.

1.2.4 GaAs and the Luttinger Hamiltonian

The bulk GaAs samples we use in HSG experiments come from a wafer grown via molecular beam epitaxy (MBE). Through a controlled process which consists of depositing layers of Gallium and Arsenide atoms one atomic layer at a time, our collaborators are able to grow ultra-pure crystalline lattices, which greatly simplifies the physics of our experiments. By properly choosing the substrate on which the GaAs crystal is grown, our collaborators define the orientation of the crystal on our wafer. For

the experiments in this thesis, we used a GaAs wafer with face orientation (100) pointing out from the growth direction.

GaAs is a member of the III-V semiconductor family, a class of materials which are insulators by nature but have band gaps in the optical frequency range. III-V semiconductors have been widely studied for decades due to their use in conventional semiconductor electronics and optical systems [45]. Early on, Luttinger and Kohn [56, 57], among other scientists, developed a theory of the electronic structure of these materials.

Utilizing a perturbative method called k*p theory (read *k dot p*) and the symmetry of the III-V crystals, they were able to derive a general effective Hamiltonian for this class of materials [38, 58-62]. The resulting Hamiltonian is a reduction of the eight band Kane Hamiltonian of zinc-blend crystals. Therefore, this Luttinger Kohn effective Hamiltonian describes quasiparticle interactions with the III-V lattice in the two highest energy valence bands (hh and lh) and the conduction band (e). The valence band effective Hamiltonian looks like:

$$H_v(\mathbf{k}) = \frac{\hbar^2}{2m_0}\left(\left(\gamma_1 + \frac{5}{2}\gamma_2\right)k^2 - 2\gamma_3(\mathbf{k}\cdot\mathbf{J})^2 - 2\left(\gamma_3 - \gamma_2\right)\left(k_x^2 J_x^2 + k_y^2 J_y^2 + k_z^2 J_z^2\right)\right) \tag{1.6}$$

Here the three scalar parameters $\gamma_1, \gamma_2, \& \gamma_3$ are called the Luttinger parameters and are specific to a given material, m_0 is the bare electron mass, and J_i are the 4x4 spin 3/2 matrices [58, 61].

Looking at the three terms of the Hamiltonian, the first is the normal k^2 dependent dispersion relation, the second is a spherically symmetric spin orbit coupling (SOC) term. The third breaks continuous rotational symmetry and introduces the cubic symmetry of the Ga and As sub lattices with an additional SOC term. The Luttinger parameters $\gamma_1, \gamma_2, \& \gamma_3$ moderate the contributions of these terms, which determines the dispersion relation and wavefunctions for a given material [45].

In HSG, the conduction band of the Kane model for an 8 band system describes the dynamics of the electron portion of our e-h pair [58]. This Hamiltonian is a typical k^2 dispersion relation of a free particle, but with the conduction band mass of the electron in Bulk GaAs, m_c, as opposed to the free electron mass, m_0.

$$H_c(\mathbf{k}) = \frac{\hbar^2 k^2}{2m_c} \tag{1.7}$$

The measurement of this m_c value can be measured through cyclotron resonance, and for bulk GaAs is a well known value, quoted at $0.063 \cdot m_0$ [44].

The valence Hamiltonian can be simplified under the assumption $k_z = 0$, allowing the 4X4 spin 3/2 matrices to be represented by the 2X2 Pauli spin matrices. The reduced form breaks the nonzero components of the Hamiltonian into two 2X2 blocks [58, 61-63], denoted by $s = +, -$

$$H_{v,s}(\mathbf{k}) = \frac{\hbar^2 k^2}{2m_0} \left(\gamma_1 \tau_0 - 2\gamma_2 \mathbf{n}_s \cdot \tau\right) \tag{1.8}$$

Here τ_0 is the identity matrix, τ_i are the Pauli spin matrices, m_0 is the bare electron mass, and

$$\mathbf{n}_{\pm}(\theta) = \left[\frac{\sqrt{3}}{2}\sin(2\theta), \mp\frac{\sqrt{3}\gamma_3}{2\gamma_2}\cos(2\theta), -\frac{1}{2}\right] \tag{1.9}$$

The eigenstates of these blocks are $\left|\pm 3/2\right\rangle$, $\left|\mp 1/2\right\rangle$, which form e-h pairs with the $\left|\mp S\right\rangle$ electron state in the conduction band. In this way, each block of the Hamiltonian can be viewed as the electron-hole states created for a particular electron state when excited below the resonant energy of the band gap.

By exciting our e-h pairs with NIR frequencies lower than the band gap in bulk GaAs, we can experimentally create the conditions for the block diagonal Luttinger Hamiltonian to be a good description of the dynamics of our quasiparticles through bulk GaAs. For the rest of this thesis, I will be using various experimental data to learn features of this Hamiltonian and the quasiparticle dynamics as they are driven by large electric fields.

1.3 THE FREE ELECTRON LASER

The quasiparticles producing the HSG photons are accelerated by THz radiation generated by the FEL facility at UCSB [64]. Even among FELs, the UCSB FEL is a unique source of THz radiation [65-71], which enables the particular HSG experiments detailed in the rest of this thesis. First I will detail *how* THz is generated by the FEL, and in so doing explain *why* the FEL produces radiation unique to its peer group.

1.3.1 Relativistic Electron Beam Generating Radiation

THz is generated in the FEL by using a magnetic field to wiggle (or accelerate) electrons of the free variety. For the FEL to output coherent radiation like that of a solid

state laser, the beam of free electrons needs to be energetic enough in order for the radiative gain in the cavity to outweigh losses.

Without belaboring the exact beam energies required to produce high gain THz radiation, we will take the need for relativistic electron beams for granted. What has not been taken for granted are how the relativistic electron beams are produced, and how FEL operators guide the beam to the lasing cavity.

To begin, we generate the high energy electron beams with an electrostatic gradient which can be tuned up to 4.5 MV. The "accelerator" is what we call the component containing this large electrostatic gradient and electronics which shape the temporal and spatial nature of the electron beam. Since we are accelerating free electrons with this gradient, this means the electron energies top off at 4.5 MeV, in the relativistic limit. For perspective, CERN is currently operating in the 10 TeV regime, or $2 \cdot 10^6$ larger energies, with a full time staff $2 \cdot 10^3$ larger than our own. To create the electrostatic environment used in the FEL, you would need one million commercial DC batteries wired in series. So the FEL operates between a conventional, consumer grade electrostatic environment and the highest energy environment produced on Earth. A more apt comparison for the energy scale is lightning, which also presents an engineering challenge for the accelerator. The accelerator needs a more inert environment than air, because air will breakdown at the voltages at which we hold the accelerator. As a result, the FEL accelerator is filled with SF_6, held at a pressure of 70 psi, which is less prone to electrostatic breakdown compared to ambient conditions. With all this in place, we are able to produce pulses of our relativistic electron beams.

Unlike linacs, which are often employed to produce x-ray and THz radiation, the FELs utilize a closed-cycle electrostatic environment. This greatly reduces the necessary power consumption and geographical footprint when compared to other radiative sources [64], however, it most notably caps the peak output power and repetition rate of the source. One limits the other, as, in order for the beam to reliably recirculate for each THz pulse, the quasi-dc electronics need to regain the operating potential before each pulse.

This places a great emphasis on precisely guiding the electron beam through the beam line. Two conventional magnetic components are used for such a task. The first is a steering coil, which is more or less a pair of Helmholtz coils arranged with orthogonal magnetic fields, used to deflect the electron beam in the x or y direction. The second is a quadrupole, which uses current running through four loops to create a magnetic field, used for shaping the beam. Both have local magnetic environments modulated by the amount of current running through their coils, which in turn can be controlled by an end user in the control room. The directing and shaping of this electron beam is directly dependent on the energy of the electron beam. As a result, the electrostatics in the accelerator need to be operating consistently in order for the beam to be reliably steered by the magnetic components.

Using these magnetic components, the electron beam can be steered through the beam line such that the electron beam is focused at the center of the lasing cavity of the FEL and the beam is still making a roundtrip through the entire beam line. The former is monitored with metallic screens which are inserted into the beam line and fluoresce where they are hit by the electrons. This fluorescence is imaged by CCD cameras for

monitoring. The latter is measured by the amount of electrons which return to the electrostatic components at the to the accelerator, reported through the voltage measured on the corona triode.

Going back to the UCSB FELs utilization of a closed cycle electrostatic environment, this measurement on the corona triode is equivalent to how stable the electrostatics of the accelerator are under the current operation of the FEL. When the electrostatics are unbalanced, the FEL will electrostatically discharge, or “arc”, as it is often referred to among users. This arc is the equivalent to a lightning bolt going off somewhere in the FEL, which, for obvious reasons is something we want to avoid.

Figure 1.1 shows the consequences of both a single arc and repeated arcs displayed on a copper plate which was in the beam line. The singular lines are produced by the relativistic electron beam momentarily pulsing at a lower energy after an arc, and as a result taking a drastically different path. This “drastically different path” intersects with the copper plating running throughout the beam path, scraping off copper in the process. The hole is the product of many arcs over the decades; eventually the electron beam punctured a hole in the beam path. This catastrophe brought all the components to ambient condition, destroying all the equipment operating at high vacuum like the ion pumps and cathode, or electron source. This event is often recognized as the most catastrophic event to occur in the FEL facility.

Given the engineering constraints and limitations of this closed cycle, relativistic electron beam, care is taken by the research staff to insure the electron beam is properly recirculating at a lower electron beam pulse width. This reduces the instability of the

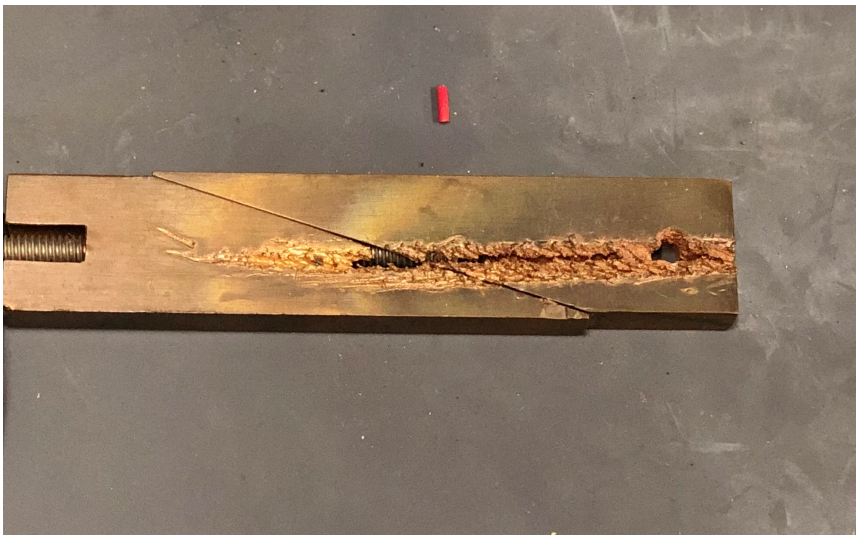

Figure 1.1 - Catastrophic E-Beam Degradation of a Copper Plate
A copper component which was a part of the electron beam transport system, near the accelerator tube. Scrapes are the result of errant electron beam pulses after an arc, and the hole on the right is the result of an electron beam which punctured the copper plate and exposed the entire electron beam path, including the cathode, to ambient conditions.

accelerator's electrostatic environment, making the system more tolerant to imperfections and reducing the possibility of an arc. In this less volatile environment, the magnetic components are tuned outside the vault. Decades ago, the current in these magnetic components were controlled via analogue dials, with FEL operators tuning components by hand and writing historically successful values down on notepads (see the upper image of Figure 1.2). Nowadays, a PC talks to the magnetic components using NI Fieldpoint firmware and software written on NI LabVIEW. (See the lower image of Figure 1.2 for an example) Given the obsolesce of Fieldpoint on the more current versions of LabVIEW, an update to the LabVIEW version on the control PC would be catastrophic, cutting off all communication between the PC and components in the vault.

Using the florescent screens placed strategically throughout the beam path, FEL users tune the beam to match historical images of the electron beam which have been

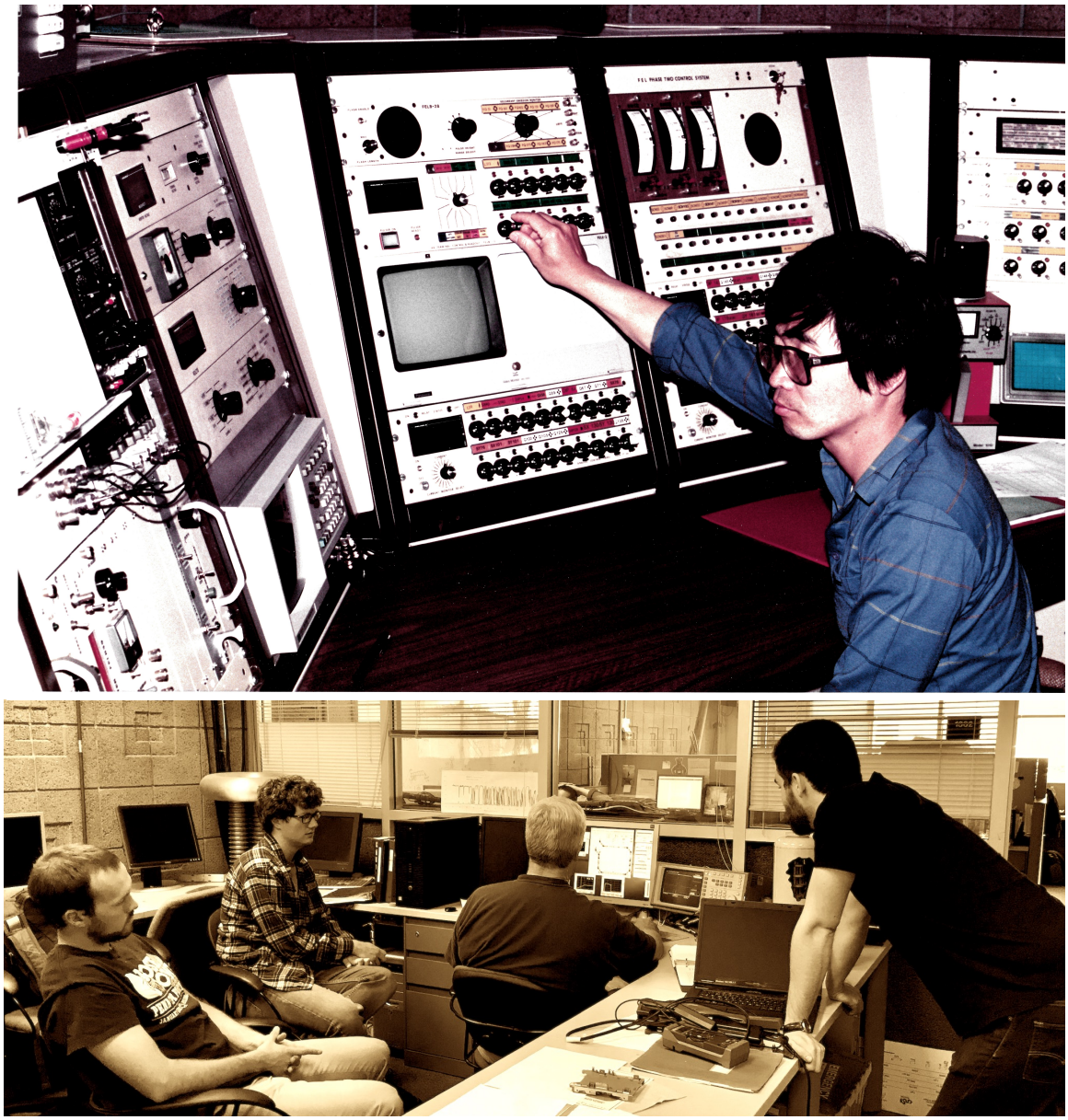

Figure 1.2 - Analogue and Modern FEL tuning
(Above) A man, known to FEL lore as "The Wizard", using analogue components to tune the different magnetic components of the FEL. (Below) Three befuddled graduate students look on while the maestro (Dave Enyeart) conducts his symphony. Here David is using a LabVIEW program to interface with the magnetic components in the vault, used to tune the electron beam.

known to recirculate an induce lasing in the cavity. Starting at the most upstream point of the beam line, where the electrons are exiting the accelerator, to the most downstream, users make small adjustments to the magnetic components to create a beam path which

recirculates most of the electrons. Once this is achieved and verified with the CT voltage readout, the beam length can be increased to induce lasing.

In sub microsecond steps, users increase the pulse length, which is in effect increasing the gain of the electrons in the FEL cavity. Eventually, with a long enough pulse, the gain in the cavity will be greater than the loss in the cavity, and lasing will be induced. It should be noted that beam alignment in the cavity is the most direct way to increase the gain. Put another way, a beam could be so misaligned going into the cavity that no beam width will induce lasing. Additionally, optical components in the cavity which interact with the generated THz field could be lossy enough that no electron beam will be able to lase in the cavity. This has occurred once during my PhD, and the experience is detailed in a section of the Appendix.

1.3.2 THz Generation in the FEL

Now that we have an electron beam entering the FEL cavity with enough energy at the right alignment as to induce lasing, we are producing coherent THz radiation. Compared to other THz sources, the radiation output from the FEL has a few distinguishing characteristics:

Quasi-cw Operation — Whereas other sources of THz generation [cite ZnTe and LiNbO3 papers] emit only one or a few cycles of THz radiation, any given FEL THz pulse will contain ~10,000 cycles of the THz field.

Narrow Frequency — Because the wiggling of electrons in a well defined magnetic array determines the frequency of output THz radiation, the bandwidth

of the output FEL radiation is on the order of 1 GHz, 1000 times less than the typical THz source bandwidth [68]. Given the relationship between the frequency of light and the energy of a photon [72], for HSG experimentation this implies there is a well defined energy scale for the physics we are probing.

Moderate Power, High Energy — While the peak field and power output of the FEL is ~100 times less than the top of the line THz sources, these other THz sources output few cycles THz radiation. When you multiply the power output by the timescale the THz field is present on the sample, the FEL makes up for this lower peak power with its much longer pulse width. This leads to ~mJ of THz energy in a single pulse from the FEL, unprecedented in any THz source [find citation].

Tunable Frequency — The frequency generated by the FEL is determined by the periodicity of the magnetic field wiggling the free electrons. Due to relativistic length contraction [73] electrons of different energies experience magnetic fields of different periodicities. In this way, the FEL is a broadly tunable source of THz radiation, where the output THz frequency is determined by the terminal voltage of the accelerator.

These characteristic features of the FEL are embedded in the sideband spectra we observe in lab on a regular basis. The narrow line width of the THz radiation from the FEL generate sideband photons well defined in frequency space. The quasi-cw mode also allows for large signal acquisition on moderate time scales for optical experimentation

(~10 sec, or 10 FEL pulses), allowing for a greater signal to noise ratio. This high signal to noise environment, with photons well defined in frequency space and tuned to relevant energy scales enables HSG polarimetry to precisely measure the polarization state of sideband photons.

The FEL also offers a mode of operation which allows for higher power output, called the cavity dump mode. In this mode, three mirrors form a closed cavity, coupling out little THz radiation. Once the FEL starts lasing, THz radiation builds up in the cavity. In order to actually use this build up THz radiation, there needs to be a mechanism for coupling it out.

In-between two of the mirrors sits a silicon (Si) slab, mounted at Brewsters angle. By exciting the Si with a green laser pulse, the newly created conduction electrons make the Si reflective to THz frequencies. At Brewsters angle, this Si slab acts a lot like a metallic mirror, and couples the THz out of the cavity and into the optical transport system [65, 67, 68, 70, 74, 75]. Because the THz is released from the cavity all at once, the FEL no longer produces a low-field pulse lasting on the order of the electron beam width, but instead a high-field pulse with a duration determined by the speed of light and the length of the cavity. For the FEL cavity we use, this round trip time is ~40 ns.

Because the Si slab is never perfectly at Brewsters angle, and even if it were, by dint of geometry the full THz wavefront is not *all* confronting the Si at Brewseters angle, some of the THz radiation is coupled out during the cavity building process. This low power portion of the THz pulse is called the front porch. An FEL operational heuristic says the larger the THz energy in the front porch, the less there is in the high-power

cavity dump. Therefore, it is a goal of FEL operation to set the Si at an angle where this front porch signal is minimized using a stepper motor. After this parameter is tuned, the high field THz output is optimized for experiments, such as the HSG experiments detailed in this thesis.

1.4 MAIN TEXT OUTLINE

The remaining chapters of this thesis will detail different experiments which utilize sideband polarimetry to gain insight into the quantum mechanics of non-equilibrium quasiparticles in solids. The synopsis of the subsequent chapters goes as follows:

Chapter 2 — What can the altered polarizations of sidebands tell us about the Bloch Wavefunctions which created them?

Chapter 3 — How can we move from a basis centered around optics to a basis centered on the constituent wavefunctions?

Chapter 4 — Can we model the polarization of sidebands we observe as an interferometry experiment?

Chapter 5 — How do the initial energies of the quasiparticles change the observed sideband polarization?

Chapter 6 — What role does the dispersion relation play in the sideband polarization state? Can we reconstruct the constituent components of the dispersion relation, i.e. the effective Hamiltonian of the particle?

Chapter 7 — What lies ahead for HSG experimentation?

To answer such questions, we need both a theory connecting the influence of different experimental parameters to the predicted sideband polarization state *and* an experimental method to isolate the influence of one variable. My goal is to present experimental data which mastered the latter, and delivering the most insight possible from results utilizing the former.

Chapter 2 — Reconstructing Bloch Wavefunctions

The discovery of Dynamical Birefringence (DBR) lead to the development of Dynamical Jones Calculus formalism used to characterize chaining sideband polarimetry [76]. The methods developed to investigate the mechanisms of DBR, specifically pulsed Stokes polarimetry, form the majority of experiments conveyed in this thesis, and are worth detailing.

This chapter details how conventional optical measurements can be used to reconstruct of the Bloch wavefunctions when connected to the proper theory. The experiments detailed in this chapter are the first demonstrations of HSG reconstructing the wavelike behavior of quantum condensed matter. By connecting the outgoing polarization of our sidebands to the quantum processes producing them, we generated

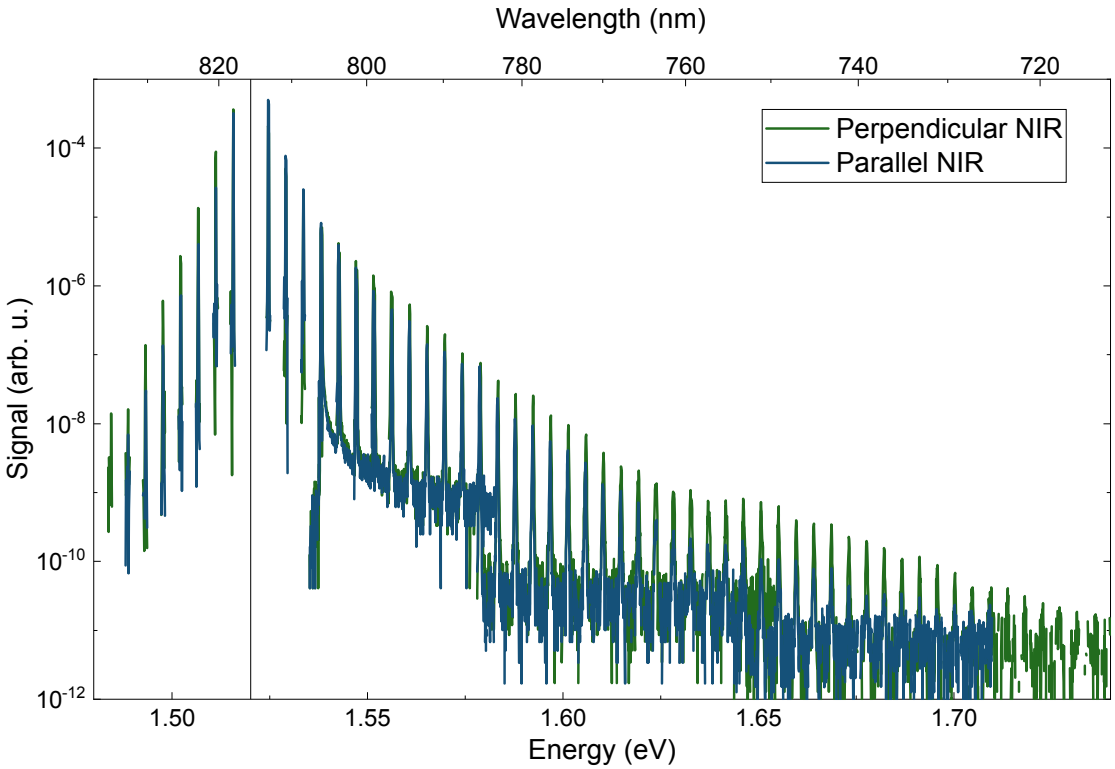

Figure 2.1 - Dynamical Birefringence In Bulk GaAs.
An example of DBR in a 500 μm sample of bulk GaAs. The two spectra are taken with different NIR polarizations: parallel to the THz polarization (red) and perpendicular (black). Each spectra are normalized to the laser line of their NIR laser field.

newfound access to the behavior of quasiparticle wavefunctions in these systems. In the process, a new paradigm of HSG as a Bloch wave interferometer was born, which serves as the motivation for the remaining chapters of this thesis.

2.1 DYNAMICAL JONES CALCULUS

The intensity of outgoing sidebands generated in GaAs/AlGaAs quantum wells are dependent on the incoming NIR laser's polarization [76]. The sidebands generated by quasiparticles excited by NIR light parallel to the THz field were stronger than those excited by NIR light perpendicularly aligned to the THz. Further investigations saw the polarization of each sideband was changing, and dependent on NIR excitation.

2.1.1 Dynamical Birefingence and Dynamical Jones Calculus

GaAs is not a birefringent material. Along the (001) face, which is the direction of the NIR propagation, are the same along all crystal axes. However, when driven by the THz field, the outgoing sidebands do demonstrate a birefringent-like behavior. Due to the necessity of the THz driving field in this phenomenon, the group labeled this behavior Dynamical Birefringence [76]. Figure 2.1 is an example of two spectra which demonstrate dynamical birefringence in bulk GaAs, with the green peaks and blue peaks having been acquired with orthogonal NIR excitation pulses. The responsibility of the THz field in DBR and the energy gained by the sidebands also required an upgrade to the traditional Jones matrix formalism, which the group called Dynamical Jones Calculus.

The modified Jones Calculus equation looks incredibly similar to the original Jones calculus used to map an incoming polarization state to an outgoing polarization state [77]

$$\begin{pmatrix} E_{x,n} \\ E_{y,n} \end{pmatrix} = \begin{pmatrix} J_{xx,n} & J_{xy,n} \\ J_{yx,n} & J_{yy,n} \end{pmatrix} \begin{pmatrix} E_{x,NIR} \\ E_{y,NIR} \end{pmatrix} \tag{2.1}$$

With the n in the outgoing electric field indicating the higher frequency of the outgoing electric field, $\Omega + n\omega$, and the n in the Jones matrix elements indicating the existence of a different Jones matrix for each sideband order. Put another way, the sideband polarization changes with sideband order, and the set of Jones matrices captures both the transformation from NIR to sideband polarization.

Because the Jones matrix elements are independent of NIR polarization, they can be reconstructed through experiment. The outgoing sideband polarization is measured through Stokes polarimetry, which is the next subject of discussion.

2.1.2 Pulsed Stokes Polarimetry

After the realization that sidebands had a different polarization than the input NIR polarization, a pulsed polarimetry experimental apparatus was used to fully characterize the polarization states of the sidebands observed in the Sherwin group's CCD sideband detection scheme. The full polarization state of an electric field can be parameterized by the four Stokes parameters. For a generic electric field $|E\rangle$, the Stokes parameters are defined as

$$\begin{aligned} S_0 &= \langle E \,|\, E \rangle \\ S_1 &= \left(\langle H \,|\, E \,|\, H \rangle - \langle V \,|\, E \,|\, V \rangle \right) \cdot S_0^{-1} \\ S_2 &= \left(\langle D \,|\, E \,|\, D \rangle - \langle A \,|\, E \,|\, A \rangle \right) \cdot S_0^{-1} \\ S_3 &= \left(\langle R \,|\, E \,|\, R \rangle - \langle L \,|\, E \,|\, L \rangle \right) \cdot S_0^{-1} \end{aligned} \tag{2.2}$$

The S_0 parameter is the electric field's overall intensity, and the other three parameters, normalized by the electric field intensity, take on values between -1 and 1. Here $|H\rangle$ is the horizontal component of the electric field, and $|V\rangle$ is the vertical component, so the S_1 parameter quantifies the relative difference between horizontal and vertically polarized light in the electric field. In the same manner, S_2 quantifies the relative difference between the diagonal component $|D\rangle$ and anti diagonal component $|A\rangle$, and S_3 quantifies the relative difference between the right handed circularly polarized (RHCP)

component $|R\rangle$ and left handed circularly polarized (LHCP) component $|L\rangle$. With these four parameters, the electric field $|E\rangle$ is fully defined.

In order to measure these values for each sideband, directly after the cryostat, a quarter wave plate (QWP) and polarizer were installed to the CCD HSG detection scheme. This combination of QWP and polarizer is called a polarimeter. The polarizer was tuned to the horizontal axis of the optical table. Because of the polarizer determines the polarization of the output light, this insures that regardless of the sideband polarization state, reflections off of further elements on the optical table are uniform. Conventional optical mirrors have slight differences in reflection coefficients in the *s* and *p* orientation, so having a uniform, defined polarization of light reflecting off of the mirrors directing sidebands into the CCD provides experimental consistency. In addition, the diffraction gratings used for frequency resolved measurements in the CCD and PMT have preferential NIR orientations, making a consistent NIR polarization on these components essential.

If the polarization of light exiting the polarimeter is constant and independent of sideband polarization, what is the experimental value which is dependent on the Stokes parameters of a sideband? The dependent variable we measure is the intensity of the sideband measured on the CCD.

Using the Muller matrices for a QWP with fast axis at an angle φ from the polarizer axis and a polarizer with a horizontal orientation, we can calculate the measured intensity of a sideband, S_{out}, in terms of an arbitrary set of Stokes parameters.

$$S_{out} = \frac{S_0}{2} + \frac{S_1}{4} - \frac{S_3}{2}\sin(2\varphi) + \frac{S_1}{4}\cos(4\varphi) + \frac{S_2}{4}\sin(4\varphi) \tag{2.3}$$

For a defined φ, the measured S_{out} is not unique to one set of Stokes parameters. However, by measuring how S_{out} changes with φ, $S_{out}(\varphi)$, we can reconstruct the unique set of Stokes parameters for a given sideband.

In order to do this, the QWP is mounted on a motorized rotation mount, in order to measure $S_{out}(\varphi)$ for many QWP orientations. Due to the periodicity of the sine and cosine terms, we need to sample a certain number of angles in order to resolve contributions by all the Stokes parameters. Standard operating procedure is to take data at 16 QWP orientations, sweeping 360 degrees of rotation in 22.5 degree steps. Figure 2.2 shows a plot of one such scan, where the y-axis is the measured $S_{out}(\varphi)$, and the x-axis being the QWP fast axis orientation, with the sixteen discrete steps visible in the data. Half of this scan is technically redundant, due to the periodicity of the trigonometric terms, however, experimental discrepancies in the first and second half of the sweep reveal misalignments in optical components in the polarimeter. If the two halves are not equivalent, something is wrong with the apparatus, must be realigned, and the data set must be retaken.

Given the four Stokes parameters are multiplied by orthogonal trigonometric expressions, Fourier analysis can transform $S_{out}(\varphi)$ into different Fourier components, which are related to contributions of different Stokes parameters. Using the Fourier transform

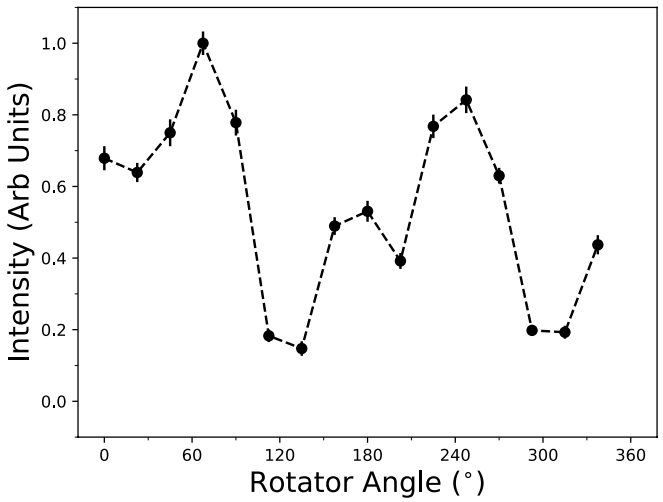

Figure 2.2 - Polaragram Used To Reconstruct Stokes Parameters
The measured intensity of the 24th order sideband as a function of the angle between the QWP fast axis and the horizontal analyzer. The data are normalized to the highest intensity datum. (Inset) A cartoon of the polarimeter, with the QWP and Analyzer depicted with respect to the SB field.

$$\mathcal{F}_m = \frac{1}{2\pi}\int_0^{2\pi} S_{out}(\varphi)e^{im\varphi}d\varphi \tag{2.4}$$

We can express the Stokes parameters as

$$\begin{aligned} S_0 &= 2\mathcal{F}_0 - 4\mathrm{Re}(\mathcal{F}_4) \\ S_1 &= 8\mathrm{Re}(\mathcal{F}_4) \\ S_2 &= -8\mathrm{Im}(\mathcal{F}_4) \\ S_3 &= 4\mathrm{Im}(\mathcal{F}_2) \end{aligned} \tag{2.5}$$

From this systematized rotating QWP measurement, we can reconstruct the Stokes parameters of a sideband. Because this method is broadband and we are simultaneously measuring the $S_{out}(\varphi)$ of all sidebands peaks recorded on the CCD, we are simultaneously measuring the Stokes parameters of all the sidebands.

The Stokes parameters are sufficient to describe the polarization of an electric field, however, with well polarized light the sideband electric field can parameterized

with just two values, the linear orientation, α, and the ellipticity, γ, which can be calculated from the Stokes parameters

$$\begin{aligned}\alpha_n &= \frac{1}{2}\tan^{-1}\left(\frac{S_2(n)}{S_1(n)}\right)\\ \gamma_n &= \frac{1}{2}\tan^{-1}\left(\frac{S_3(n)}{\sqrt{S_1^2(n)+S_2^2(n)}}\right)\end{aligned} \tag{2.6}$$

These values can be used to express the sideband polarization in the Cartesian basis

$$\begin{pmatrix}E_{x,n}\\E_{y,n}\end{pmatrix} = \begin{pmatrix}\cos\alpha_n & \sin\alpha_n\\ -\sin\alpha_n & \cos\alpha_n\end{pmatrix}\begin{pmatrix}\cos\gamma_n\\ i\sin\gamma_n\end{pmatrix} \equiv \begin{pmatrix}\cos\beta_n\\ e^{i\delta_n}\sin\beta_n\end{pmatrix}e^{i\zeta_n} \tag{2.7}$$

The same expression is true for the NIR polarization, and these two expressions combined with Eq. 2.1 give the linear expression

$$\begin{aligned}&\cos\beta_n\left(\frac{J_{yx,n}}{J_{xx,n}}\cos\beta_{NIR} + \frac{J_{yy,n}}{J_{xx,n}}e^{i\delta_{NIR}}\sin\beta_{NIR}\right)\\ &-e^{i\delta_n}\sin\beta_n\left(\cos\beta_{NIR} + \frac{J_{xy,n}}{J_{xx,n}}e^{i\delta_{NIR}}\sin\beta_{NIR}\right) = 0\end{aligned} \tag{2.8}$$

From this, we can reconstruct the Jones matrix elements up to an arbitrary phase by independently tuning three or more α_{NIR} & γ_{NIR} and measuring the outgoing α_n & γ_n and solving the resulting system of linear equations. This method sets $J_{xx,n} = 1$, for all n, so it is experimentally resolved up to a phase $\zeta_{NIR} - \zeta_n$ which cannot be resolved experimentally since the THz and NIR source are not phase locked.

2.1.3 the Circular Basis of the Jones Matrix

Due to the optical selection rules of bulk GaAs, the circular basis is more natural for the theoretical description of sideband polarization. Fortunately, the Jones matrices measured in the Cartesian basis can be converted to the circular basis using a unitary transformation. If we define the two Jones matrices in the different bases as

$$\mathcal{J}_n \equiv \begin{pmatrix} J_{xx,n} & J_{xy,n} \\ J_{yx,n} & J_{yy,n} \end{pmatrix}$$
$$\mathcal{T}_n \equiv \begin{pmatrix} T_{++,n} & T_{+-,n} \\ T_{-+,n} & T_{--,n} \end{pmatrix} \tag{2.9}$$

Where $+ \,\&\, -$ denote the RHCP and LHCP basis, respectively. The unitary transform matrix $U(\phi)$, where ϕ is the orientation between the [100] crystal axis of GaAs and the horizontal lab frame/THz field orientation, and

$$U(\phi) \equiv \begin{pmatrix} e^{-i\phi} & -e^{i\phi} \\ ie^{-i\phi} & ie^{i\phi} \end{pmatrix} \tag{2.10}$$

Can be used to transform form one basis to another, using the relation

$$\mathcal{T}_n = U^{\dagger}(\phi)\mathcal{J}_n U(\phi) \tag{2.11}$$

Because ϕ is known, this transformation is possible for experimentally measured values.

2.1.4 Expected Jones Matrix Values in Bulk GaAs

For reasons which are extensively detailed in the next Chapter and other publications [63], the expected values of ratios of these circular Jones matrix elements

$$\frac{T_{++,n}(\theta)}{T_{--,n}(\theta)} \equiv \xi_n(\theta) = 1 \tag{2.12}$$
$$\frac{T_{+-,n}(\theta)}{T_{-+,n}(\theta)} \equiv \chi_n(\theta) = \frac{\sin(2\theta) - i\gamma_3/\gamma_2 \cos(2\theta)}{\sin(2\theta) + i\gamma_3/\gamma_2 \cos(2\theta)}$$

Here θ is the orientation from the [110] axis of bulk GaAs to the THz electric field orientation, which governs the direction of the quasiparticles thought the crystal lattice. The values γ_3 & γ_2 are two of the Luttinger parameters discussed in the previous Chapter. These expected Jones matrix relations have a few expected behaviors

Constant Magnitude of $\xi_n(\theta)$ & $\chi_n(\theta)$ - In both of these expressions, the magnitude of the Jones matrix relations $\xi_n(\theta)$ & $\chi_n(\theta)$ is a constant value of 1, independent of sideband order and THz-to-crystal axis orientation.

Zero Phase of $\xi_n(\theta)$ - Even though $T_{++,n}(\theta)$ & $T_{--,n}(\theta)$ are complex numbers with non-zero phases, their ratio should have no phase, for all sideband orders and crystal axis orientations.

Phase of $\chi_n(\theta)$ depends on crystal angle - The phase of $\chi_n(\theta)$ should vary with the crystal orientation and, besides special values of θ, be non-zero.

Phase of $\chi_n(\theta)$ is constant for sideband order - While the phase of $\chi_n(\theta)$ should vary with θ, it should be constant for all sidebands observed at a given crystal orientation. This is related to the fact that the block diagonal wavefunctions are constant in $|k|$, because the sideband order is related to the quasimomenta where the quasiparticles annihilated.

Phase of $\chi_n(\theta)$ depends on the ratio γ_3/γ_2 - Along with the dependence on crystal angle, the values of $\chi_n(\theta)$ depend on the ratio γ_3/γ_2. Because the numerator and denominator of $\chi_n(\theta)$ are complex conjugates, this dependence is only expected to manifest in the phase. With the crystal orientation θ experimentally set, the ratio γ_3/γ_2 is the unknown value influencing the measured $\chi_n(\theta)$, allowing for the ratio to be reconstructed from experimentation.

In order for experimental data to convincingly reconstruct the ratio γ_3/γ_2, all five of the listed behaviors of $\xi_n(\theta)$ & $\chi_n(\theta)$ should be apparent in the experimental data. As the beginning of the next section will detail, all five of these behaviors were not observed in previous iterations of HSG experimentation, leading to overhauls in the sample fabrication process and the standard experimental process.

2.1.5 the Ratio γ_3/γ_2 and the Bloch Wavefunctions

Going back to the expression for the valence bands of the block diagonal Luttinger Hamiltonian in the previous chapter,

$$H_{v,s}(\mathbf{k}) = \frac{\hbar^2 k^2}{2m_o}\left(\gamma_1\tau_0 + \mathbf{n}_s \cdot \tau\right) \tag{2.13}$$

The eigenvalues of these two matrices are the dispersion relations, or energies as a function of quasimomenta, of these hole states. The eigenfunctions are the Bloch wavefunctions of these hole states. The first term in the parentheses is in the form of the identity matrix, and gives us information about the eigenvalues of the matrix. The second term in the parentheses has off-diagonal elements, which give us the form of the Bloch

wavefunctions. The Pauli spin matrices are known, and the only missing piece of information is the spinor component,

$$\mathbf{n}_{\pm}(\theta) = \left[\frac{\sqrt{3}}{2} \sin(2\theta), \mp \frac{\sqrt{3}\gamma_3}{2\gamma_2} \cos(2\theta), -\frac{1}{2} \right] \tag{2.14}$$

The ratio γ_3/γ_2 is the only unknown in the spinor component, so an experimental measurement of this ratio could lead to a reconstruction of the Bloch wavefunctions of the holes in bulk GaAs.

2.2 LIMITING THE INFLUENCE OF STRAIN IN SIDEBAND POLARIMETRY

There are ways to conduct HSG polarimetry experiments which do not yield the expected χ and ξ values predicted from the block diagonal Luttinger Hamiltonian. This suggested the predictions of sideband emissions required higher order physics, making it more convoluted and difficult to extract values like the Luttinger parameters from experimental data. However, many data sets with this behavior have a common trait. The sideband signal was not well polarized, parameterized by the degree of polarization

$$DOP = S_0(n) \cdot \left(S_1^2(n) + S_2^2(n) + S_3^2(n) \right)^{-1/2} \tag{2.15}$$

For polarized light, the DOP is 1. Coherent processes like HSG take polarized light (the incoming NIR pulse) and output well polarized light. Among other simplifications, the coherent nature of HSG radiation allows us to use the reduced Jones matrix formalism to map incoming NIR light to outgoing HSG photons. For light of arbitrary polarization, the more involved 4x4 Muller matrix formalism must be used. This sections details

modifications made to the HSG experimental setup which enabled the reconstruction of Bloch wavefunctions, and serves as a demonstration of how sensitive HSG polarimetry is to the microscopic physics of quasiparticles.

2.2.1 Role of Strain on Hamiltonian and Jones Calculus

By interpreting the sideband signal as the sum total of the physics contained in the region encircled by the THz and NIR beam spot on our sample, our intuition honed in on the strain of our sample. Strain on the GaAs lattice will lift the degeneracy of the HH and LH pairs at the Γ point and distort the band structure nearby. This is the band structure which determines the dynamics of the quasiparticle pairs as they are driven by the THz field, and by extension influences the outgoing sideband polarization. Samples with different strain, or even spots on the sample with different strain, have different outgoing sideband polarizations from the same NIR excitation.

Further complications ensue for a sample with inconsistent strain, where, on the size scale of the NIR beam spot (~100s of μm) the strain was varying significantly. The HSG signal will be combination of photons emitted from microscopic regions on the sample with measurably different physics. This superimposed signal, with multiple sources of different polarizations, will inherently lead to a combined sideband electric field with DOP less than one.

Our hypothesis was not rejected with a local absorbance measurement of our GaAs sample. Absorbance provides a straightforward but limited measurement of the strain of the sample illuminated by the white light. A clear continuum state is visible, with an increased density of states in the HH and LH excitonic states. The difference in energy

of the two peaks, or peak splitting, can be related to the amount of strain on the lattice. However, absorbance does not provide any information on the direction of strain. By taking absorbance spectra at spots less than a NIR beam width apart, we saw the peak splitting varied on the order of meV, indicative of rapidly changing local physics on our GaAs sample. Figure 2.3 demonstrates how spots on the sample with different strain, as measured through absorbance in the upper left figure, lead to qualitatively different sideband intensities (upper right) and polarizations (lower plot of fans).

Because we are sampling different pockets of microscopic physics from our mesoscopic NIR and THz optics experiment, we cannot extract key values parameterizing the microscopic physics of our quasiparticles, like the Luttinger parameters. If we wanted a more straight forward insight to the effective Hamiltonian, we needed to fabricate a sample with a more consistent local strain environment.

2.2.2 Circular Sample Fabrication

From our depolarized HSG signal, it would appear our current methods of sample fabrication was not cutting it. Following intuition and popular semiconductor fabrication methods, we decided etching a circular epilayer of GaAs could yield samples with a more uniform strain environment. This involved incorporating a mesa etch to the front end of our sample fabrication process (see appendix for more details).

After a successful fabrication process was established and a sample was ready, absorbance measurements revealed a sample regions of consistent strain. One of these regions was characterized with finely stepped position-based absorbance spectra, and the

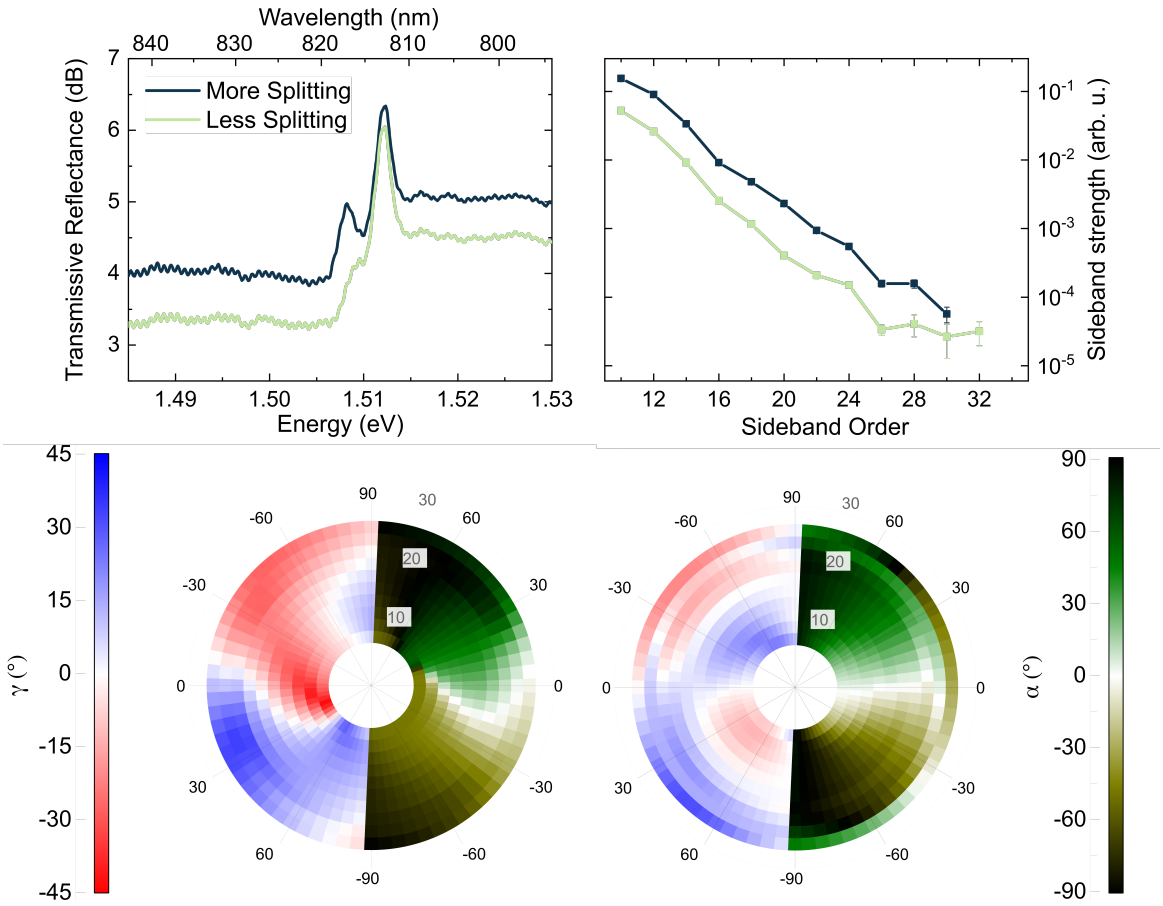

Figure 2.3 - Role of Strain on Polarimetry
(Above, Left) The absorbance spectra at two positions on the GaAs sample. The strain can be qualitatively observed by the splitting of the HH and LH absorbance peaks. (Above, Right) Measured sideband intensities for polarimetry runs taken at these two different spots. (Below) The fans diagrams from polarimetry data taken at spots A and R. The fundamentally different behaviors of α and γ at both spots is visually apparent.

most stable local region was chosen for future HSG experimentation, the results of which are detailed in the next section.

2.2.3 Equipment and Experiment Specifics

Given the hypothesized THz-to-crystal axis dependence of χ and ξ, the ability to mount the sample at some arbitrary angle was a desired but missing feature of our cryostat. A cryostat was designed and machined to allow for the incorporation of a rotation sample stage.

Using pulsed Stokes polarimetry, we measured the Stokes parameters of sidebands. To reconstruct the Jones matrix elements, we conducted this method on sidebands produced with four different NIR excitations, α = 0, 90, +45, and -45 degrees, with γ = 0 degrees for all four excitations. Figure 2.4 displays data from polarimetry scans using these four NIR polarizations. The upper plot holds the measured α of the sidebands, and the lower plot holds the measured γ of the sidebands, defined with the polarization ellipse in the lower plot's inset. Data taken with different NIR orientations are displayed with different colored curves (blue, α = 0; red, α = 90; yellow, α = + 45; green, α = - 45, displayed in the cartoon of the upper plot).

Only three of these are required to create a systems of linear equations from Eq. 2.8 which reconstruct the Jones matrix elements up to an arbitrary phase. By including positive and negative 45 degree excitations, we create an internal consistency check for an experimental run. The symmetries of the sample and the phenomena are time reversal invariant, so excitations by time reversely symmetric NIR should yield equivalent polarizations of the opposite sign. If the data do not demonstrate this behavior, we have an indication something is flawed with the experimental run.

Any particular data set would involve mounting the sample, initially coarsely by hand and then finely with a $\pm$ 5 degree manipulator on the rotation stage. Once the sample was pumped to vacuum, the closed cycle cryogenic pump would begin cooling the sample down to 60 K, the base temperature of the cryostat setup. During this cooling process, the FEL laser was tuned at its 15 cm^{-1} operating mode, with the cavity dump

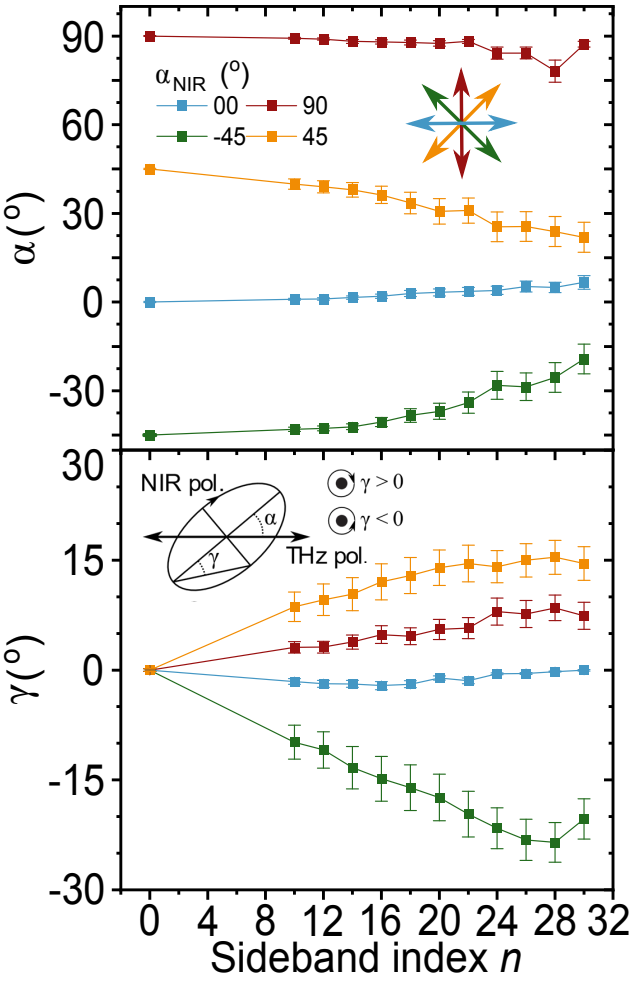

Figure 2.4 - Measured α and γ Used To Reconstruct Jones Matrix Elements. The measured α and γ of sidebands 10 to 30 for four different NIR polarizations, depicted in the cartoon above. (α_{NIR} = 90 deg (red curves) α_{NIR} = 45 deg (yellow), α_{NIR} = 0 deg (blue), α_{NIR} = -45 deg (green)). (Above) The measured α_n at each of these NIR orientations. (Below) The measured γ_n at each of these orientations.

folding mirror (mostly) in place. Attention was given to the FEL outputting THz with comparable power (~2 mJ) over all of the days experimental data was taken.

With the sample at 60 K and the FEL tuned for THz output, the NIR optics were tuned to pass one of the four predetermined polarizations using the HWP and QWP. Because those two optical components will pass different intensities of NIR light, depending on the incoming NIR polarization from the AOM and the set outgoing

polarization, we need to tune the amount of radiation exiting the initial NIR optical setup. Earlier in the beam path is a a HWP and vertical polarizer, and be tuning the relative angle of the HWP fast axis to the vertical axis, we can fine tune the intensity of the NIR field encountering the HWP and QWP. As a result, we can ensure the power on the GaAs sample is 100 mW for all four NIR polarizations conducted during experimentation.

We enhanced our signal-to-noise ratio by peaking up the sideband signal observed in our CCD detection scheme while reducing noise introduced by the laser line. The former involved fine tuning NIR optics after the cryostat to maximize the observed intensity of a lower order sideband for one-pulse acquisitions of our CCD. The latter was achieved by tuning a short pass filter to attenuate the 8th order sideband while fully passing the 10th order sideband, and setting the edge of the spectrometer to clip the 6th order sideband on the CCD aperture. Even though the laser line is ~10^6 more intense than the sidebands, these actions make the sharply peaked sidebands the most prominent feature in the frequency domain when compared to the tail of the laser field.

Because the experiments detailed in this chapter we run at the same NIR frequency and conducted over consecutive days, only a small amount of fine tuning was required to maintain a constant acquisition of sideband radiation. However, these steps were important for consistency as a few components needed to be snapped in and out of magnetic mounts, and the sample had to be macroscopically slid in and out of the NIR beam path for the setting of different NIR polarizations. Repeating this process every day, at every NIR polarization ensures consistency in the acquisition of polarimetry data.

2.3 EXPERIMENTAL ANALYSIS

Finally, all of the cards are in place. We have a sample which is confirmed to have a uniform strain environment. We have a cryostat which allows us to rotate the sample over a 360 degree phase space. We have an FEL which is lasing consistently, and an established NIR optical apparatus to capture the sidebands generated under these controlled experimental conditions. We have a theory which can take us from experimental data to an interpolated story of the microscopic physics of our sample. All of this took over two years to develop. Over the span of two weeks, Joe and I clicked through polarimetry scans at different THz-to-crystal axis orientations. Each data set demonstrated close to the expected behavior of χ and ξ, outlined in bold above. Together they told a fascinating story of our quasiparticles, detailed below.

2.3.1 Constant Jones Matrix Ratios

Figure 2.5 A and B and Figure 2.6 show experimentally observed values of χ and ξ which are constant in sideband order. Because the Bloch wavefunctions do not vary with $|\mathbf{k}|$, we do not expect these values we use to reconstruct the wavefunctions, χ and ξ, to vary with a value analogous with quasimomenta, or sideband order. Observing behaviors of χ and ξ qualitatively similar to the Bloch wavefunctions brings us a step closer to their reconstruction.

2.3.2 Angle Dependent Phase of Jones Matrix Elements

The other important behavior of both the Bloch wavefunctions and thus our reconstructed Jones matrix elements is the expected angular dependence. Both should vary with THz orientation θ, and should take on the C_4 rotational symmetry of the GaAs crystal in the

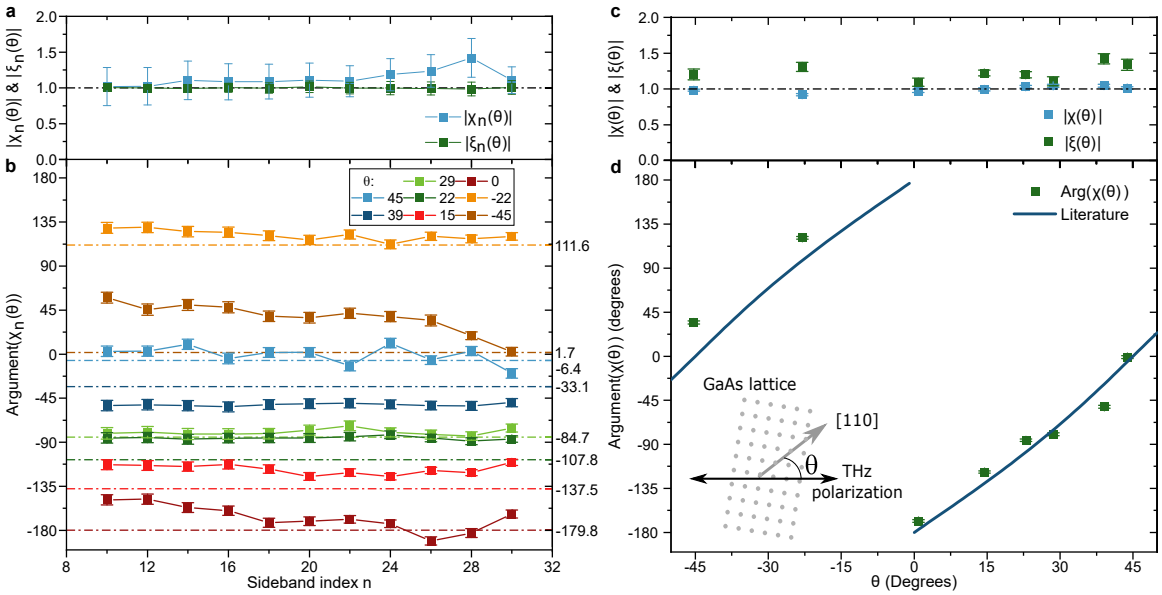

Figure 2.5 - Values of χ and ξ Measured in Experiment.
A) The measured values of $\left|\chi_n(\theta = 39\,\mathrm{deg})\right|$ and $\left|\xi_n(\theta = 39\,\mathrm{deg})\right|$ as a function of sideband order. The expected value of 1 for both $\left|\chi_n(\theta)\right|$ and $\left|\xi_n(\theta)\right|$ is plotted with the black dash-dot line. B) The measured values of Arg $\left(\chi_n(\theta)\right)$ at different crystal angles. The theoretically expected value from Eq. 2.12 and the literature values of the Luttinger parameters γ_2 & γ_3 are plotted for data sets at each angle, the color of the dash-dot line corresponding to the THz-to-[110] crystal axis of the data set, denoted in the legend. (THz-to-[110] axis orientation defined in the inset of D). C) The value of $\left|\chi(\theta = 39\,\mathrm{deg})\right|$ and $\left|\xi(\theta = 39\,\mathrm{deg})\right|$ averaged over sideband index, $\chi(\theta) = \left\langle \chi_n(\theta) \right\rangle_n$ and $\xi(\theta) = \left\langle \xi_n(\theta) \right\rangle_n$, as a function of crystal axis orientation. The expected value of 1 for all crystal angles is denoted with the black dash-dot line. D) The experimental values of Arg $\left(\chi(\theta)\right)$ dependent on crystal axis orientation. The blue line denotes the expected value from Eq. 2.12 and the literature values of the Luttinger parameters γ_2 & γ_3.

(100) plane. As the bolded statements above mentioned, the only value of χ and ξ varying with θ should be the argument of χ. The rest should be independent of THz-to-crystal angle orientation.

Figures 2.5 (a) and 2.6 (b&c) show $\left|\chi_n(\theta)\right|$ and $\left|\xi_n(\theta)\right|$ are independent of θ and instead are 1 for all crystal angles observed in experiment. Figure 2.7(a) shows

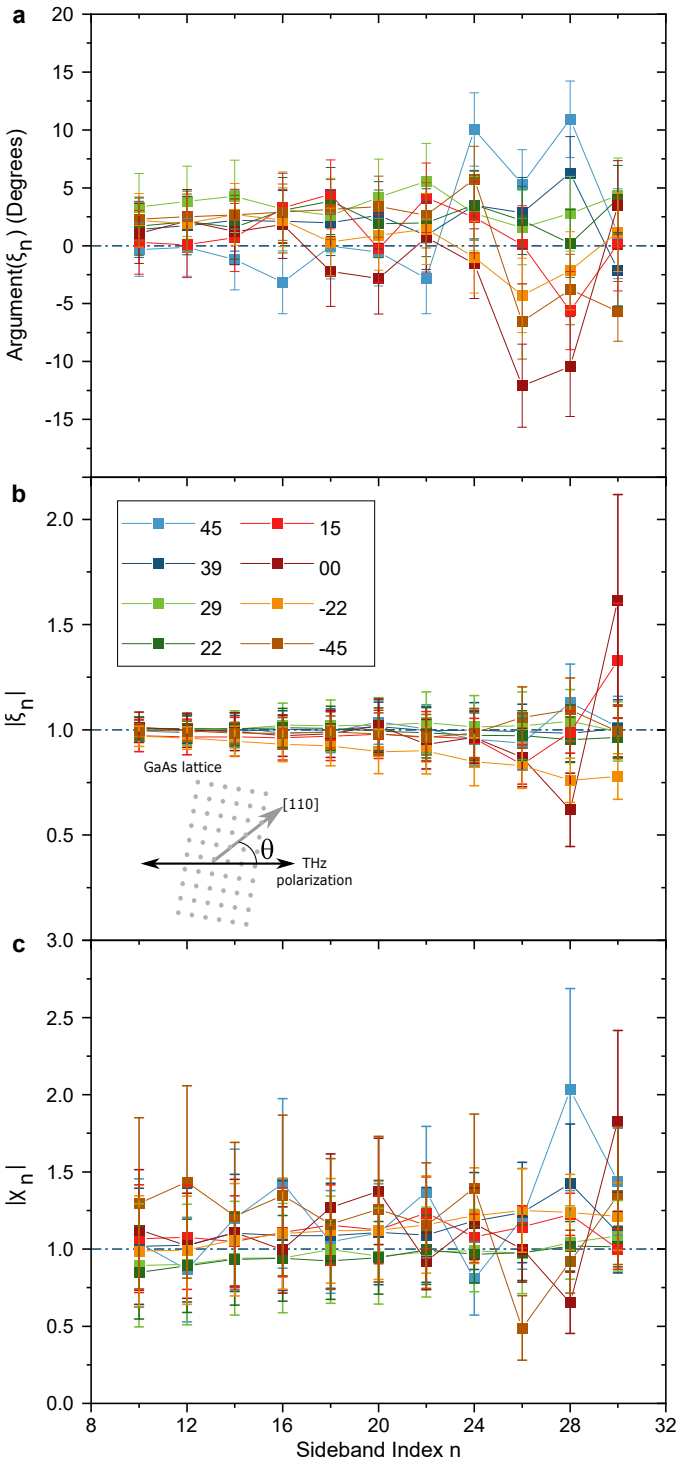

Figure 2.6 - Additional Values of χ and ξ Measured in Experiment.
A) The measured Arg $\left(\xi_n(\theta)\right)$ B) $\left|\xi_n(\theta)\right|$ C) and $\left|\chi_n(\theta)\right|$ for all experimental angles sampled. The inset of (B) defines the crystal angles with respect to the THz radiation, which is used to label the datasets in the legend. The dashed dot line marks the expected value of 0 and 1 for A and B & C, respectively.

Arg $\left(\xi_n(\theta)\right)$ is also independent of θ and is 0 for all crystal angles observed. All of these behaviors mirror what is expected in Eq. 2.12. Figure 2.6(b) shows the changing value of Arg $\left(\chi_n(\theta)\right)$ at varying θ. The dash-dot line indicates the expected value for Arg $\left(\chi_n(\theta)\right)$, using Eq. 2.12 and the literature values of γ_2 & γ_3 [45], with the experimental values lie close to the expected values of theory.

2.3.3 Field Independent Jones Matrix Elements

Given the problems previous samples had with strain affecting the quasiparticle physics of our experiment, we were concerned strain would somehow confound our χ and ξ values. Because strain distorts the dispersion relation around the Γ point, where the sidebands are created, most quasiparticle trajectories producing sidebands would experience this strain-induced distortion. The speed at which our quasiparticles interact with the altered dispersion relation should lead to noticeable effects if the distortion plays any notable role in their dynamics.

By observing the values of χ and ξ at different terahertz field strengths, we wanted to see if there was any noticeable change to the quasiparticle dynamics. Theory does not predict there to be any dependence, and an experimentally observed dependence would reveal some larger force distorting the dynamics of our quaisiparticles. Measurements of χ and ξ taken with 100%, 75%, and 50% THz field strengths (70 kV/cm, 52.5 kV/cm, and 35 kV/cm) did not depend on field strength. Figure 2.7 demonstrates measured Arg(χ) with no dependence on THz field strength. Among other conclusions, we take this to indicate strain has negligible effects on the measured pollination values we used to reconstruct the Bloch wavefunctions.

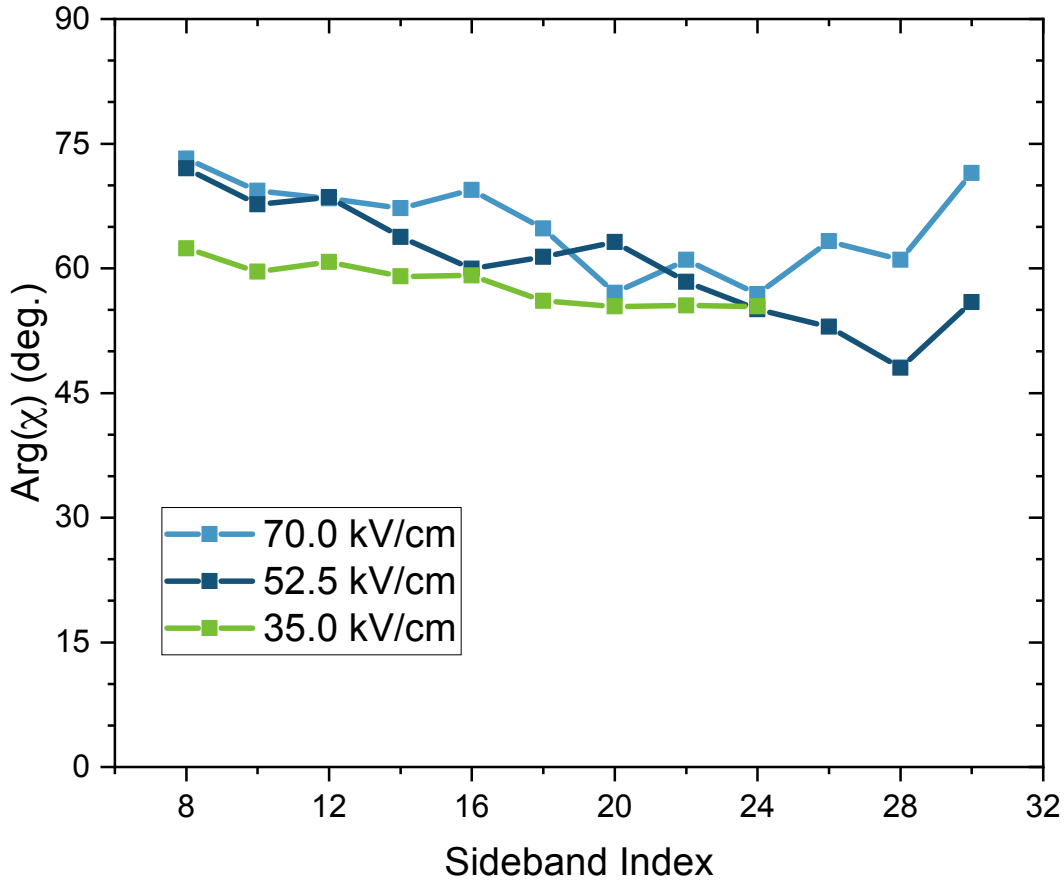

Figure 2.7 - Jones Matrix Ratios Independent of Field.
The measured Arg $\left(\chi_n(\theta)\right)$ using three different field strengths on the sample, tuned with two crossed wire-grid polarizers.

2.3.4 Reconstructed Bloch Wavefunctions

With the experimental values of χ and ξ demonstrating all of the expected behaviors, we felt confident in using this experimental data to reconstruct the ratio of γ_3/γ_2, which appears in the expression for Arg $\left(\chi_n(\theta)\right)$ and $n_{y,\pm}(\theta)$. As mentioned before, knowing the form of $\mathbf{n}_{\pm}(\theta)$ is all that is necessary to reconstruct the Bloch wave functions of the hole states in GaAs. Using our experimental data, we can reconstruct the value of $\gamma_3/\gamma_2(\theta)$

which would manifest the observed $\mathrm{Arg}\left(\chi(\theta)\right)$ for each data set at a unique crystal orientation θ:

$$\frac{\gamma_3}{\gamma_2}(\theta) = \left|\tan 2\theta\right| \sqrt{\frac{1-\cos[\mathrm{Arg}\left(\chi(\theta)\right)]}{1+\cos[\mathrm{Arg}\left(\chi(\theta)\right)]}} \tag{2.16}$$

Using these reconstructed values of $\gamma_3/\gamma_2(\theta)$, we can report an mean value and standard deviation for the reconstructed values over all the data taken in experiment, $\gamma_3/\gamma_2 = 1.47 \pm 0.48$.

From experimentally reconstructed ratio, we also have an experimentally reconstructed $\mathbf{n}_{\pm}(\theta)$, and wavefunctions. To represent our reconstructed wavefunctions, we utilize the Bloch sphere, as all of our reconstructed states are in a superposition of two angular momentum eigenstates. Each of these eigenstates will form a pole on the Bloch sphere, and the polar angle of our wavefunctions on the Bloch sphere represent the hole state being in a relative superposition of both eigenfunctions. This polar position Θ is quantified by

$$\cos(\Theta) = -\frac{1}{\sqrt{3(\sin^2(2\theta) + (\gamma_3/\gamma_2)^2\cos^2(2\theta)) + 1}} \tag{2.17}$$

The azimuthal angle of our wavefunctions on the Bloch sphere also has physical significance, equivalent to changing the THz to crystal axis orientation. Figure 2.8 is our representation of the reconstructed Bloch wavefunctions on the Bloch sphere.

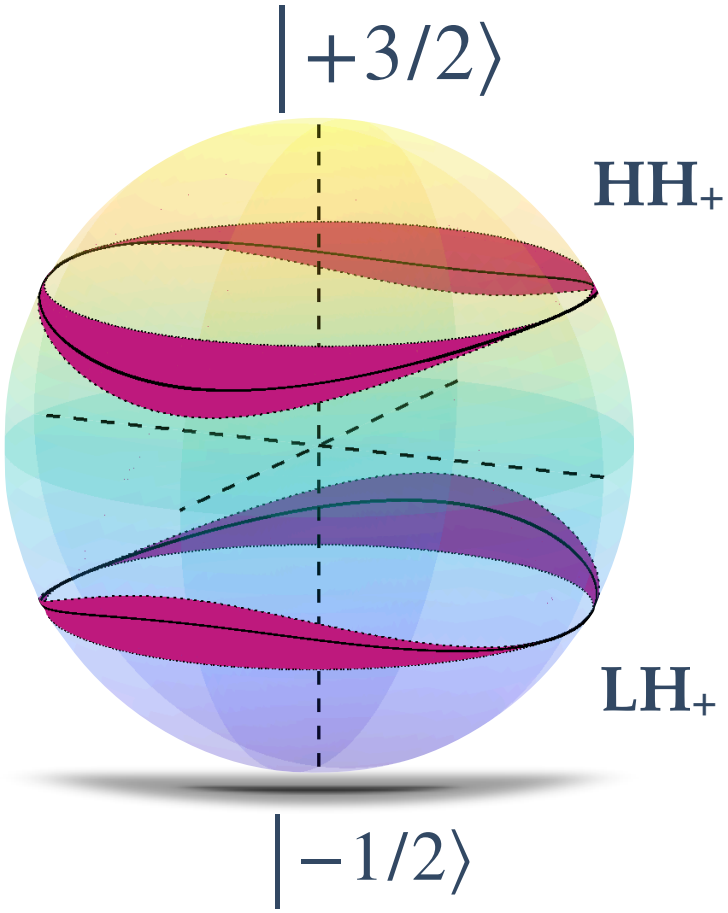

Figure 2.8 - Reconstructed Bloch Wavefucntions of Hole States in Bulk GaAs.
The Bloch wavefunctions of HH and LH bands associated with H_+ are plotted as black lines. The red shaded area corresponds to the uncertainty in the wavefunction associated with one standard deviation in the measurement of γ_2/γ_3. For a given θ, each wavefunction is represented by a point on the Bloch sphere. The poles correspond to the spin −3/2 and spin +1/2 states. The wavefunctions for H_- are paths reflected across the x–z plane on a Bloch sphere with poles representing the spin +3/2 and spin −1/2 states.

2.4 JUST THE BEGINNING

The experiments detailed above were the first to reconstruct the wavefunction of a quasiparticle in a quantum condensed matter system. By connecting the electromagnetic fields we measure in lab to the quantum mechanics of the quasiparticles creating them, HSG polarimetry gives us access to the quantum phases of our wavefunctions.

With all this in mind, the reconstruction of the Bloch wavefunctions is the beginning of the new line of research we have been developing in the Sherwin group. As the next chapter will demonstrate, the Bloch wavefunctions act as a key to transforming data into a more intuitive, wavefunction-oriented basis. Further on in the thesis, having unlocked this more intuitive basis, I start to explore how much we can actually understand about the wavefunctions of our quasiparticles. In condensed matter, the wavefunction and its Hamiltonian reflect the interaction between the quasiparticle and the crystal lattice. By measuring the phases of our wavefunctions, we develop a sensitive probe of the environment experienced by our electrons. These probes, through HSG polarimetry provide opportunities to measure material parameters previously unmeasured in experiment.

Chapter 3 — Hole Basis Analysis

With the knowledge of the Bloch wavefunctions, we can transform from the circular basis used for the optical observation used in experiment to a construction of a hole basis. In this hole basis, we can model the dynamics of the electron-hole pair as it is driven through the Luttinger Hamiltonian by the propagator ς_n^{ν}, where $\nu = \mathrm{hh}, \mathrm{lh}$. Transforming to this basis and developing an experimental method to measure in this basis allows us to connect optical measurements of sideband photons to one of hole-species contributions to the sideband polarization field. *Note:* in the SI of [63], and Qile's subsequent publications, Qile uses the character $\mathbb{Q}$ in leu of ς. Around the time I was developing my own contributions to the work, the fringe movement "Q-Anon" was becoming an increasingly dangerous presence in American civil life, including the violent storming of the U.S. Capitol in an attempt to overthrow a democratic election. Frankly, I was a bit

weary of having the character “Q” littered all over my works, so I transitioned to a more anodyne character, ς, which is the “sigma” character at the end of Greek words.

3.1 A QUANTUM THEORY OF SIDEBAND GENERATION

By the end of this first section you will see a connection between contribution to the sideband polarization field by a hole species, ς_n^{ν}, where ν = hh or lh, and the circular Jones Matrix elements, $T_{ij,n}$, detailed in the previous chapter. Laying in-between the two is the mechanism which converts the hole basis and the circular basis, which are the Bloch wavefunctions we reconstructed in the previous section. Bridging these two bases by a quantity we convincingly reconstructed in the previous chapter provides insight to the hole species basis. With the hole species basis, we can begin to examine intricacies in the differences between contributions from the e-hh and e-lh pairs to both the sideband intensity and polarization, a powerful tool which will be utilized for the rest of this thesis.

3.1.1 Quantum Path Formalism of Sideband Creation

Using a formalism developed in the Supplementary Information of previous HSG works [63], we can develop a quantitative theory for sideband generation. Breaking down the three step model into three theoretical steps, we can develop an expression for the output polarization field $\mathbb{P}$, and the Fourier transform for a particular sideband index n, $\mathbb{P}_n$.

Starting with the optical excitation, we can use the dipole transition matrix $\mathbb{D}$ of the GaAs crystal to convert incoming NIR light into electronic states. There are a few allowed transitions from hole band-edge defined states

$\left(\left|+3/2\right\rangle, \left|+1/2\right\rangle, \left|-1/2\right\rangle, \left|-3/2\right\rangle\right)$ and electron states in the conduction band $\left(\left|S\uparrow\right\rangle, \left|S\downarrow\right\rangle\right)$. The allowed transitions are the non-zero elements of $\mathbb{D}$, which takes the form

$$\mathbb{D} = -d\left(\sigma_+,0,\frac{\sigma_-}{\sqrt{3}},0,0,\frac{\sigma_+}{\sqrt{3}},0,\sigma_-\right)^T \tag{3.1}$$

Where the non-zero elements are the transitions between $\left|S\uparrow\right\rangle\left|-3/2\right\rangle$, $\left|S\uparrow\right\rangle\left|+1/2\right\rangle$, $\left|S\downarrow\right\rangle\left|-1/2\right\rangle$, and $\left|S\downarrow\right\rangle\left|+3/2\right\rangle$, respectively. Here $d = \langle S|ex|X\rangle$, where S is the scalar representation of the T_d point group, and X is the vector representation of the T_d point group along the [100] crystal axis of GaAs. The dipole elements are projected onto the basis vector for circular polarization, $\sigma_\pm = \pm\left(\hat{X} \pm i\hat{Y}\right)/\sqrt{2}$, where Y is the vector representation of the T_d point group along the [010] crystal axis of GaAs.

Because HSG is done in the linear response regime of the NIR excitation, this linear optical dipole response is sufficient to parameterize the creation of electronic states in the bulk GaAs. This also allows us to use the Luttinger Hamiltonian to parameterize the dynamics of the e-h pairs when they are accelerated by the THz field without the need for Coulomb interaction terms. Additionally, we excite states at the $k_z = 0$ point, so we can express the Luttinger Hamiltonian in the block diagonal form. If we use $s = \pm$ to denote the two 2x2 block diagonal portions, we can write the Luttinger Hamiltonian like Eq 1.1

We can express the population of the different electronic states at a given qauismomenta $\mathbf{k}(t)$ through a density matrix

$$\hat{\rho}_{s,\mathbf{k}(t)} = \left\langle \left(b_{s3/2,\mathbf{k}(t)}, b_{-s1/2,\mathbf{k}(t)} \right)^T \otimes a_{-s,\mathbf{k}(t)} \right\rangle \tag{3.2}$$

Where $b_{s3/2,\mathbf{k}(t)}$ is the creation operator for a hole state in the $|s \cdot 3/2\rangle$ angular momentum eigenstate at quasimomenta $\mathbf{k}(t)$, and $a_{s,\mathbf{k}(t)}$ is the creation operator for the electron state in the $|Ss\rangle$ band edge state at quasimomenta $\mathbf{k}(t)$. In this block diagonal form, the dipole matrix can be reduced to

$$\mathbb{D}_s = -d \left(-\sigma_{-s}, \sigma_s/\sqrt{3} \right)^T \tag{3.3}$$

and incorporated as the dipolar source term, along with the expression for the NIR electric field, $\mathbf{E}_{NIR} = E_+\sigma_+ + E_-\sigma_-$ in the time evolution of the density matrix

$$i\hbar \frac{d}{dt} \hat{\rho}_{s\mathbf{k}(t)} = \hat{H}_{v,s} \left(\mathbf{k}(t) \right) \hat{\rho}_{s,\mathbf{k}(t)} - \mathbb{D}_s \mathbf{E}_{NIR}(t) \tag{3.4}$$

This equation can be diagonalized and solved for analytically with a SU(2) unitary transformation R_s, defined as $R_s^\dagger \mathbf{n}_s \left| \mathbf{n}_s \right|^{-1} \tau^\bullet R_s = \tau_z$. This will transform the density matrix and Hamiltonian from the circular basis of the electric field to the "hole basis", were the eigenfunctions are the Bloch wavefunctions of the two hole states. This newly diagonalized expression takes the from

$$i\hbar\frac{d}{dt}\left(R_s^{\dagger}\hat{\rho}_{s,\mathbf{k}(t)}\right) = \begin{pmatrix} E_c\left(\mathbf{k}(t)\right) - E_{hh}\left(\mathbf{k}(t)\right) & 0 \\ 0 & E_c\left(\mathbf{k}(t)\right) - E_{lh}\left(\mathbf{k}(t)\right) \end{pmatrix} R_s^{\dagger}\hat{\rho}_{s,\mathbf{k}(t)} - R_s^{\dagger}\mathbb{D}_s\mathbf{E}_{NIR}(t) \tag{3.5}$$

Where $E_{hh(lh)} = -\hbar^2 k^2 (2m_0)^{-1}\left[\gamma_1 - (+)2\gamma_2 |\mathbf{n}_s|\right]$ are the eigenvalues of the block diagonal Luttinger Hamiltonian associated with the given hole species. The solution to this differential equation is

$$R_s^{\dagger}\hat{\rho}_{s,\mathbf{k}(t)} = \frac{i}{\hbar}\int_{-\infty}^{t} \begin{pmatrix} \exp[iA_{hh}(t,t')] & 0 \\ 0 & \exp[iA_{lh}(t,t')] \end{pmatrix} R_s^{\dagger}\mathbb{D}_s\mathbf{E}_{NIR}(t) \tag{3.6}$$

Where we define the dynamical phase accrued by the e-h pair between time *t* and *t'* as

$$A_{\nu}(t,t') = \int_{t}^{t'} dt''\left[E_c\left(\mathbf{k}(t)\right) - E_{\nu}\left(\mathbf{k}(t)\right) + i\Gamma_d\right]/\hbar \tag{3.7}$$

By expressing the quasimomenta of the electron and hole in terms of the semiclassical dynamics under the influence of a THz electric field $\mathbf{E}_{THz}(t)$

$$\mathbf{k}(t) = \frac{e}{\hbar}\int_{t_0}^{t} dt'\mathbf{E}_{THz}(t') \tag{3.8}$$

and incorporating this time dependent quasimomentum into the dispersion relation in the dynamical phase expression, we have an expression for the time dependent dynamical phase of the e-h pair under the influence of the THz electric field, which is then used to calculate the evolution of the density matrix of the e-h states in our GaAs sample.

For the out coupling of light in the form of sideband generation, we use the same dipole matrix $\mathbb{D}$ we used in the first step, however, this time we use it to convert electronic states in bulk GaAs into outgoing light. This is the reverse of how we used this object in step one. If we represent the outgoing polarization field as $\mathbf{P}(t)$, then using the number of electronic states present at a given time and quasimomenta, in the form of $\hat{\rho}_{s,\mathbf{k}(t)}$, we have the expression

$$\mathbf{P}(t) = \frac{1}{V}\sum_{\mathbf{k}(t),s} \mathbb{D}_s^{\dagger}\hat{\rho}_{s,\mathbf{k}(t)} \tag{3.9}$$

Where V is the volume of the sample subject to both NIR creation of excited states and THz acceleration. Because HSG is conducted in the frequency domain, the Fourier transform of $\mathbf{P}(t)$ will provide insight into the polarization field at a given sideband order, $\mathbf{P}_n$

$$\begin{aligned}\mathbf{P}_n &= \sum_{s=\pm}\frac{\omega}{2\pi V}\int_0^{2\pi/\omega}\mathbf{P}(t)e^{i(\Omega+n\omega)t}dt \\ &= \sum_{s=\pm}\frac{i\omega}{2\pi V\hbar}\int_0^{2\pi/\omega}e^{i(\Omega+n\omega)t}dt\cdot \\ &\int_{-\infty}^{t}\mathbb{D}_s^{\dagger}R_s\begin{pmatrix}\exp[iA_{hh}(t,t')]0\\ 0\qquad\qquad\exp[iA_{lh}(t,t')]\end{pmatrix}R_s^{\dagger}\mathbb{D}_s\mathbf{F}_{NIR}(t)e^{-i\Omega t'}\end{aligned} \tag{3.10}$$

Here the NIR electric field was simplified to $\mathbf{E}_{NIR}(t) \approx \mathbf{F}_{NIR}e^{-i\Omega t}$ by the rotating wave approximation, where only the $-\Omega t$ component of the electric field contributes to

quasiparticle excitation. This expression for the polarization field at a given frequency can be simplified to

$$\mathbf{P}_n = \frac{1}{d^2}\sum_{s=\pm}\mathbb{D}_s^{\dagger}R_s\begin{pmatrix}\varsigma_n^{hh} & 0\\ 0 & \varsigma_n^{lh}\end{pmatrix}R_s^{\dagger}\mathbb{D}_s\mathbf{F}_{NIR} \tag{3.11}$$

Where ς_n^{ν} is a propagator, determining the hole-species contribution to the polarization field with a frequency $\Omega + n\omega$, and takes the form

$$\varsigma_n^{\nu} = \sum_{s=\pm}\frac{i\omega d^2}{2\pi V\hbar}\int_0^{2\pi/\omega} e^{i(\Omega+n\omega)t}\int_{-\infty}^{t} dt' e^{iA_{\nu}(t,t')}e^{-i\Omega t'} \tag{3.12}$$

These ς_n^{ν} can be connected to experimentally measurable value, the Jones Matrix elements, T_{ij}, if we express the polarization field in the form of Jones Matrix analysis.

$$\mathbf{P}_n = -\begin{pmatrix}\sigma_+ & \sigma_-\end{pmatrix}\begin{pmatrix}T_{++,n} & T_{+-,n}\\ T_{-+,n} & T_{--,n}\end{pmatrix}\begin{pmatrix}\sigma_+\\ \sigma_-\end{pmatrix}\mathbf{F}_{NIR} \tag{3.13}$$

Here the sideband field and the polarization field are in the circular basis , $\mathbf{P}_n = (E_{n,+}, E_{n,-})^T$ and $\mathbf{F}_{NIR} = (E_{NIR,+}, E_{NIR,-})^T$. Using the differences between the dipole moment and the unitary circular basis of the electric field, and the diagonalization condition of the unitary rotation operator, we can relate ς_n^i to the measured Jones Matrix elements,

$$\begin{aligned} T_{++,n} = T_{--,n} &= \frac{2}{3}\left(\varsigma_n^{hh} + \varsigma_n^{lh}\right) + \frac{n_z}{3}\left(\varsigma_n^{hh} - \varsigma_n^{lh}\right)\\ T_{+-,n} &= \frac{n_x + in_y}{\sqrt{3}}\left(\varsigma_n^{hh} - \varsigma_n^{lh}\right)\end{aligned} \tag{3.14}$$

$$T_{+-,n} = \frac{n_x - i n_y}{\sqrt{3}} \left(\varsigma_n^{hh} - \varsigma_n^{lh} \right)$$

As the previous chapter and other publications have established [63, 76], we can experimentally reconstruct the Jones Matrix elements. Now, with the reconstructed Bloch wave functions, we can also reconstruct ς_n^{ν}.

3.1.2 Bloch Wavefunction Reconstruction Separating HH and LH Contribution

Simple algebra is all that stands in the way of transforming the measured Jones Matrix elements into the ς_n^{ν} values. It starts with knowing the normalized form of the spinor element $\hat{\mathbf{n}}_S = \mathbf{n}_s \left(|\mathbf{n}_s| \right)^{-1}$, where $\mathbf{n}_s$ is defined in the spinor equation. If the normalized values of $n_x, n_y, \& n_z$ are known, we can transform the known Jones Matrix expressions into ς_n^{ν} with the expressions

$$\begin{aligned} \varsigma_n^{hh} &= \frac{3}{4} \left(T_{++,n} + \frac{2 - n_z}{\sqrt{3}(n_x + i n_y)} T_{+-,n} \right) \\ \varsigma_n^{lh} &= \frac{3}{4} \left(T_{++,n} - \frac{2 + n_z}{\sqrt{3}(n_x + i n_y)} T_{+-,n} \right) \end{aligned} \tag{3.15}$$

From this expression, we can conduct analysis on the contributions of different hole species to a particular sideband signal.

3.2 SEMICLASSICAL PICTURE OF BLOCH WAVE PROPAGATION

The theory above presents a clear, quantum picture for sideband generation, and derives a propagator for our Bloch waves, ς_n^ν, and develops an experimental method for measuring these values. However, there is no straightforward (non-time intensive) way to calculate the expected values of these ς_n^ν in their current form. By reducing the possible paths which produce a sideband from all possible paths to just those contained in a single cycle of the THz field, we greatly simplify our calculation, moving from a quantum path interpretation of the sideband generation to a semiclassical picture of the quasiparticle acceleration.

3.2.1 Semiclassical Approximation

In the single cycle limit, there is only one trajectory which will emit a sideband from a given hole species at a given sideband order. First, the limits of the integral for dt' in Eq. 3.12 collapse from $-\infty$ to $t_{o,n,\nu}$, the creation time of the e-h pair which produces the *n*th order sideband, and t to $t_{f,n,\nu}$, the annihilation time for the pair. This simplifies the expression of ς_n^ν to

$$\varsigma_n^\nu = \frac{i\omega d^2}{2\pi\hbar V}\int_0^{2\pi/\omega} dt e^{i(n\omega+\Omega)t}\cdot\int_{t_{o,n,\nu}}^{t_{f,n,\nu}} dt' e^{iA_\nu(t_{f,n,\nu},t')}e^{-i\Omega t'} \tag{3.16}$$

For the Fourier expression in the first integral, we use a delta function $\delta(2\pi/\omega = t_{f,n,\nu})$ to collapse the transformation onto the annihilation time, leading to the simplification

$$\varsigma_n^\nu = \frac{i\omega d^2}{2\pi\hbar V}\exp\left[i\left(n\omega t_{f,n,\nu} + A_{n,\nu} + (i\Gamma_d + \Delta_{NIR})\tau_{n,\nu}/\hbar\right)\right] \tag{3.17}$$

Here we define $\tau_{n,\nu} \equiv t_{f,n,\nu} - t_{o,n,\nu}$ as the time the e-h pair needs to be accelerated to produce the nth order sideband, $A_{n,\nu} \equiv -\int_{t_{o,n,\nu}}^{t_{f,n,\nu}} E_{e-\nu}(t)dt/\hbar$ is the dynamical phase accumulated by the e-h pair from the dispersion relation of the crystal, and $\Delta_{NIR} \equiv \hbar\Omega - E_g$ is the NIR detuning away from the energy gap, E_g, of the crystal. This expression greatly simplifies the relationships between the propagator and other experimental variables, and provides the opportunity to connect data to parameters of the quantum condensed matter system. However, as the next section will detail, this expression for ς_n^{ν} does not produce an analytical solution for an arbitrary HSG experiment.

3.2.2 Semiclassical Conundrum

Along with making these calculations more computationally intensive, the lack of an analytical solution for the semiclassical ς_n^{ν} has no explicit dependence on experimental parameters. Semiclassically, we can express the quasimomenta of both the electron and hole as

$$\begin{aligned} \hbar\dot{k} &= eF_{THz}\sin(\omega t) \\ k(t) &= \frac{eF_{THz}}{\hbar\omega}\left(\cos(\omega t_0) - \cos(\omega t)\right) \end{aligned} \tag{3.18}$$

Using the creation $(x(t_{o,,n,\nu}) = 0)$ and annihilation $(x(t_{f,,n,\nu}) = 0)$ condition, and the semiclassical expression for our quasiparticle's position can be written as

$$\ddot{x} = \frac{eF_{THz}}{m}\omega t \tag{3.19}$$
$$x(t) = \frac{eF_{THz}}{m\omega^2}\left(\omega(t - t_{o,n,\nu})\cos(\omega t_{o,n,\nu}) + \sin(\omega t_{o,n,\nu}) - \sin(\omega t)\right)$$

With the conservation of energy condition

$$\begin{aligned} \hbar^2 k^2 (t_{f,n,\nu})(2\mu_\nu)^{-1} &= n\hbar\omega \\ \left(\cos(\omega t_{o,n,\nu}) - \cos(\omega t_{f,,n,\nu})\right) &= \frac{n\hbar\omega^3}{e^2 F_{THz}^2} \end{aligned} \tag{3.20}$$

And the annihilation condition $\left(x(t_{f,n,\nu}) = 0\right)$

$$\begin{aligned} 0 &= \frac{eF_{THz}}{m\omega^2}\left(\omega\tau\cos(\omega t_{o,n,\nu}) + \sin(\omega t_{o,n,\nu}) - \sin(\omega t_{f,n,\nu})\right) \\ \cos(\omega t_{o,n,\nu})\omega\tau &= 2\sin(\omega\tau)\cos(\omega(t_{f,n,\nu} + t_{o,n,\nu}/2) \end{aligned} \tag{3.21}$$

Which leads to the relationship between $\omega t_{o,n,\nu}$ & $\omega t_{f,n,\nu}$

$$\cos(\omega t_{f,n,\nu}) = \sqrt{\frac{n\hbar\omega^3}{e^2 F_{THz}^2}} + \cos(\omega t_{f,n,\nu}) \tag{3.22}$$

Which is not analytically solvable.

In order to gain more insight on the influence of internal and external parameters, we will incorporate the linear in time approximation in the next Chapter. While seemingly greatly reduced from its original quantum form, the linear in time approximation reproduces exact numerical results with great accuracy, as is detailed in Figure 3.1. The figure compares these two methods of calculating values for the e and lh at three field strengths used in experimentation (70 kV cm^{-1}: Red, 53 kV cm^{-1}: Green, and

35 kV cm^{-1}: Blue) for three sideband orders observed in experiment (16th order: left column, 24th order, middle column, and 32nd order: right column). The x position of the e and hh from the initial exciton center of mass (top row), the quasi momentum of the e-hh pair (second row), the kinetic energy of the e-hh pair $E_{e-hh}(t) = \hbar^2 k^2(t)(2\mu_{e-hh})^{-1}$ (third row), and the dynamical phase of the pair $A(t_{o,n,hh}, t)$ (fourth row) are all calculated for the two $\mathbf{E}_{THz}(t)$ ($F_{THz}\sin(\omega t)$ (dashed lines) and $F_{THz}\omega t$ (solid curves)). The second y-axis of the second row depicts the explicit $\mathbf{E}_{THz}(t)$ used for the calculations of the corresponding curves of the same color and pattern.

3.3 EXPERIMENTAL MEASUREMENT OF ς_n^{ν} VALUES

While this hole species basis of HSG analysis might appear straightforward, there are some experimental subtleties which must be observed in order to ensure data from a particular experimental run gives the fullest insight. Previously in HSG experiments, Jones Matrix elements were measured up to an overall normalization factor. By incorporating PMT data into the data processing of HSG experimentation, we can scale the overall Jones Matrices at different sideband indices by the conversion efficiency of the GaAs crystal and HSG process. These values is related to the quantum mechanisms embedded in the magnitudes of ς_n^{ν}.

3.3.1 PMT/CCD Experiments for Hole Species Projection

A subtlety of moving from the Jones matrix element ratios of the previous Chapter to the unnormalized Jones matrix elements in Eq. 3.15 is that the measured values we want are not longer of order ~1 but rather decreasing with sideband order. The

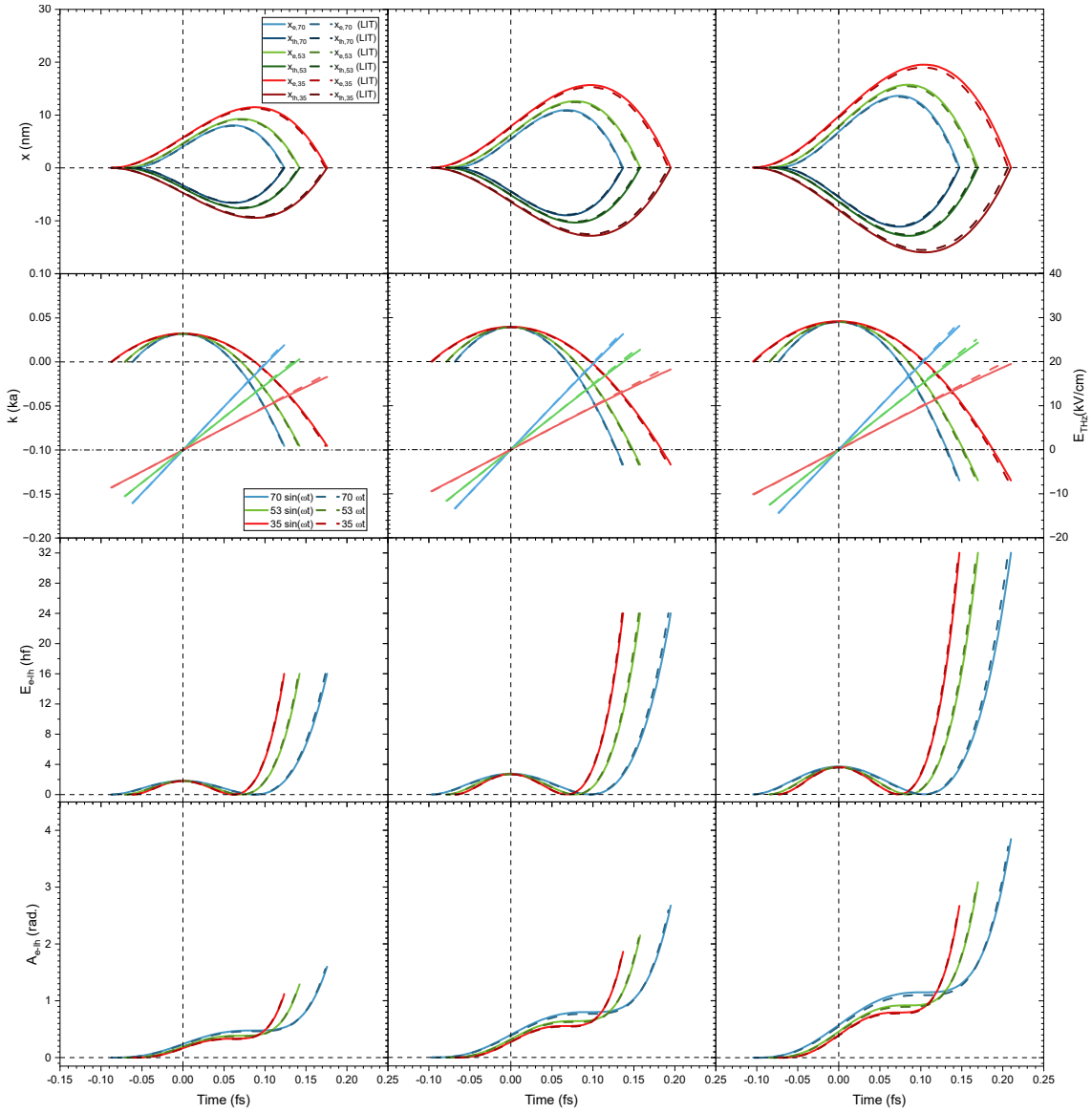

Figure 3.1 - Comparison of LIT Calculation and Sinusoidal Numerical Calculations of Quasiparticle Dynamics

A comparison of various values parameterizing the e-lh pair dynamics calculated using the LIT analytical method (solid curves) and numerical solutions for a sinusoidal THz field (dashed lines) at the three field strengths used in experimentation (70 kV cm^{-1}: Red, 53 kV cm^{-1}: Green, and 35 kV cm^{-1}: Blue). The three columns are for e-lh pairs being accelerated to different offset energies (left: 16th order, middle: 24th order, and right: 32nd order). The top row is the distance of the e or lh from the initial exciton center of mass, the second row is the quasimomenta of the e-lh pair in multiples of the lattice constant a = 5.5 Å, with the second y-axis depicting the $\mathbf{E}_{THz}(t)$ used for each calculation. The third row is the e-lh pair kinetic energy $E_{e-hh} = \hbar^2 k^2(t)(2\mu_{e-hh})^{-1}$, presented in multiples of the THz photon energy. The fourth row is the dynamical phase $A(t_{o,n,hh}, t)$ in radians.

magnitude of the Jones matrix elements should be close to the measured conversion efficiency of the sidebands. Looking at Eq. 3.13, the Jones matrix elements act as the conversion efficiency from incoming NIR light to outgoing sideband signal. The magnitude of an individual Jones matrix element, and, by extension, the magnitudes of the hole species contribution, are related to the measured sideband intensity.

Unfortunately, we don't measure the intensity of the sidebands when we measure their polarizations. The CCD is not calibrated to an overall intensity reading, so additional measurements are required to obtain the magnitude of the Jones matrix elements. We can measure the magnitude of the J_{xx} component in the PMT by exciting the sample with horizontally polarized NIR light and orienting the polarizer after the sample to be passing horizontally polarized light. Now the Jones matrix elements are measured up to an arbitrary phase, related to the NIR phase. Using the same unitary transformation $U(\phi)$ introduced in the previous Chapter, we are able to transform the scaled Cartesian Jones matrix elements into the circular basis. By having overlap with the sidebands measured in the CCD and in the PMT, this scaling of the Jones matrix elements can be extended to all the sidebands measured by the CCD in pulsed polarimetry. With the magnitudes of the Jones matrix elements, knowledge of the Bloch wavefunctions and simple algebra are all that is necessary to calculate ς_n^{ν}, as outlined in Eq. 3.15.

3.4 SCIENTIFIC SIGNIFICANCE

Converting our HSG polarimetry data to the hole species basis provides a more intuitive probe of the physics underlying our quasiparticle dynamics. Coupled to this simplicity is

the ability to separate contributions of the two different wavefunctions in our material to the overall sideband signal. To our knowledge this is not a capability available to most nonlinear optical probes.

With this wavefunction specific insight into our sample, there are many experiments available which could provide unique insight into the microscopic physics of the quasiparticles in bulk GaAs. Below are outlines of some of the experiments enabled by the hole basis analysis.

3.4.1 NIR Dependence

In Chapter 5, we will investigate the influence of the dynamical gap on our sideband signal. This comes from the $\Delta_{NIR} = \hbar\Omega - E_g$ term in the semiclassical calculation of the sideband polarization. By tuning the experimentally set Ω, we can in effect tune the detuning phase of each quasiparticle pair. By connecting the changing outgoing sideband polarization to the altered NIR wavelength, we can hone in on a value for the dynamical gap, E_g, which, to date, has been difficult to measure in driven systems.

3.4.2 Wavefunction Specific Picture of Measured Sideband Signal

By attributing characteristics of a sideband photon to either the hh or lh wavefunction, we can use our signal to examine individual characteristics of either wavefunction. An example of this would be dephasing between the crystal lattice and the quasiparticles. Joe Costello conducted temperature dependent probes of the sideband signal. As he increased the temperature for a given acquisition, he found the polarization of the sidebands remained similar, but the overall intensities of the sideband photons decreased. He connected this increase in intensity to a temperature dependent model of

dephasing, and, using the hole basis analysis, was able to report individual values for the hh and lh dephasing strengths.

We can also expand on the dynamical gap analysis to play with the nuance induced by incorporating a peak-splitting term between the hh and lh states. In the absence of strain, the hh and lh states should be degenerate at the band gap. The e-hh and e-lh pairs created with the same NIR photon energy should be seeing the same dynamical gap between the conduction and valence band. When strain is present on the GaAs sample, as is most certainly the case for our sample, there is a lifting of the degeneracy between the hh and lh states. In this instance, the e-hh and e-lh pairs would see different dynamical gaps, and the wavefunctions would carry these different detuning phases. Our hole state basis provides insight into these small differences in phase, which can impact our observed sideband signal.

3.4.3 Angle Dependence

The orientation of the THz electric field will tune the direction of the crystal lattice traversed by the quasiparticles. By propagating along different directions, the quasiparticles are seeing different dispersion relations, determined by the Luttinger Hamiltonian. Parameterized by the reduced mass of the e-h pair

$$\begin{aligned} \mu_{lh}(\theta) &= m_0 \left(m_c^{-1} + 2\gamma_1 + \gamma_2 |\, \mathbf{n}(\theta) \,| \right)^{-1} \\ \mu_{hh}(\theta) &= m_0 \left(m_c^{-1} + 2\gamma_1 - \gamma_2 |\, \mathbf{n}(\theta) \,| \right)^{-1} \end{aligned} \tag{3.23}$$

This effective mass parameter affects the ponderomotive energy $U_{p,\nu}$ of each e-h pair, which, as indicated in the equations above, alters the outgoing sideband signal.

Given our newfound sensitivity to the separate contributions of hh and lh species, we have access to the different reduced masses of the e-h pairs. This, in turn, offers access to disaggregate contributions from all three Luttinger parameters in the reduced mass terms of both e-h pairs. With a clear probe at the influence of the Luttinger parameters, we present in Chapter 6 our method to reconstruct the effective Hamiltonian of a quantum condensed matter system.

Chapter 4 — Interference of Bloch Waves

In 1899, Thomas Young demonstrated the wave-like nature of light by interfering two waves which entered from two different slits. The altering intensities of light appearing on a screen upstream was an example of interference between the two waves of light propagating from the two different slits. This double slit experiment was later replicated by another type of wave, a matter wave, with free electrons serving as the host for the matter waves [78, 79].

Waves are a physical phenomenon well described by complex numbers, meaning both real and imaginary numbers are used to describe their motion through space and time. This complex nature makes them difficult to measure, as imaginary numbers are

normally precluded from experimental measurement. What physicists normally measure is a projection of a two dimensional phenomena on the real and imaginary axis plane onto just the real axis. Physicists are constantly chasing the shadows of the imaginary phenomena.

Interference between two waves provides a measurable insight into *differences* between the complex propagation of two or more wavefronts. Specifically, if the two waves have different phases, the two will interfere and create an overall destruction in the total amplitude of the system. Like Thomas Young, physicists have utilized this phenomena to characterize the wave-like nature of systems.

Albert. A. Michelson invented a particular interferometer which still bears name in an attempt to disprove the hypothesis of the stationary luminiferous ether [80]. In a Michelson interferometer, incoming light is diverted into one of two arms via a beamsplitter. In both arms the lightwaves make a round trip in the arm, and are then coupled out by the same beamsplitter. Differences in phases accumulated by the lightwaves in either arm manifest in the form of interference detected after the out-coupling. As arm-lengths change, the interference pattern may also change. This measured relationship to interference and arm-length is called an interferogram.

The interferometry of light waves is still utilized, and is most famously being deployed by the Laser Interferometer Gravitational Observatory (LIGO) to detect gravity's influence on light traversing two 4 kilometer long arms [81]. Quantum Mechanics tells us light is not the only wavelike object in the universe, and in fact matter itself is wavelike at the proper energy and length scales. There is an expanding literature

of an array of optical experiments resolving the interference of different matter waves [2, 4, 82, 83]. Even with this wide-ranging fascination in matter wave interference, there has been a noted deficiency in interferometry experiments of coherently driven Bloch waves in solids. This is in part because these Bloch waves dephase on the order of picoseconds, even in ultra-pure conventional semiconductors like bulk GaAs. Such fast timescales place a constraint on the types of experiments which will yield a resolvable interferometry signal from Bloch waves in solids, and have stunted experimental efforts.

In Chapter 1, I outlined the current state of the art experimental sensitivities for HHG, which is an ultrafast experiment operating on the timescales requisite for coherently driven Bloch waves in solids. Here it is worth emphasizing that an inherent feature of HHG makes it difficult to act as interferometer of a few excited states. Because of the high field strengths necessary for HHG experiments, many different excited states are created in the solid under experiment. In the interferometry picture, where each of these different states acts as a different arm of a Michelson interferometer, the excitation mechanism of HHG is equivalent to building an interferometer with many, many arms [28, 84]. The resulting HHG signal may contain interference information of the multiple wave fronts [20], but it is difficult to connect a given signal to a particular characteristic of the Bloch waves.

In addition, in HHG both the intraband and interband polarizations are driven by the excitation pulse and contribute to the harmonics [27, 85-87]. For some systems of interest, these intraband currents have been attributed to an observed energy shift in the

harmonics, a so called “non-integer” harmonic [88]. All of these contributions complicate the microscopic picture of the signatures of interferometry observable in an HHG signal.

4.1 HSG POLARIZATION ACTING AS AN INTERFEROGRAM FOR MATTER WAVES

From the beginning, interferometry of matter waves has been an exciting avenue of experimentation because of the insight it provides into the nature of the constituent wavefunctions. If the mechanism of interferometry is so complicated, as it is in HHG, the resulting signal provides diminishingly little insight into the matter waves which are interfering. As you will read in this section, HSG polarimetry serves as a platform for interferometry of Bloch waves. Furthermore, the mechanism is so straightforward that it can be well described with an analytical, classical model of the quasiparticle dynamics. Such success with an analytical model is an incredible boon for experiment, as future experiments could be developed which can directly measure HSG polarization’s response to material parameters, especially those of interest in the broader community.

Depicted in Figure 4.1 is our microscopic picture of sideband generation, which should be familiar from Chapter 2, and our Michelson interferometer picture of sideband generation and polarization. A key difference between Fig 4.1 (A) and Chapter 2 is the inclusion of Roman numerals, which correspond with the numerals in Figure 4.1 (B) depicting the key steps for the Michelson interferometer picture of HSG. In Figure 4.1, both cartoons depict (i) the incident NIR pulse (ii) being split by the GaAs sample (the beam splitter in our interferometer) (iii) into one of two hole states (the arms of our interferometer). The arms of the interferometer are different lengths due to the different

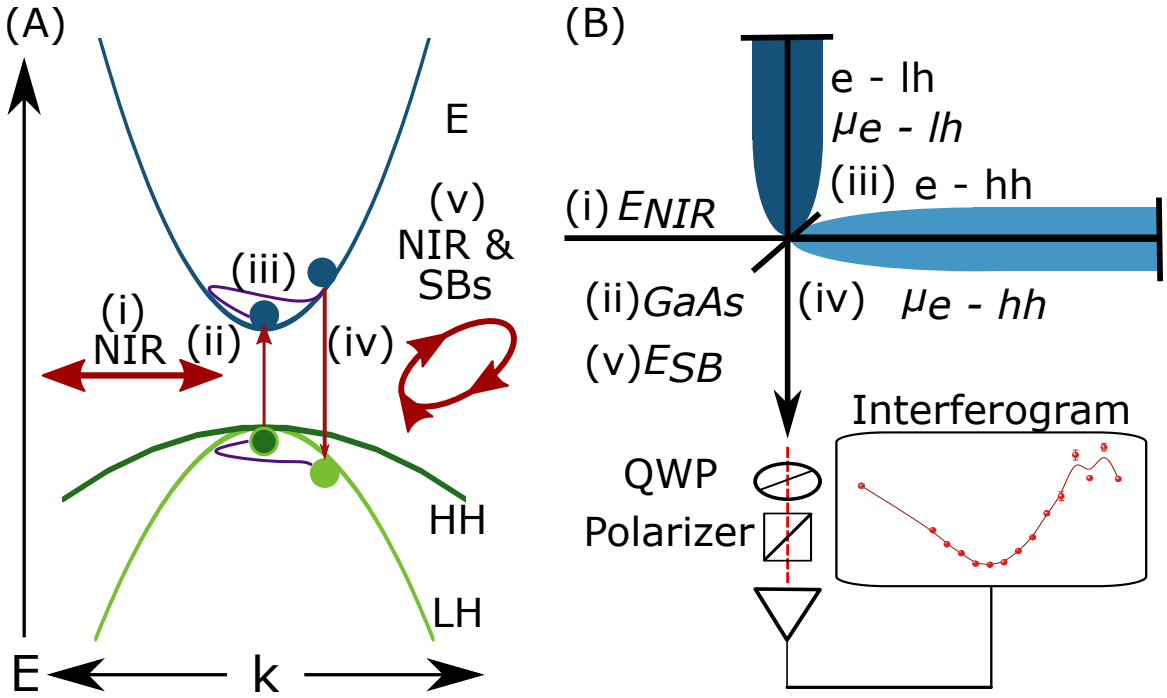

Figure 4.1 - the Microscopic Dispersion Picture and the Michelson Interferometry Picture of Sideband Generation and Polarization.

A) The microscopic picture of HSG, with the Energy versus quasi momentum relationship for the conduction electron (blue), hh band (dark green), and lh (light green) of bulk GaAs. The only feature not to scale is the gap between the valence and conduction band. The Roman numerals correspond with key steps in the Michelson interferometry picture also denoted with Roman numerals. B) A cartoon of the Michelson interferometry description of HSG polarization. An incoming NIR pulse (i) is split into the two arms of the interferometer by the GaAs lattice (ii), corresponding to the two types of e-h pairs. The arms of the interferometer have different lengths, corresponding to the different dispersion relations the pairs have traverse in order to emit a sideband of the same order. Because the two e-h pairs have different dispersion relations and effective masses, the arms in this picture are filled with media with different indices of refraction. After the e-h pairs traverse their respective arms, equivalent to their acceleration by the THz field, the GaAs couples out the pairs (iv) as either RHCP or LCHP light in the form of the SB electric field (v), whose polarimetry is then measured by our Stokes polarimeter. This, conducted for many sideband orders leads to our measured interferogram.

dispersion relations of the hh and lh bands, which require different acceleration times by the THz field to achieve the same offset energy and thus emit a sideband of the same order. The different dispersion relations also act like media with different indices of

refraction in the different arms (denoted by μ_ν). After the two matter waves finish their acceleration process, (iv) they annihilate and are out -coupled by the GaAs crystal (v) in the form of light, or high order sidebands. This outgoing sideband electric field is measured by our Stokes polarimetry apparatus, which registers the changing sideband polarization as a function of sideband order. We call this signal an interferogram because increasing the observed sideband order is equivalent to sending quasiparticles farther and farther in real and inverse space, or lengthening the arms of the interferometer.

4.1.1 Jones Matrix

We can use our Jones Matrix formalism developed in Chapter 2 in order to develop an expectation for how the sideband polarization signal will change as a function of sideband order *n* and other experimental parameters by incorporating an analytical version of the ς_n^ν values I developed in Chapter 3. First, we are going to rephrase the expressions for the NIR and sideband electric fields, in order to express them in terms of variables which are intuitive to HSG's optical selection rules.

As detailed in Chapter 2, the annihilation of the e-h pair will emit a photon with either RHCP or LHCP. For each hole state, the Bloch wavefunction will be in a superposition of angular momenta eigenstates, $\left|\pm 3/2\right\rangle$ & $\left|\mp 1/2\right\rangle$, one of which will emit a RHCP photon and one which will emit a LHCP photon. With this insight, the circular basis will inform us of the dynamics of Bloch wavefunctions in a basis which is synonymous with the distribution of angular momenta eigenstates of the wavefunctions. In the circular basis, we can express the normalized sideband electric field as

$$\left|\hat{\mathbf{E}}(n)\right\rangle \equiv \mathbf{E}(n)\cdot\|\mathbf{E}(n)\|^{-1} = r(n)\left|R\right\rangle + l(n)e^{i\phi(n)}\left|L\right\rangle \tag{4.1}$$

Here $r(n)$ and $l(n)$ are quantifying the normalized amount of light in the RHCP and LHCP basis, respectfully, with the condition $r^2(n)+l^2(n)=1$ for all sideband orders n. By focusing on the normalized electric field, our signal will focus on changes in polarization on the order of unity with respect to sideband order as opposed to the logarithmic falloff of electric field strength observed in GaAs high order sidebands. In this expression, $\phi(n)\equiv\phi_l(n)-\phi_r(n)$ is the relative phase difference between the LHCP and RHCP components of the sideband field. The individual phases of these components are defined with respect to the RHCP component of the NIR excitation, which, given the gauge freedom, is chosen to be set to zero.

We can reconstruct the sideband electric field in the circular basis using the Stokes parameters measured from the Stokes polarimetry process detailed in Chapter 2 using the expressions

$$\begin{aligned} r^2(n) &= \frac{1+\tilde{S}_3(n)}{2} \\ l^2(n) &= \frac{1-\tilde{S}_3(n)}{2} \\ \phi(n) &= \arctan\left(\frac{\tilde{S}_2(n)}{\tilde{S}_1(n)}\right) - 2\theta - \pi/2 \end{aligned} \tag{4.2}$$

Here θ is the THz-to[110] crystal axis orientation, and

$$\tilde{S}_i(n) \equiv S_i(n)/\sqrt{S_1^2(n)+S_2^2(n)+S_3^2(n)} \tag{4.3}$$

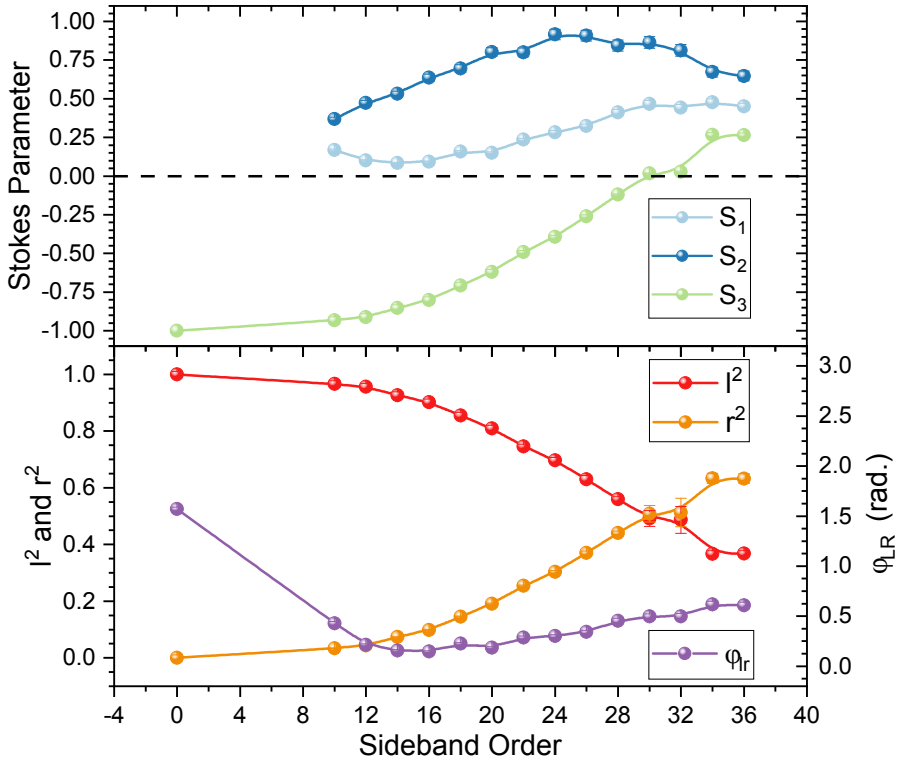

Figure 4.2 - Stokes Parameters and Reconstructed Sideband Electric Field. Top Frame: An example of the measured Stokes parameters of the sideband spectra. Stokes parameters are located directly underneath the corresponding sideband peak. Bottom Frame: The Stokes parameters is the representation of the sideband electric field in the circular basis, $\hat{\mathbf{E}}_n = l(n)e^{i\phi(n)}\left|L\right\rangle + r(n)\left|R\right\rangle$. Using Eq. 4.2, the measured Stokes parameters calculate the values for $r(n), l(n), \& \phi(n)$ displayed.

which allows for the normalization of $l(n)$ & $r(n)$ such that they are independent of the sideband intensity. Figure 4.2 depicts the measured Stokes parameter for a given polarimetry run, and the calculated $r^2(n), l^2(n), \& \phi(n)$ for an experimental run.

With this expression of the sideband electric field, and an equivalent expression for the NIR excitation, we can rewrite our Jones Calculus expression

$$\begin{pmatrix} r(n)e^{i\phi_r(n)} \\ l(n)e^{i\phi_l(n)} \end{pmatrix} = \begin{pmatrix} T_{++,n} & T_{+-,n} \\ T_{-+,n} & T_{--,n} \end{pmatrix} \begin{pmatrix} r_{NIR} \\ l_{NIR}e^{i\phi_{NIR}} \end{pmatrix} \tag{4.4}$$

For this work, we will only be calculating the Jones matrix elements using the methods outlined in Chapter 3, as opposed to Chapter 2, where the reconstruction of the Jones matrix elements and their ratios was the key experimental accomplishment. By measuring the values on the left side of the equation, and having experimentally set $r_{NIR}, l_{NIR}, \& \phi_{NIR}$, we have to develop a good model for ς_n^{ν}, robust to various experimental conditions, which calculates the $T_{ij,n}$ that predicts an outgoing sideband electric field which is in good quantitative agreement with experiment.

4.1.2 Bloch Wavefunction Dynamics Modeling the Phase of Sideband Polarization

If we go back to Eq 3.1, we can see how the values we predict for ς_n^i can calculate $T_{ij,n}$ and thus $\left|\hat{\mathbf{E}}(n)\right\rangle$ from a particular NIR polarization. However, the form of ς_n^{ν} in Eq. 3.12 is not analytically calculable. HSG polarimetry would ideally experimentally probe the sideband polarization's dependence on material parameters. Fortunately, approximations can be made to simplify Eq. 3.12.

4.1.3 LIT Approximation

In the semiclassical approximation of ς_n^{ν}, we argued most of the e-h pairs which contribute to a sideband signal are accelerated by less than one cycle of the THz field. Assuming this is the case, we can look at the form $\mathbf{E}_{THz}(t) = F_{THz}\sin(\omega t)$ during the window of time these e-h pairs are accelerated by the THz field. Numerical solutions provided by the annihilation conditions in Eq. 3.19 show the e-h pairs are accelerated for ~200 fs by the THz field before annihilating and emitting a sideband. Importantly, this

time window is located around the node of $\mathbf{E}_{THz}(t)$. With this narrow time domain around the node of the field, we can approximate the THz field as linear in time (LIT), or $\mathbf{E}_{THz}(t) \approx F_{THz}\omega t$.

With the LIT approximation, we can express the position of the electron or hole and the quasi momentum as

$$\begin{aligned} x(t) &= \frac{eF_{THz}}{m\omega^2}\left((\omega t)^3/3 - (\omega t_{o,n,\nu})^2\omega t + 2/3(\omega t_{o,n,\nu})^3\right) \\ k(t) &= \frac{eF_{THz}}{2\hbar\omega}\left((\omega t)^2 - (\omega t_{o,n,\nu})^2\right) \end{aligned} \tag{4.5}$$

And simplify the annihilation conditions in Chapter 1 to a form which is analytically solvable for a specific set of experimental conditions. First the position condition for annihilation

$$\begin{aligned} x(t_{f,n,\nu}) &= 0 \\ \omega t_{f,n,\nu}^3 - \left(\omega t_{o,n,\nu}^2\right)\omega t_{f,n,\nu} + 2/3\omega t_{o,n,\nu}^3 &= 0 \\ \left(t_{f,n,\nu}/t_{o,n,i}\right)^3 &= t_{f,n,\nu}/t_{o,n,\nu} - 2/3 \\ t_{f,n,\nu} &= -2t_{o,n,\nu} \end{aligned} \tag{4.6}$$

And then the energy conservation expression

$$\begin{aligned} \frac{\hbar^2 k^2(t_{f,n,\nu})}{2\mu_\nu} &= n\hbar\omega \\ \frac{e^2F_{THz}^2}{8\mu_\nu\omega^2}\left((\omega t_{f,n,\nu})^2 - (\omega t_{o,n,\nu})\right)^2 &= n\hbar\omega \\ \frac{3}{4}\left(\omega t_{f,n,\nu}\right)^2 &= \sqrt{\frac{8n\hbar\omega^3\mu_\nu}{e^2F_{THz}^2}} \\ -2\omega t_{o,n,\nu} = \omega t_{f,n,\nu} &= \frac{2}{\sqrt{3}}\left(\frac{8n\hbar\omega^3\mu_\nu}{e^2F_{THz}^2}\right)^{1/4} \end{aligned} \tag{4.7}$$

This also provides us with the expression for the unitless acceleration time

$$\omega\tau_{n\nu} = -3\omega t_{o,n,\nu} = \sqrt{3}\left(\frac{8n\hbar\omega^3\mu_\nu}{e^2F_{THz}^2}\right)^{1/4} \tag{4.8}$$

The expression in the parenthesis can be simplified to be in terms of the ponderomotive energy and the THz photon energy $E_{\gamma THz} \equiv \hbar\omega$,

$$\omega\tau_{n,\nu} = \sqrt{3}(2nE_{\gamma THz}/U_{p,\nu})^{1/4} \tag{4.9}$$

Which provides insight into what experimental parameters will alter the acceleration and annihilation time to produce a sideband of a particular order. With this analytical expression for the acceleration time, we can also derive an analytical expression for the dynamical phase

$$A_{n\nu} = -\int_{t_{o,n,\nu}}^{t_{f,n,\nu}} \frac{e^2F_{THz}^2}{8\hbar\omega^2\mu_\nu}\left((\omega t)^2 - (\omega t_{o,n,\nu})\right)^2 dt = \frac{2}{15}n\omega\tau_{n\nu} \tag{4.10}$$

Which we can then use to write ς_n^i completely in terms of experimental and material parameters

$$\varsigma_n^\nu = \frac{i\omega d^2}{2\pi V\hbar}\exp\left[i\sqrt{3}\left(\frac{8}{15}n + (i\Gamma_d + \Delta_{NIR})(\hbar\omega)^{-1}\right)(2nE_{\gamma THz}/U_{p,\nu})^{1/4}\right] \tag{4.11}$$

Given all these approximations, it is reasonable to question how accurate the resulting model of the quasiparticle dynamics actually is when compared to the quantum theory. The first proof will come from comparing the values calculated by the LIT approximation analytically and the values calculated using numerics with a sinusoidal THz field. Figure 3.1 compares these two methods of calculating values for the e and hh.

Qualitatively and quantitatively, the values calculated analytically from the LIT approximation and the values calculated numerically from the sinusoidal field nearly match, as demonstrated above. Figure 4.3 shows values calculated using both the LIT approximation (dashed lines) and the sinusoidal field (solid lines) for the e-hh (left column) and e-lh pairs (right column) which produce the 24th order sideband when driven by the three THz field strengths used in experiment (70 kV/cm (blue), 52.5 kV/cm (green), and 35 kV/cm (red)). The slight differences are exacerbated at higher sideband orders and lower field strengths, most visible in Figure 4.3 with the red curves having greater differences than the green and blue curves. As the creation and recombination times get farther away from the node of the THz field, the LIT approximation becomes less effective, which is the case for the increasing acceleration times required for higher orders and lower F_{THz}.

With this analytical model replicating values calculated by a more exact model of the quasiparticle dynamics, we move to our next proof point in the LIT approximation: using the values of ς_n^i predicted by Eq. 4.11 to accurately predict the outgoing sideband polarization observed in experiment.

4.2 FIELD DEPENDENT PROBE OF SB POLARIZATION

Looking at the expression for ς_n^i in Eq. 4 11, we can see an F_{THz} dependence embedded in the expression of the ponderomotive energy. Therefore, all other experimental conditions being held constant, tuning the F_{THz} used to accelerate the quasiparticles should produce sidebands of the same order with different polarizations. Looking at the fourth row of

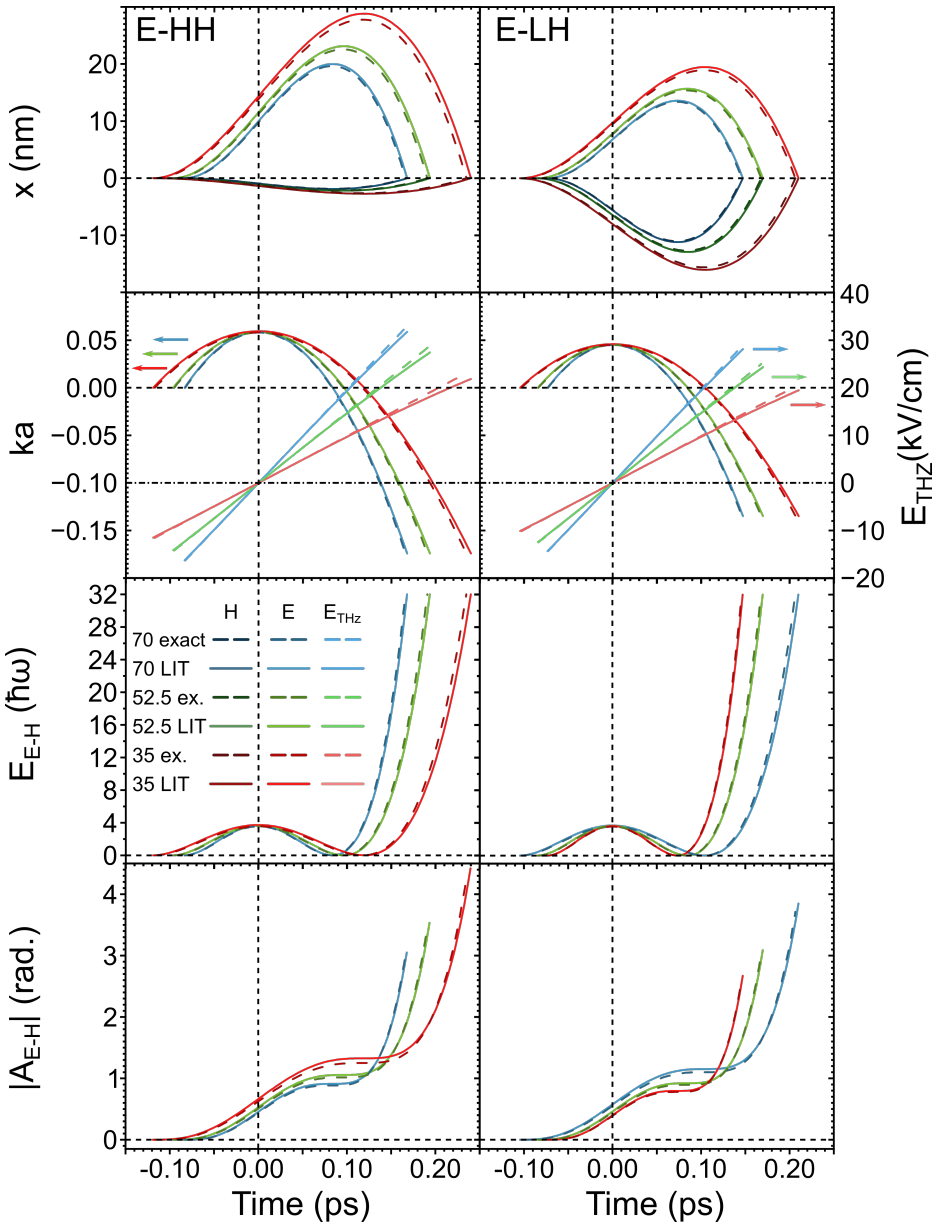

Figure 4.3 - Comparison Between LIT and Sine Wave Calculation.
Values calculated from LIT (dashed line) and numerical solutions of a sinusoidal (solid line) THz field for E-H pairs which produce a 32nd order sideband. The different field strengths used in experiment, 70 kV/cm (blue), 52.5 kV/cm (green), and 35 kV/cm (red), are all displayed. The left column holds the values for the E-HH pairs, and the right holds the values for the E-LH pairs. The top row holds the calculated x-position for the holes (dark colors) and electrons (light colors). The second row hold the calculated wave vectors for the electrons (downward parabolas, associated with the left y-axis, a = 5.56 Å) and the THz fields (lines, associated with the right y-axis). The third row holds the calculated E-H pair kinetic energy. The bottom row holds the calculated absolute values of the E-H pair dynamical phase.

Figure 4.3, this knob of F_{THz} can be viewed as producing sidebands with quasiparticles having different $A_{n,i}$. This provides us a convenient and easily manipulable experimental probe to test this theory of sideband polarization as an interferogram between two Bloch waves. If the LIT approximation validly describes the Bloch wave dynamics in bulk GaAs, then it should also model the change in sideband polarization as a function of F_{THz}.

4.2.1 Observed and Predicted Polarizations

We can break up the expression for ς_n^i into two parts: one which is oscillating, and one which is exponentially decaying, which we can express as

$$\varsigma_n^\nu \propto e^{i\Theta_\nu(n)} e^{-\Gamma_d \tau_{n,\nu} \hbar^{-1}} \tag{4.12}$$

Here

$$\begin{aligned} \Theta_\nu(n) &\equiv n\omega t_{f,n,\nu} + A_{n,\nu} + \Delta_{NIR}\tau_{n,\nu}\hbar^{-1} \\ &= \left(8n/15 + \Delta_{NIR}/\hbar\omega\right)\sqrt{3}(2nE_{\gamma THz}/U_{p,\nu})^{1/4} \end{aligned} \tag{4.13}$$

This expression indicates there is one part of the oscillating term which goes as $n^{5/4}$ and is dependent on the quasiparticle dynamical phase and the Fourier transform, and another which goes as $n^{1/4}$ and is dependent on the NIR detuning. Also, there an exponential damping to the oscillations which is dependent on the dephasing value, and operates as the fringe contrast on our interferogram signal.

Using this form of ς_n^ν in the expression for the Jones matrix elements in Eq. 3.14, we can predict the polarization of the sideband field parameterized by $l^2(n)$ & $\phi(n)$. These predictions and experimental results are displayed in Figure 4.4, ($l^2(n)$: top row,

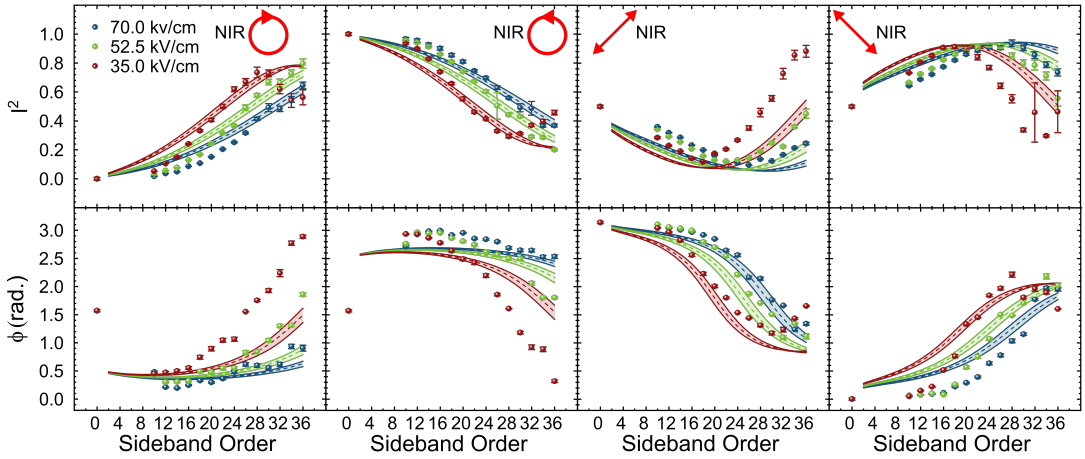

Figure 4.4 - Experimental Measurements and LIT Predictions of $\hat{\mathbf{E}}(n)$ With Unique NIR Polarization and Varying Thz Field Strength

Measurements of Bloch-wave interferograms present in the sideband electric field $\hat{\mathbf{E}}(n) = r(n)\left|R\right\rangle + l(n)e^{i\phi(n)}\left|L\right\rangle$ observed with four different NIR polarizations (RHCP: first column, LHCP: second column, Diagonal: third column, and Antidiagonal: fourth column) and three different THz field strengths (70 kV cm^{-1}: Red, 53 kV cm^{-1}: Green, and 35 kV cm^{-1}: Blue). The polarization is parameterized by $l^2(n)$ (top row) & $\phi(n)$ (bottom row). The dashed-dot lines overlayed in the same color are the theoretical predictions of polarization stemming from the LIT version of ς_n^{ν}. The bands are from a 5% error in THz field strength. In the calculations for these curves $\Gamma_d = 4.7\hbar\omega$ and $\Delta_{NIR} = 0$.

$\phi(n)$: bottom row) using four different NIR polarizations (RHCP: first column, LHCP: second column, Diagonal: third column, and Antidiagonal: fourth column) and three different field strengths (70 kV cm^{-1}: Red, 53 kV cm^{-1}: Green, and 35 kV cm^{-1}: Blue). There are a few characteristics of this plot of experimental data (scatter plots connected with spline curves) and theoretical curves (dashed-dot curves, with bands indicating 5% error in THz field strength) worth examining in detail:

The expected dependence on NIR polarization - Such a result is expected, given the HSG literature, and is more a confirmation of the use of Jones matrices to map different NIR polarizations into outgoing sideband polarization states.

The changing polarization as a function of sideband order *n* - In all 24 experimental curves presented in Figure 4.4, none are constant with sideband order. This is a departure from the results in Chapter 2, where the polarization measurements where measuring a value which was constant with sideband order. In Chapter 2, this value was connected to an individual Bloch wavefunction, which in our system is constant in $|k|$, analogous to being constant with sideband offset energy, or order n. For the experiments in this Chapter, we are observing something about the Bloch wavefunctions which changes with $|k|$, and we hypothesize it the increasing difference in dynamical phase which leads to this change in sideband polarization as a function of n.

The dependence on F_{THz} - In all eight panels, tuning the F_{THz} used to accelerate the quasiparticles leads to different observed sideband polarizations. Qualitatively, Eq. 4.11 predicts the dynamics of the Bloch waves to be inversely proportional to F_{THz}**.** *The lower the field strength, the greater the variation in phase of the Bloch waves as a function of sideband order*. This is visible in Figure 4.4, where, for all eight panels of experimental data, the lower field strength data sets all oscillate more rapidly as a function of sideband order.

The fringe contrast for the RHCP and LCHP NIR data sets - The fringe contrast features for our interferometry signal are most apparent for the 35 kV cm^{-1} dataset in the RHCP and LHCP data sets, where the $I^2(n)$ data do not oscillate between 0 and 1, but rather dampen to some intermediate value. This

behavior is dependent of the values of dephasing in the exponential dampening term on Eq. 4.12.

Qualitatively, the theoretical predictions from the LIT approximation demonstrate the same behavior. Quantitatively. The dashed dot curves in Figure 4.4 demonstrate good overlap with the experimental data. It should be noted for the 24 curves calculated, there is only one free parameter toggled: the dephasing rate. For all the theoretical curves plotted, the values of $\Gamma_d = 4.7\hbar\omega$ and $\Delta_{NIR} = 0$ were used in calculations of ς_n^{ν}.

Along with overlapping experimental data and theoretical curves, the LIT approximation provides one more insight which can demonstrate the validity or lack thereof for the model. At first glance, the datasets taken with the same NIR polarization but different field strengths look like they *could* overlap if the x-axes of the different sets were scaled by a particular factor. The LIT approximation provides this factor.

4.2.2 LIT Scaling Law for Field

Looking at Eq. 4.12 and 4.13, the phases of the Bloch waves evolve with terms dependent on $(n^5 F_{THz}^{-2})^{1/4}$ and $(n F_{THz}^{-2})^{1/4}$. The former is the expression related to the Fourier transform and dynamical phase, which is the focus of this Chapter. The later is related to the contributions from Δ_{NIR}, and will be further investigated in the next chapter.

By scaling the x-axes of the datasets by a multiple of the relative field strength factor predicted by the LIT approximation, $n \cdot \lambda^{-2/5}$, where $\lambda \equiv (F_{THz}/70\text{kV} \cdot \text{cm}^{-1})$, the x-axes of the scaled datasets will represent a constant dynamical phase for a given

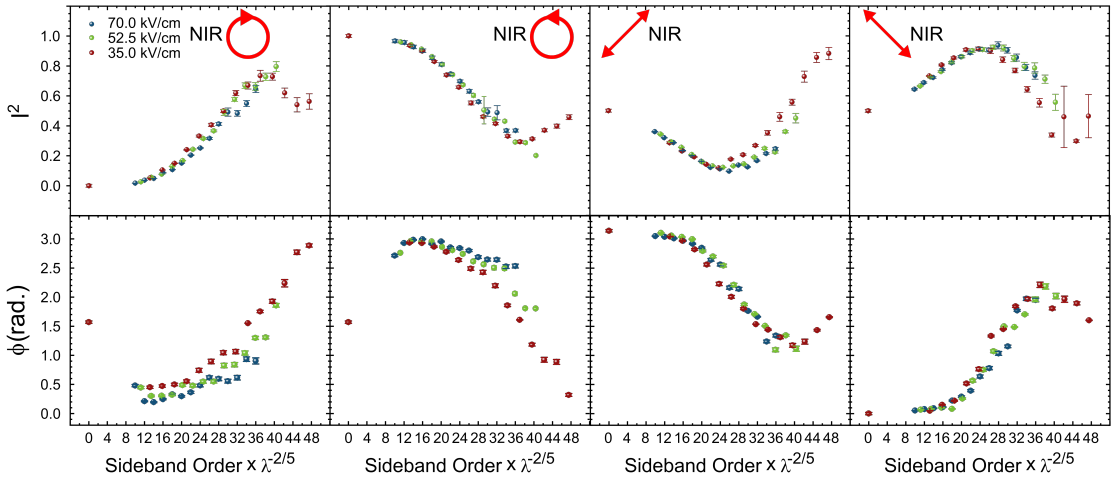

Figure 4.5 - Scaled Experimental Measurements of $\hat{\mathbf{E}}(n)$ Using Dynamical Phase Field Dependent Scaling Law Predicted by Lit Approximation
Measurements of $\hat{\mathbf{E}}(n) = r(n)\left|R\right\rangle + l(n)e^{i\phi(n)}\left|L\right\rangle$ presented in Figure 4.3. The sideband orders (x-axis of Figure 4.3) of datasets taken at different field strengths are scaled by a multiple of the relative field strength factor $n \cdot \lambda^{-2/5}$ ($\lambda \equiv (F_{THz}/70\text{kV} \cdot \text{cm}^{-1})$). The LIT approximation predicts this will lead to an x-axes equivalent to a constant dynamical phase for all datasets, and the Michelson interferometry picture of HSG would predict this scaling would cause the different datasets to overlap in each panel.

polarization state. If the dynamical phase difference between Bloch waves is what leads to a change in polarization, and the LIT has an accurate prediction of the changing sideband polarization, the datasets should overlap. Figure 4.5 presents the scaled datasets, and the overlap of datasets in each panel indicates the accuracy of the LIT approximation and the Michelson interferometry description of changing sideband polarization.

With a straightforward, analytical model of the Bloch wavefunction dynamics, we accurately modeled the qualitative and quantitative behavior of the sideband polarization as a function of sideband order and THz field. The agreement is only the beginning of the success of this paradigm, as these promising experimental results open up a wide array of related microscopic physics in solids which can be probed using this method. The

analytical form of our description allows for straightforward mechanisms to measure the influence of and extract from experiment key material parameters of interest.

4.3 MORE KNOBS TO TUNE

Looking at Eq. 4.11, ς_n^{ν} are dependent on more than just F_{THz}. We could even argue the other dependencies are more interesting, as they are inherent to the sample. Whereas $\mathbf{E}_{THz}$ is an external influence of the quasiparticle trajectories, material parameters like the dynamical gap, crystal lattice dephasing, and the effective Hamiltonian parameters also affect the trajectories. Given the success of the analytical LIT approximation of sideband polarization, we now have a mechanism to observe the influence of material parameters on the interference of Bloch waves and extract their values. Below, I will sketch a few of the most promising at-hand interferometry experiments which could extract relevant effective Hamiltonian parameters. The first, the quasiparticle to crystal lattice dephasing, has been studied extensively by my two colleagues, Joe Costello and Qile Wu. The second and third, the dynamical gap and Luttinger parameters, respectively, will form the remainder of this thesis.

4.3.1 Dephasing Constant

The dephasing contribution to sideband signal, as depicted in Eq. 4.11, occupies a unique position in the exponential term. Specifically, it is the only factor we have contributing to the attenuation of the sideband signal. Because this chapter dealt entirely with the normalized electric field, this behavior of the dephasing did not manifest in the experimental data in this chapter. However, other HSG works have looked into various

expressions of quasiparticle dephasing, and demonstrated ways to extract these values experimentally.

Recent HSG experiments have used the LIT expression for ς_n^{ν} to investigate the temperature dependent behavior of dephasing, $\Gamma_d(T)$, by isolating contributions of the HH and LH as a function of temperature.

Theoretical explorations of the quasiparticle dynamics resulting in HSG have incorporated higher order contributions from the THz field, complex recombination dynamics, and quasi momentum dependent dephasing.

4.3.2 NIR Dynamical Gap

For the purposes of this chapter, Δ_{NIR} was assumed to be constant, and for all intents and purposes was a constant frequency offset in experimentation. By changing the frequency of the NIR field, Ω, the NIR detuning now becomes an independent experimental variable, $\Delta_{NIR}(\Omega)$.

By running the same field dependent scans at multiple NIR excitation frequencies, the HSG polarimetry data becomes a two dimensional dataset which can be used to determine the dephasing constant and the dynamical gap. Assuming the dephasing is not quasimomenta dependent, a single value for the dephasing should describe the quasiparticle dynamics for these data sets. The only value which would tune the output sideband polarization as a function of NIR frequency is $\Delta_{NIR}(\Omega)$. The analytical nature of Eq. 4.11 provides a direct measurement of this dynamical gap from experimental data.

4.3.3 Luttinger Parameters

As Eq. 4.8 demonstrates, the values of these dynamical processes are all dependent on the ponderomotive energy of the quasiparticles in the THz field, which in turn is dependent on the effective mass of the e-h pair. This effective mass is determined by the specific dispersion relation of the electron and hole, defined along the crystal direction traversed by the quasiparticles. In a system with broken rotational symmetry like that of bulk GaAs, sending the e-h pair along different crystal directions should alter the outgoing sideband polarization due to a changing dispersion relation. This the Luttinger Hamiltonian, this change in dispersion relation and effective mass are quantified by the three Luttinger parameters.

The next layer of Bloch wavefunction interferometry would incorporate experiments conducted at different THz-to-crystal axis orientations. Coupled with information about the dephasing and dynamical gap already determined in the previous two experiments, the effective mass is the unknown parameter altering sideband polarizations. Using the expression for the effective mass in the Luttinger Hamiltonian in Eq. 1.6, one can reconstruct the scalar Luttinger parameters of bulk GaAs.

Chapter 5 — Dynamical Gap Measurement

Concurrent with measurements done in the previous chapter, we were observing the dependence of our HSG signal on NIR wavelength. Figure 5.1 displays data taken during our experiments detailed in Chapter 2 and [63]. Redoing our polarimetry experiments with slightly altered NIR excitation conditions lead to measurably different sideband signal. This sensitivity to NIR excitation wavelength is expected in the LIT approximation of the propagator ς_n^{ν}, displayed in Eq. 4.13, and provides a probe of the dynamical gap.

Such a parameter is difficult to measure, as common measurements of the gap, like absorbance, are obscured by excitonic effects (see Figure 5.2). Furthermore, these

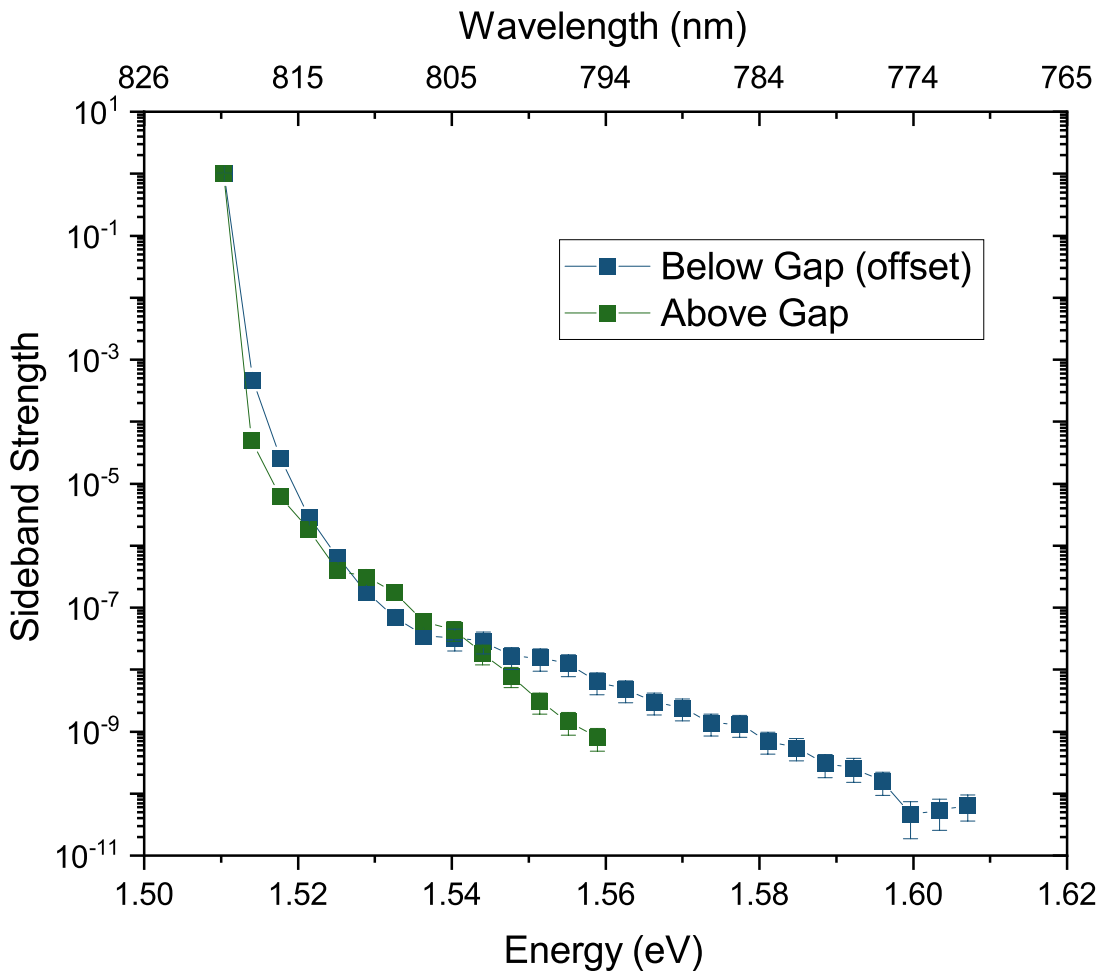

Figure 5.1 - Varying Sideband Conversion Efficiency With Different NIR Excitation Wavelength

Sideband strength (conversion efficiency) normalized to the laser line. This data was taken on the bulk GaAs sample used for Bloch wave reconstruction in Chapter 2, taken at $\theta = 90$ degrees and 65 K. The below gap excitation (blue line, $\lambda_{NIR} = 823$ nm) and above gap excitation (green line, $\lambda_{NIR} = 821$ nm) are determined with respect to the exciton peak in the absorbance spectra (inset).

experiments are normally conducted on equilibrium systems [47, 48, 50, 51]. By comparing experimental results to those predicted by the LIT approximation of the propagators, we present a preliminary measurement of the dynamical gap for bulk GaAs. Additionally, we get better agreement between datasets taken at different datasets and historical values of the band gap bulk GaAs [44, 45] when an energy splitting parameter,

δ_ν = 1.5 meV, is incorporated into the LIT calculation. Sensitivities to the dynamical gap, and differences in the energy gap of different quasiparticle species, makes future NIR dependent HSG polarimetry a potential non-destructive probe of quantum materials theorized to be a part of Majorana Zero Mode (MZM) systems. In bulk GaAs, preliminary analysis has used HSG polarimetry data to reconstruct a dynamical gap of E_g = 1.508 eV, with a peak splitting parameter of δ_ν = 1.5 meV.

5.1 QUASIPARTICLE PAIRS OF VARIOUS ENERGIES AND PHASES

Experiments detailed in this Chapter were conducted on two samples of bulk GaAs. Figure 5.2 shows the absorbance spectra of the two samples, indicative of the energy gaps for the hh and lh states in both samples. By tuning the output frequency from the M2 NIR laser cavity, we can tune the excitation energy of the quasiparticle pairs. This excitation dependent detuning

$$\Delta_{NIR}(\Omega) = \hbar\Omega - E_g \tag{5.1}$$

Is the term present in the expression for ς_n^ν in Eq. 4.11. In this expression, E_g is what we call the dynamical gap.

Like tuning the field strength in the previous Chapter, tuning the NIR excitation should tune the output polarization of the sideband electric field. Furthermore, with enough probes at different NIR wavelengths, quantitative analysis reveals a measurement of the dynamical gap term E_g, the one constant for all of the excitations. Most enticingly,

introducing a term which splits the energy scale of the hh and lh states, δ_ν, we can write the detuning term

$$\Delta_{NIR,\nu}(\Omega) = \hbar\Omega + E_g \pm \delta_\nu/2 \tag{5.2}$$

With this extra expression, we get quantitatively better agreement between our experimental data and the calculated sideband polarization.

As the previous Chapter discussed, the LIT approximation anticipates a scaling relation among data taken at different F_{THz}, contingent on the sideband polarization evolving like dynamical phase and annihilation times, following a $n^5 F_{THz}^{-2}$ relation. In the full expression for ς_n^ν, the Δ_{NIR} term also is multiplied by a ratio of n & F_{THz}, this one being $n F_{THz}^{-2}$. With this in mind, HSG polarimetry data taken under conditions where $\Delta_{NIR} \approx 0$ should show qualitatively well overlapped scaling in a reconfigured state similar to Figure 4.5 For those excitons excited far from the gap, Δ_{NIR} is tuned decidedly away from zero; more interesting physics ensue. In this regard, scaling polarimetry data as $n \cdot \lambda^{-2/5}$ should produce less of an overlap, given the inclusion of a $n F_{THz}^{-2}$ term.

5.1.1 Two Samples With Different Local Physics

In this chapter, we present data taken with two unique samples, produced from different fabrication runs. As the absorbance data in Figure 5.2 demonstrates, these two samples have measurably different local physics, as indicated by the exciton peaks. Data presented in the rest of this chapter will affirm this conclusion from the absorbance spectra, and demonstrate the sensitivity of HSG to the microscopic physics of a particular sample. Sample 1, which was the sample used for data in Chapter 4, underwent NIR

dependent polarimetry for seven wavelengths selected near the exciton peaks in the absorbance spectrum, denoted by the dashed lines. Sample 2 was fabricated for later experiments, and underwent more finely swept NIR excitations at two different crystal angles.

5.1.2 Absorbance To Determine Relevant Energy Scales

Strain is known to distort the band structure of bulk GaAs. The level of strain is specific to the van-der-Waal bonding process used to make our samples, which will vary from fabrication to fabrication. As a result, the two samples have noticeably different energy scales. These differences can be measured through absorbance measurements, such as the ones displayed in Figure 5.1. Through these measurements, we can determine the relevant NIR wavelength energies, based on where we see the exciton peaks.

The observed exciton peaks, which are close to the known 0 Kelvin gap of GaAs (1.519 eV) served as the center wavelength for these NIR probes. Redshifted excitation wavelengths are considered “below the gap”, and blue-shifted excitation wavelengths are considered “above the gap”. This terminology was adopted before Dynamical gap analysis, and preliminary data analysis indicates the gap is actually significantly lower in energy than the exciton peaks of the absorbance spectra would suggest, if there is no inclusion of a gap splitting term δ_ν.

5.2 ANALYSIS OF THE DYNAMICAL GAP

Sideband polarizations from both samples demonstrate sensitivity to the energy of the NIR excitation, with steps on the order of 0.5 nm (~1 meV) producing significantly

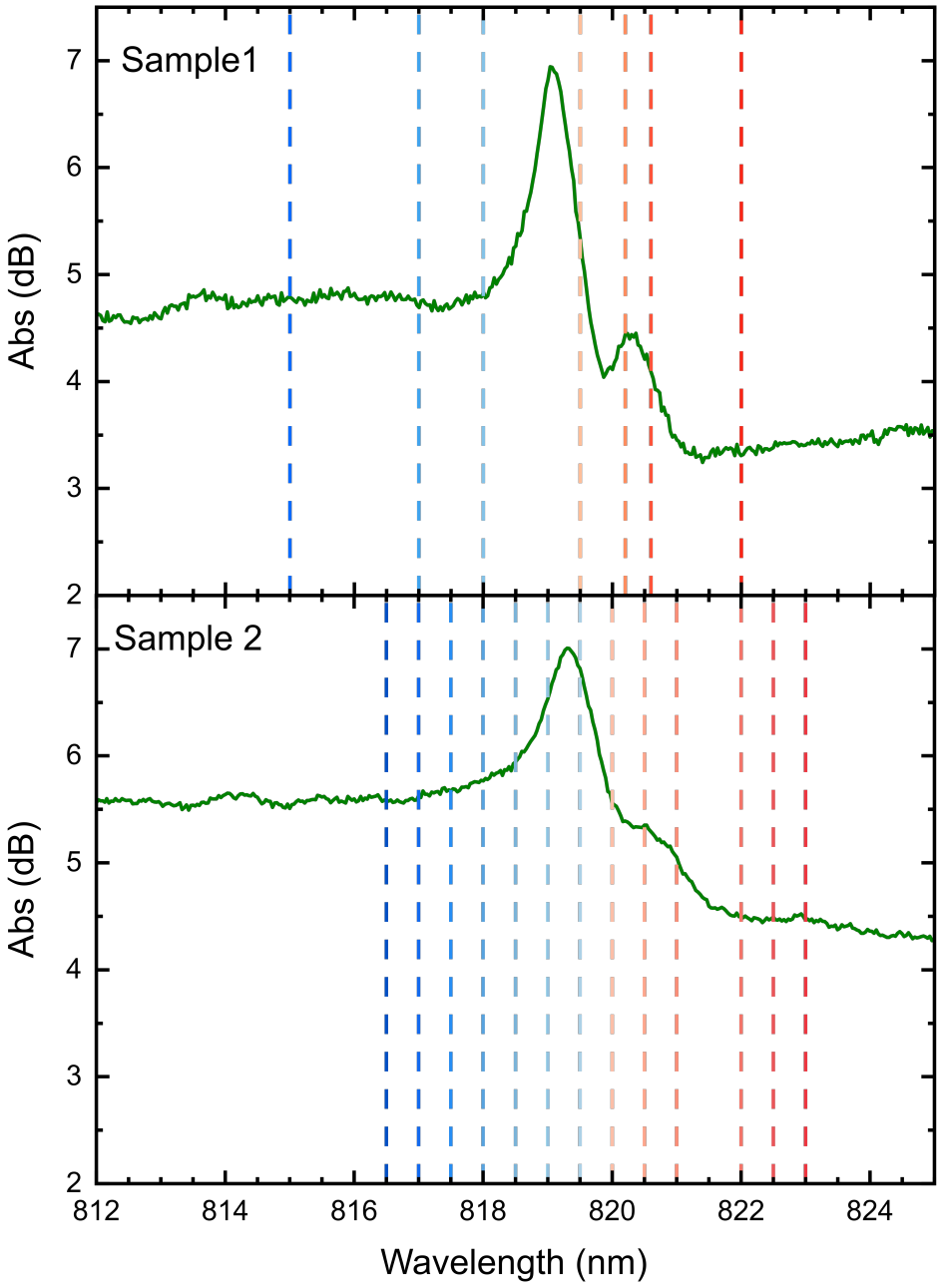

Figure 5.2 - Absorbance Measurements on Samples Used for NIR Dependent hSG Polarimetry

Absorbance data for Sample 1 (above) and Sample 2 (below). The experiments were conducted at the same temperature as HSG polarimetry experiments (35 K for Sample 1, 25 K for Sample 2). The colored dashed lines correspond to the colored curves in Figures 5.3 and 5.4, for HSG polarimetry data taken at different wavelengths.

different polarization states. Sensitivity to quasiparticle energies at this scale is necessary

to characterize future quantum devices, and is greater than the expected thermal broadening of ~2 meV from fluctuations at 25 Kelvin.

Quantitatively robust calculations are still being undertaken, however, preliminary analysis reveals a dynamical gap of approximately 1.501 eV (825.6 nm) when no peak splitting parameter is included, which is red-shifted significantly from literature values [44]. When a splitting value $\delta_\nu = 1.5$ meV is included in the LIT calculation of ς_n^ν, the analysis produces a dynamical gap of 1.508 eV (822nm), which is much closer to the literature value of 1.51 eV. This analysis, conducted on Sample 1, is robust to the individual wavelengths probed in experimentation.

5.2.1 Polarimetry With Different NIR Wavelengths

The effects of the dynamical gap on the sample can be seen through two plots. One is by looking at the behavior of the sideband polarization as a function of sideband order, with the different NIR excitation wavelengths being plotted as separate curves on the same plot as is Figure 5.3 for Sample 1, and Figure 5.4 for Sample 2. Visually, the sideband polarizations change as the NIR excitation is tuned from shorter (cool colored curves) to longer (warm colored curves) wavelengths. Across two samples, two THz orientations, and four NIR excitation polarizations, all observed sideband polarization demonstrate a dependence on the wavelength of the NIR pulse.

Figure 5.3 displays data from sideband polarimetry experiments on Sample 1, with the top row displaying the observed $l^2(n)$ of the normalized sideband electric field, $\hat{\mathbf{E}}(n)$, and the bottom row displaying the phase delay between the LHCP and RHCP components, $\phi(n)$. Each column is a different NIR excitation polarization (LHCP, first;

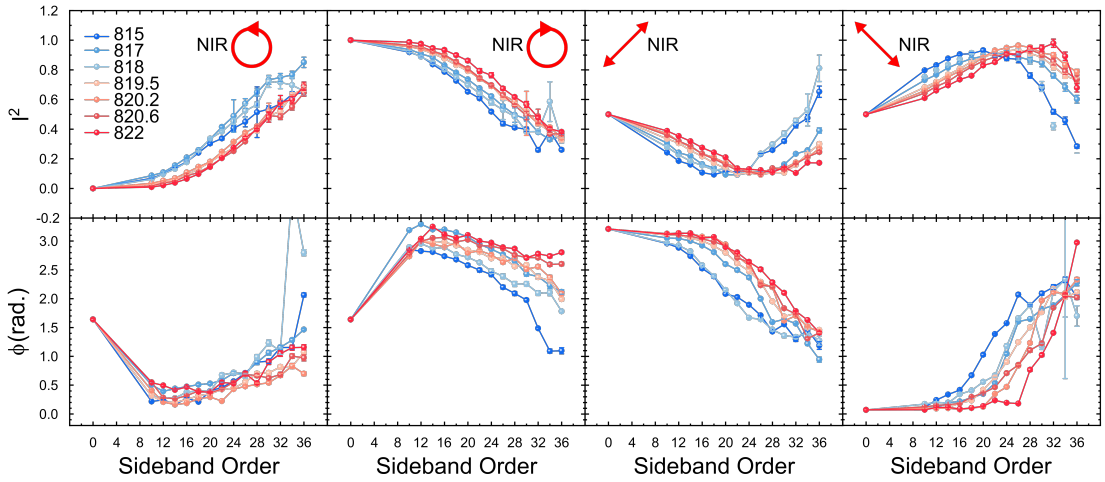

Figure 5.3 - Measurements of $\hat{\mathbf{E}}(n)$ as a Function of Sideband Energy (Sample 1), With Varying NIR Polarization and Wavelength
Measurements of $\hat{\mathbf{E}}(n)$ as a function of sideband order, parameterized with $I^2(n)$ (top row) and $\phi(n)$(bottom row), from HSG experiments on Sample 1. Each column is a different NIR polarizations (RHCP: first column, LHCP: second column, Diagonal: third column, and Antidiagonal: fourth column, upper insets). The cool to warm color scale of the curves indicate shorter to longer wavelengths of NIR excitation. The specific wavelengths are defined in the legend and correspond to the absorbance spectrum in Figure 5.2 A.

RHCP, second; Diagonal, third; Antidiagonal, fourth, upper inset). For all the data displayed, the [110] crystal axis was at an 88 degree angle with respect to the THz electric field, the sample was held at 35 K, and F_{THz} = 70 kV/cm.

Figure 5.4 displays similar data, taken on Sample 2. Here the four columns display four different polarimetry experiments. The first and third are data taken with a diagonally polarized NIR excitation pulse, and the second and fourth are data taken with an anti diagonally polarized NIR excitation. The first two columns are taken with A THz-to-[110] crystal axis orientation of 45 degrees, and the latter two are taken with a relative orientation of 90 degrees. In all data displayed for Sample 2, the sample was at 25 K for HSG experimentation, and F_{THz} = 70 kV/cm.

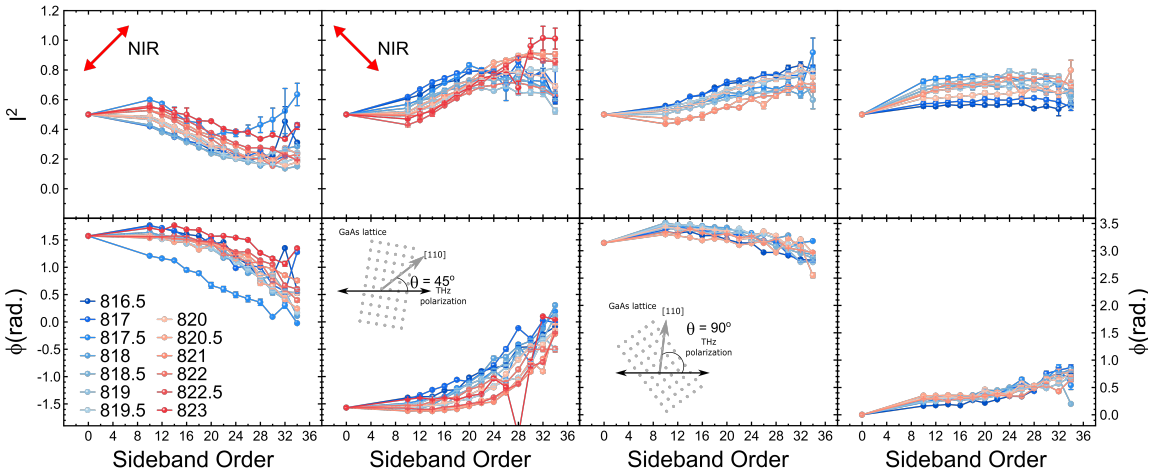

Figure 5.4 - Measurements of $\hat{\mathbf{E}}(n)$ in as a Function of Sideband energySample 2, With Varying NIR Polarization and Wavelength, at Different Crystal Angles
Measurements of $\hat{\mathbf{E}}(n)$ as a function of sideband order, parameterized with $I^2(n)$ (top row) and $\phi(n)$(bottom row), from HSG experiments on Sample 2. Each column is a different NIR polarizations (Diagonal: first column, Antidiagonal: second column, Diagonal: third column, and Antidiagonal: fourth column, upper insets). The cool to warm color scale of the curves indicate shorter to longer wavelengths of NIR excitation. The first two columns are data taken with the [110] crystal axis oriented 45 degrees with respect to the THz (inset, lower second column), and the latter two columns taken with the [110] crystal axis oriented at 90 degrees (inset, lower third column). The specific wavelengths are defined in the legend and correspond to the absorbance spectrum in Figure 5.2 B.

Plotting the sideband polarization as a function of the NIR wavelength provides more insight into the behavior of the experimental data. Figure 5.5 shows the experimental data from Figure 5.3, where the $I^2(n)$ & $\phi(n)$ of the sideband fields observed in Sample 1 are replotted as a function of NIR excitation wavelength. Here the curves are the polarization states of the different sideband photons, moving from the lower order sidebands (cooler colors) to the higher order sidebands (warmer colors). The four columns correspond to different sideband polarization states, matching the format of Figure 5.3. Figure 5.6 follows the same convention, recasting the data of Figure 5.4.

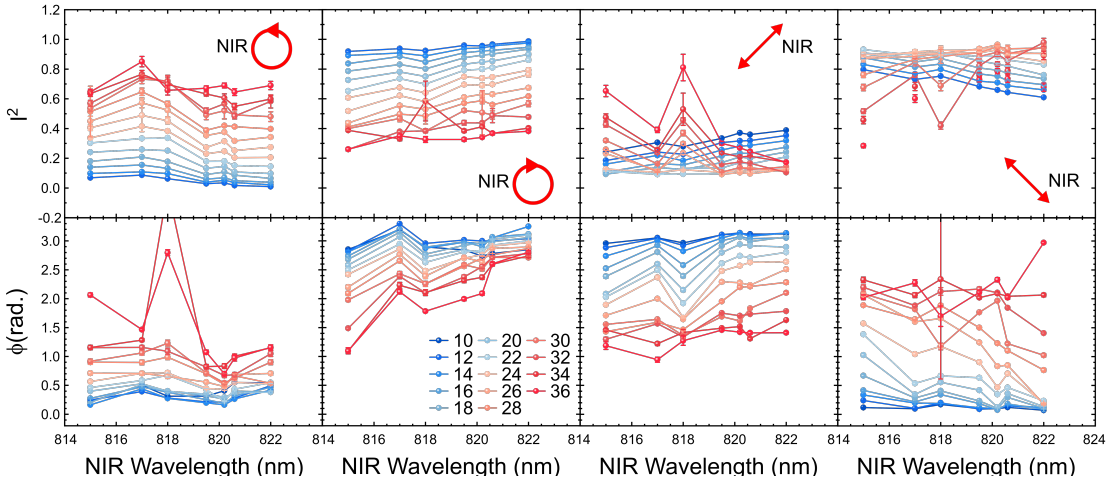

Figure 5.5 - Measurements of $\hat{\mathbf{E}}(n)$ as a Function of NIR Wavelength (Sample 1), With Varying NIR Polarization and Wavelength

Measurements of $\hat{\mathbf{E}}(n)$ as a function of NIR excitation wavelength, parameterized with $l^2(n)$ (top row) and $\phi(n)$(bottom row), from HSG experiments on Sample 1. Each column is a different NIR polarizations (RHCP: first column, LHCP: second column, Diagonal: third column, and Antidiagonal: fourth column, upper insets). The cool to warm color scale of the curves indicate shorter to longer wavelengths of NIR excitation. The specific wavelengths are defined in the legend and correspond to the absorbance spectrum in Figure 5.2 A.

There exists more nuanced quantitative behavior is visible in the curves of Figure 5.5 and 5.6. The diagonal and antidiagonal curves for $l^2(n)$ in Figure 5.4 demonstrate what appears to be a monotonic dependence on NIR wavelength. However, when looking at the behavior of other $\hat{\mathbf{E}}(n)$, it does not appear "monotonic" the best descriptor. The behavior of $\phi(n)$ in Figure 5.5 appears to be periodic with sideband order. Future experiments could prioritize probing the behavior of sideband polarization with a large NIR bandwidth, as this large scale wavelength dependence could provide greater insight to the values of the quasiparticle dephasing and band gap energy. Caution is warranted, as the classical picture used for the LIT is useful for NIR energies close to the gap, where $k_z = 0$, providing us the diagonalized Luttinger Hamiltonian in Eq. 1.6, and reducing

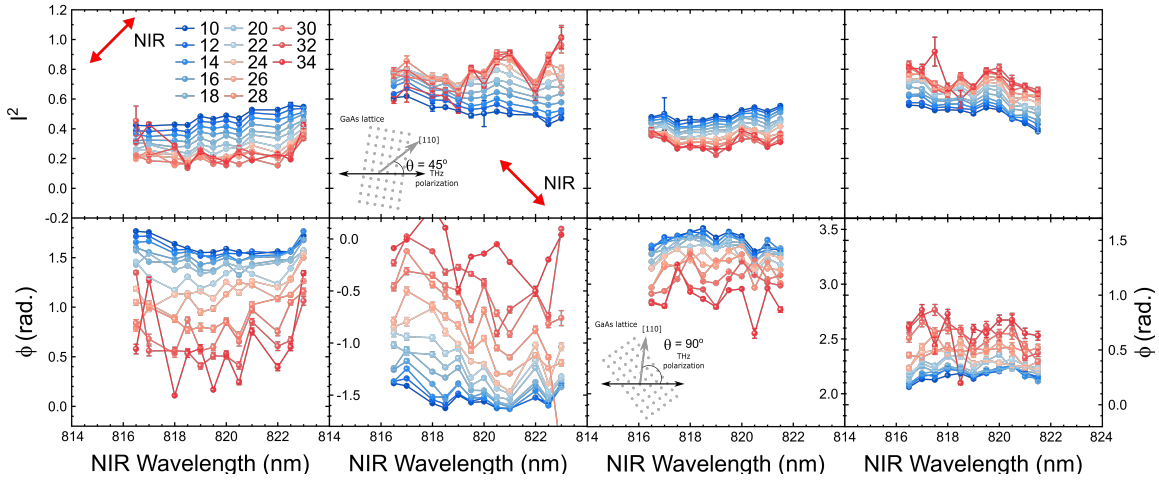

Figure 5.6 - Measurements of $\hat{\mathbf{E}}(n)$ in as a Function of NIR Wavelength (Sample 2), With Varying NIR Polarization and Wavelength, at Different Crystal Angles
Measurements of $\hat{\mathbf{E}}(n)$ as a function of NIR excitation wavelength, parameterized with $l^2(n)$ (top row) and $\phi(n)$(bottom row), from HSG experiments on Sample 2. Each column is a different NIR polarizations (Diagonal: first column, Antidiagonal: second column, Diagonal: third column, and Antidiagonal: fourth column, upper insets). The cool to warm color scale of the curves indicate shorter to longer wavelengths of NIR excitation. The first two columns are data taken with the [110] crystal axis oriented 45 degrees with respect to the THz (inset, lower second column), and the latter two columns taken with the [110] crystal axis oriented at 90 degrees (inset, lower third column). The specific wavelengths are defined in the legend and correspond to the absorbance spectrum in Figure 5.2 B.

Coulomb interaction between the quasiparticles. With the breakdown of this interpretation, experimental data will be more difficult to discern with analytical models, such as the LIT approximation.

5.2.2 Power Dependence of NIR Polarimetry

Like experiments done in the previous chapter, the measured sideband polarimetry signal should have both a NIR wavelength dependence and F_{THz} dependence. Figure 5.8 displays $\hat{\mathbf{E}}(n)$ as a function of sideband order, and Figure 5.8 displays $\hat{\mathbf{E}}(n)$ as a function of NIR wavelength. In both, each column contains data taken with different

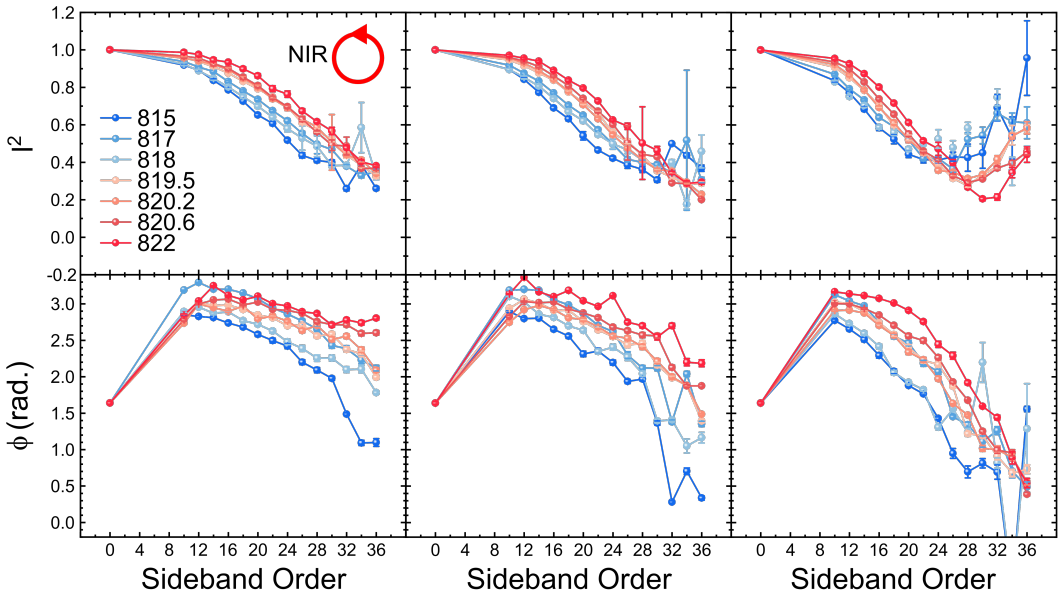

Figure 5.7 - Experimental Measurements of $\hat{\mathbf{E}}(n)$ With Varying NIR Wavelength, With Different F_{THz}.

Measurements of $\hat{\mathbf{E}}(n)$ as a function of sideband order, parameterized with $I^2(n)$ (top row) and $\phi(n)$(bottom row), from HSG experiments on Sample 1 using LHCP NIR pulses (cartoon in upper left inset) of varying wavelengths, with the cool to warm color scale indicating shorter to longer wavelengths. The specific wavelengths are defined in the legend and correspond to the absorbance spectrum in Figure 5.1 A. Each column are data taken with different F_{THz} (70 kV cm^{-1}: left, 52.5 kV cm^{-1}: middle, and 35 kV cm^{-1}: right).

F_{THz}, (70 kV/cm, left; 52.5 kV/cm, middle, 35 kV/cm, right). Figure 5.7 displays data from Sample 1 with LHCP NIR excitations, and Figure 5.8 displays data from Diagonal NIR excitations.

Because quasiparticle dephasing and their initial detuning are both present in the expression for ς_n^{ν} in Eq. 5.2, experiments in which both are separately probed are necessary to determine either value. If we assume the gap value is a constant, independent of THz field [35, 36, 89], and the quasiparticle dephasing is independent of quasiparticle momentum [29], then experiments like those presented in Figures 5.7 and 5.8 serve as fully sufficient dataset to reconstruct both parameters. Qualitatively, the data

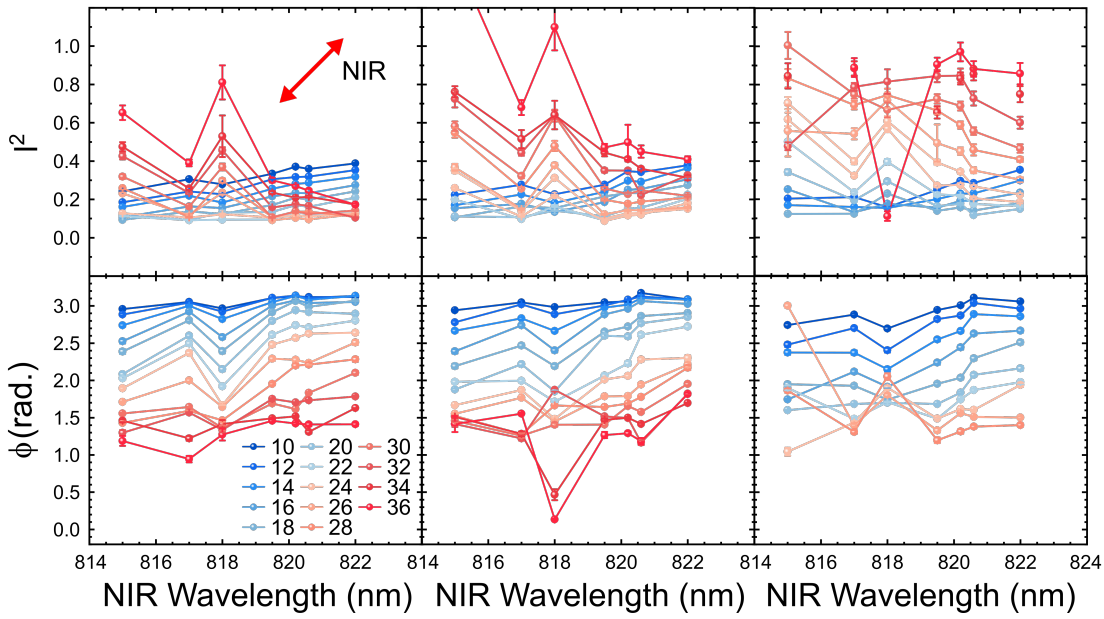

Figure 5.8 - Experimental Measurements of $\hat{\mathbf{E}}(n)$ as a Function of NIR Wavelength, With Different F_{THz}.

Measurements of $\hat{\mathbf{E}}(n)$ as a function of NIR excitation wavelength, parameterized with $l^2(n)$ (top row) and $\phi(n)$(bottom row), from HSG experiments on Sample 1 using Antidiagonal NIR pulses (cartoon in upper left inset) of varying wavelengths. The cool to warm color scale follows from lower to higher order sidebands, defined in the legend. Each column are data taken with different F_{THz} (70 kV cm^{-1}: left, 52.5 kV cm^{-1}: middle, and 35 kV cm^{-1}: right).

in Figures 5.7 and 8 demonstrate the expected behavior from the LIT model. Therefore, a cost function analysis comparing experimental sideband polarizations and those anticipated from the LIT model can be employed to determine the approximate dynamical gap and dephasing of our system.

5.2.3 Cost Function Analysis of LIT Model and Data

With datasets taken at different THz field strengths and NIR wavelengths, we can set up a cost function to be minimized. For a given dynamical gap value, E_g, and dephasing parameter, Γ_d, there are predicted sideband polarization states, parameterized by $l^2(n, E_g, \Gamma_d)$ and $\phi(n, E_g, \Gamma_d)$. The robustness of the LIT approximation is tested by

experimental data with different quasiparticle acceleration times, $\tau_{n,\nu}$, and different quasiparticle detuning, Δ_{NIR}. The former is toggled by the F_{THz} (see Eq. 4.13) and the latter is tuned by the NIR energy $\hbar\Omega$ (see Eq. 5.2). For the sideband polarizations predicted theory, the material parameters used for these calculations should be the same, taking for granted the assumptions listed in the previous section are valid for the quasiparticle energies observed experimentally. As a result, one value of the dynamical gap and quasiparticle dephasing should provide the greatest agreement. Comparing data taken at this variety of conditions leads to the cost function

$$\mathscr{C}(E_g, \Gamma_D) = \sum_n \sum_{j\in\hbar\Omega_{NIR,j}} \sum_{k\in F_{THz,k}} \left[\left(\frac{l_{j,k}^2(n, E_g, \Gamma_d) - l_{j,k}^2(n)}{l_{j,k}^2(n, E_g, \Gamma_d)} \right)^2 + \left| \frac{e^{i\phi_{j,k}(n,E_g,\Gamma_d)} - e^{i\phi_{j,k}(n)}}{e^{i\phi_{j,k}(n,E_g,\Gamma_d)}} \right|^2 \right]^{1/2} \tag{5.3}$$

When summing up this cost function across data from the 819.5, 820.2, 820.6, and 822 nm data sets from Sample 1, at all three field strengths probed, we get a cost function whose dependence on E_g and Γ_d is polluted in Figure 5.9. Here the variable plotted in the contour map is the $\mathscr{C}$ calculated at each coordinate on the x-y plane, normalized to the number of data points used at each coordinate. The color bar denotes the relative values of the $\mathscr{C}(E_g, \Gamma_d)$.

From this cost function analysis we see a clear minimum at $\Gamma_d = 4.8\hbar\omega$ and a dynamical gap of $E_g = 1.499$ eV. A plot of the calculated cost function is displayed in

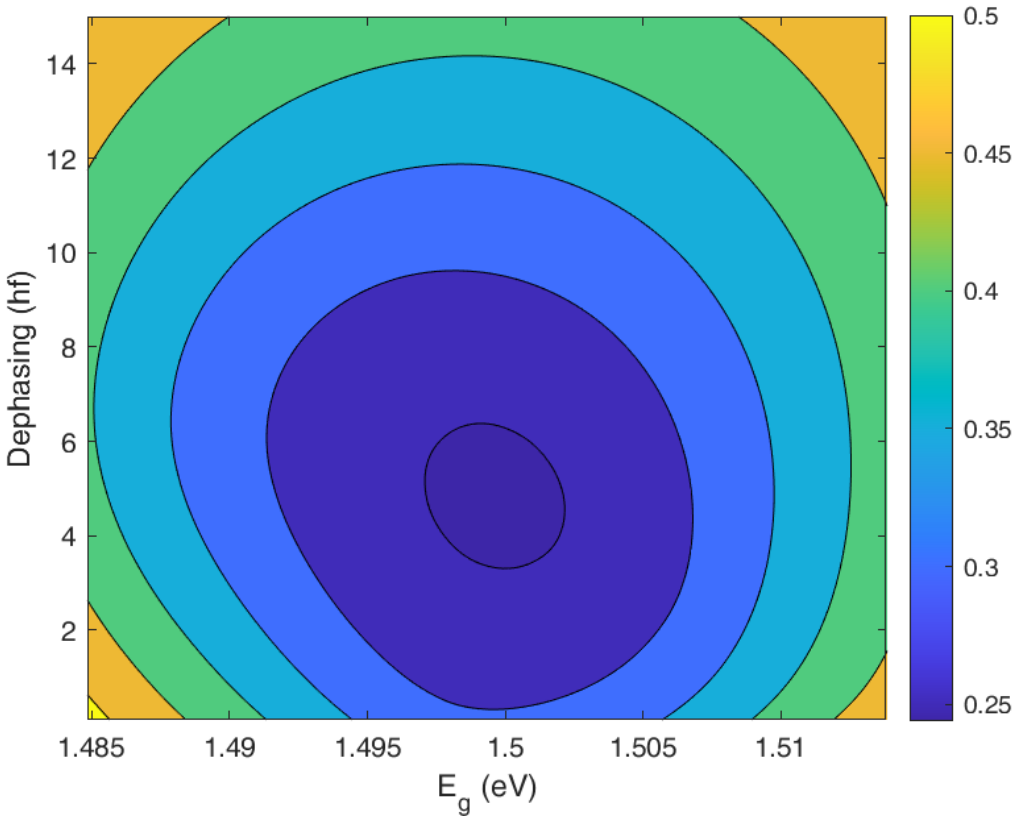

Figure 5.9 - Cost Function Analysis of LIT Calculated $\hat{\mathbf{E}}(n)$ Using Different Dephasing and Detuning Values

The difference between calculated and experimental values of $\hat{\mathbf{E}}(n)$, parameterized by the cost function $\mathscr{C}(E_g, \Gamma_d)$, displayed as a contour plot. The height of the contour at a given position is the calculated $\mathscr{C}(E_g, \Gamma_d)$ for those related coordinates. The value of a given $\mathscr{C}(E_g, \Gamma_d)$ is related by the color bar on the right.

Figure 5.9. While this dephasing value appears reasonable, and is comparable to the value used in the previous chapter which provided best agreement for the 820.6 nm data set. However, the dynamical gap value which produces a minima in all of these calculations is ~10 meV away from the quoted gap of GaAs at 0 K [44, 45]. At the time of writing, we are still in the early stages of understanding the implications of these results, and what this implies about the dynamical gap value we believe we are probing. In addition, without the incorporation of the peak splitting parameter, the shorter wavelength data sets

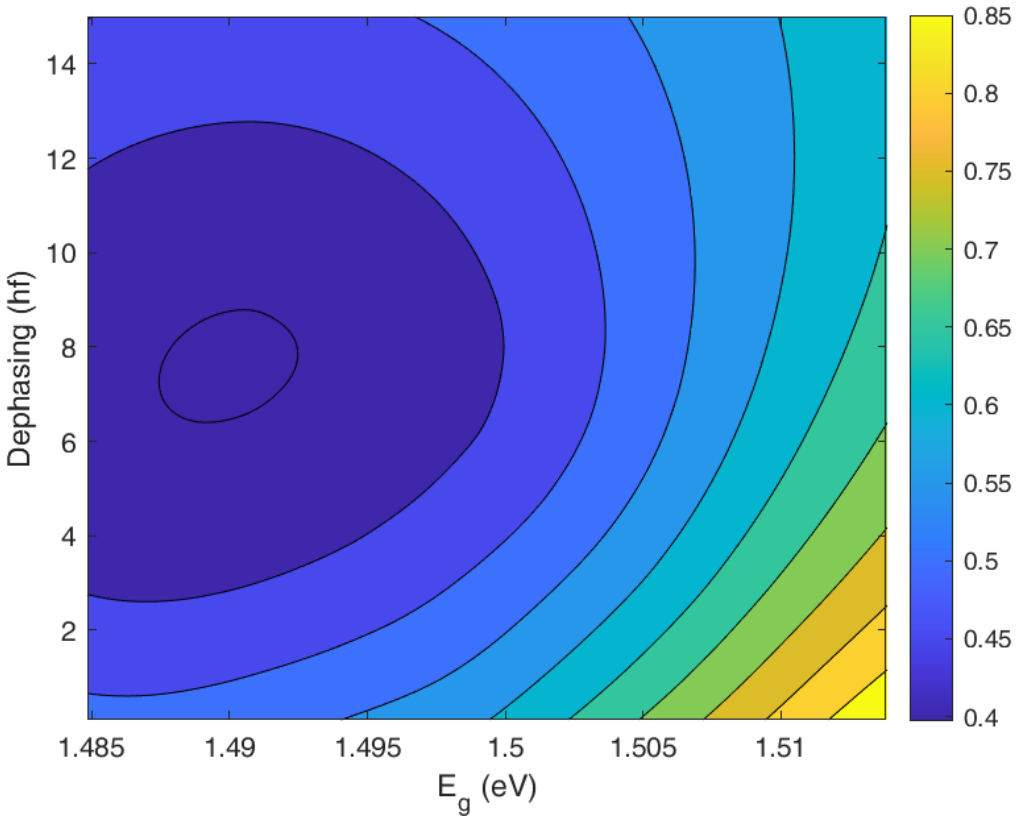

Figure 5.10 - Cost Function Analysis of LIT Calculated $\hat{\mathbf{E}}(n)$; Divergence at Shorter Wavelengths

The difference between calculated and experimental values of $\hat{\mathbf{E}}(n)$, parameterized by the cost function $\mathscr{C}(E_g, \Gamma_d)$, displayed as a contour plot. Here the data is from the 815 nm excitation wavelength on Sample 1. Notice the higher overall cost and the 10 meV redshift from the minima from the longer wavelength data sets.

not included in the cost analysis are not well behaved with respect to the longer wavelength data. Figure 5.10 shows the cost function analysis for the 815 data set, which has an additional ~10 meV redshift from the calculated dynamical gap. At this early state of analysis, there is no clear reason as to why data taken below 819.5 nm diverges from the data taken above this threshold.

Finally, the incorporation of a peak splitting parameter δ_ν provides a lower cost function, better agreement among all the data sets, and a more realistic value for the

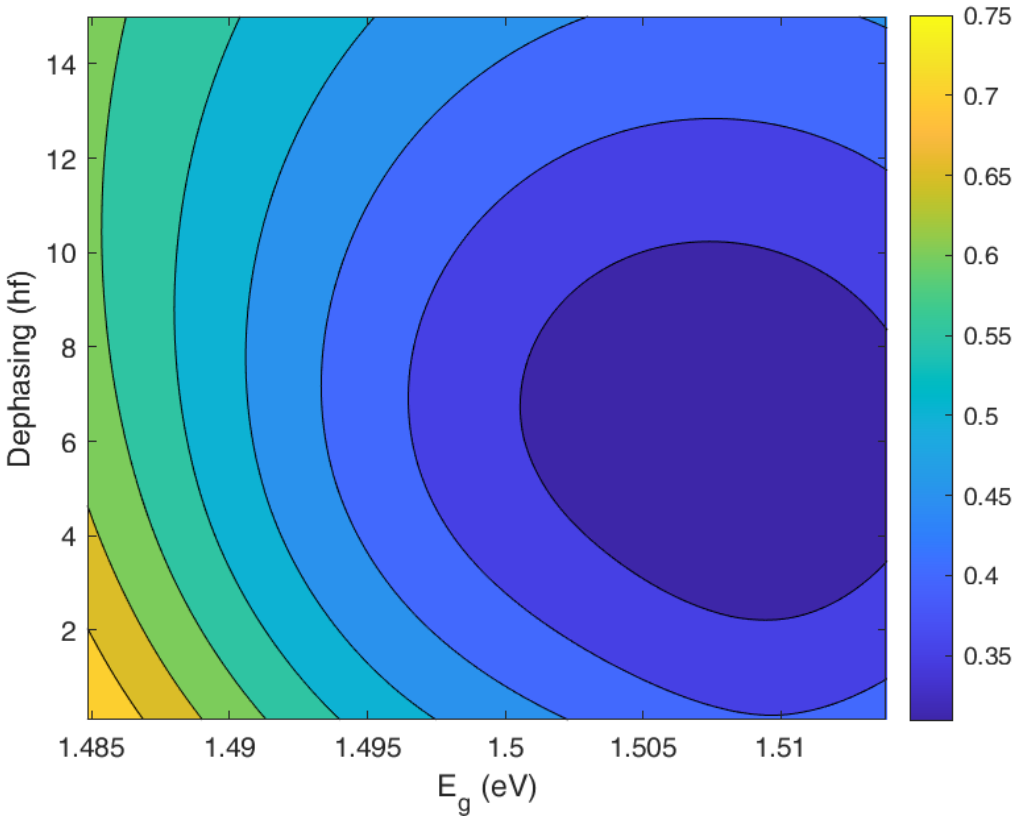

Figure 5.11 - Cost Function Analysis of LIT Calculated $\hat{\mathbf{E}}(n)$; Incorporating Peak Splitting Parameter

The difference between calculated and experimental values of $\hat{\mathbf{E}}(n)$, parameterized by the cost function $\mathscr{C}(E_g, \Gamma_d)$, displayed as a contour plot. Here the data is from all seven NIR excitation wavelengths and three F_{THz} from Sample 1. For the LIT approximation, a peak splitting parameter of $\delta_\nu = 1.5$ meV was used.

dynamical gap. As will be elaborated in a following section, this makes analysis of the detuning term more difficult, but also is an argument for how sensitive HSG is on the effective Hamiltonian of a system. With a peak splitting term of 1.5 meV, on the order of the observed exciton peak splitting in Figure 5.2, we observe a cost function minimum with $\Gamma_d = 4.8\hbar\omega$ and $E_g = 1.511$. This dynamical gap value is close to the expected gap of bulk GaAs at 25 K, and is close to the exciton peak line in the absorbance spectrum in the upper panel of Figure 5.2.

Figure 5.11 shows the cost analysis, incorporating all seven NIR wavelength datasets. Incorporating a 1.5 meV peak splitting parameter into the LIT calculation, the cost analysis yields a minimum at the values $\Gamma_d = 6.3\hbar\omega$ and $E_g = 1.508$ eV, in much better agreement with the longer wavelength data set cost analysis. All indications are a continuation of this line of inquiry will also yield a value for δ_ν, incorporating the parameter as a third variable to minimize the cost function.

5.2.4 Differences Between the Two Samples

Looking at Figures 5.3 and 5.4, we can see differences between the changes in sideband polarization as a function of Ω between the two samples. Looking at the effects of dephasing and effective mass on the outgoing sideband polarization, it would appear the two samples have observably different dephasing rates. In part, this could be due to the different temperatures at which experiments were conducted for Samples 1 and 2. However, there could also be observably more quasiparticle dephasing in one crystal compared to the other. If this can be quantitatively measured and verified, then in the future these NIR and F_{THz} sweeps of sideband polarimetry scans could, among other outcomes, nondestructively determine the amount of quasiparticle dephasing in a bulk semiconductor. In quantum materials proposed to be a part of the next generation of quantum hardware, such a method would be valuable in determining the coherence and longevity of qubits.

5.3 USE FOR QUANTUM MATERIALS

In the field of topological condensed matter, key Hamiltonian parameters like the dynamical gap are relevant for defining phase spaces [90]. Recent works have theorized methods to leverage these non-trivial topologies as sources of incorruptible quantum information for long lived quantum computing bits, or qubits [90]. For the constituent components of a topological quantum computer to operate optimally, the system must be precisely tuned to the topological phase, which requires knowledge of the Hamiltonian parameters which determine the phase [91, 92]. To date, there is no non-destructive, phase sensitive characterization technique for these materials, making the fabrication of a reliable topological quantum computer exceedingly difficult.

5.3.1 Spin-Orbit-Coupled Semiconductors Used in MZM Systems

HSG polarimetry holds promise for resolving the spin orbit coupling (SOC) induced splitting of bands associated with different p-orbitals in semiconducting systems. Semiconducting systems with large SOC in the highest energy valance bands have become materials of great interest in the materials science community [90, 93, 94]. When hybridized with a low temperature superconductor, the overall system is theorized to host Majorana fermions, incorruptible sources of quantum information with tunable phases [90, 95]. Among other proposed quantum bits, or q-bits, Majorana fermions are one of the few topologically protected q-bits [90]. While other qubits have already been built [96], and deployed in quantum computers [97], Majorana fermions and their zero-bias modes (MZM) have not been observed and reported by scientists.

The novel materials used as the high SOC semiconductor in these heterostructures are major bottlenecks in the process of building a reliable MZM system. Specifically, most of the materials used are relatively new to the field of material science, and their SOC parameters are not well known. The environment which tunes our heterostructure into a MZM is highly calibrated, determined by the energy scale of the SOC. We believe HSG could serve as a non-destructive, bulk sensitive method to measure the SOC parameter in semiconductors.

The importance of the peak splitting parameter to model the quasiparticle dynamics provides great promise for future experimentation of more novel quantum materials. The Luttinger Hamiltonian already incorporates SOC in its perturbative form, however, a degeneracy exists for the two highest energy valence bands. Non-trivial strain removes this degeneracy, creating a difference in quasiparticle energy and thus detuning parameter. For bulk GaAs with a small strain, this difference in small. Therefore, the sensitivity bodes well for using NIR dependent HSG on high-SOC semiconductors theorized to be a part of MZM die.

5.3.2 NIR Tuning Hole Basis Analysis

Given the sub-meV sensitivity of HSG between the quasiparticle initial energy and the outgoing sideband polarization, it might seem reasonable to expect behaviors like the hole species population, parameterized by $|\varsigma_n^{\nu}|$ to also show sensitivities to the NIR excitation energy. If the absorbance plots from our samples is any indicator of the NIR wavelength dependence of hh and lh populations, one would expect a narrowly defined excitation near the band gap to produce significantly more of one hole state over the

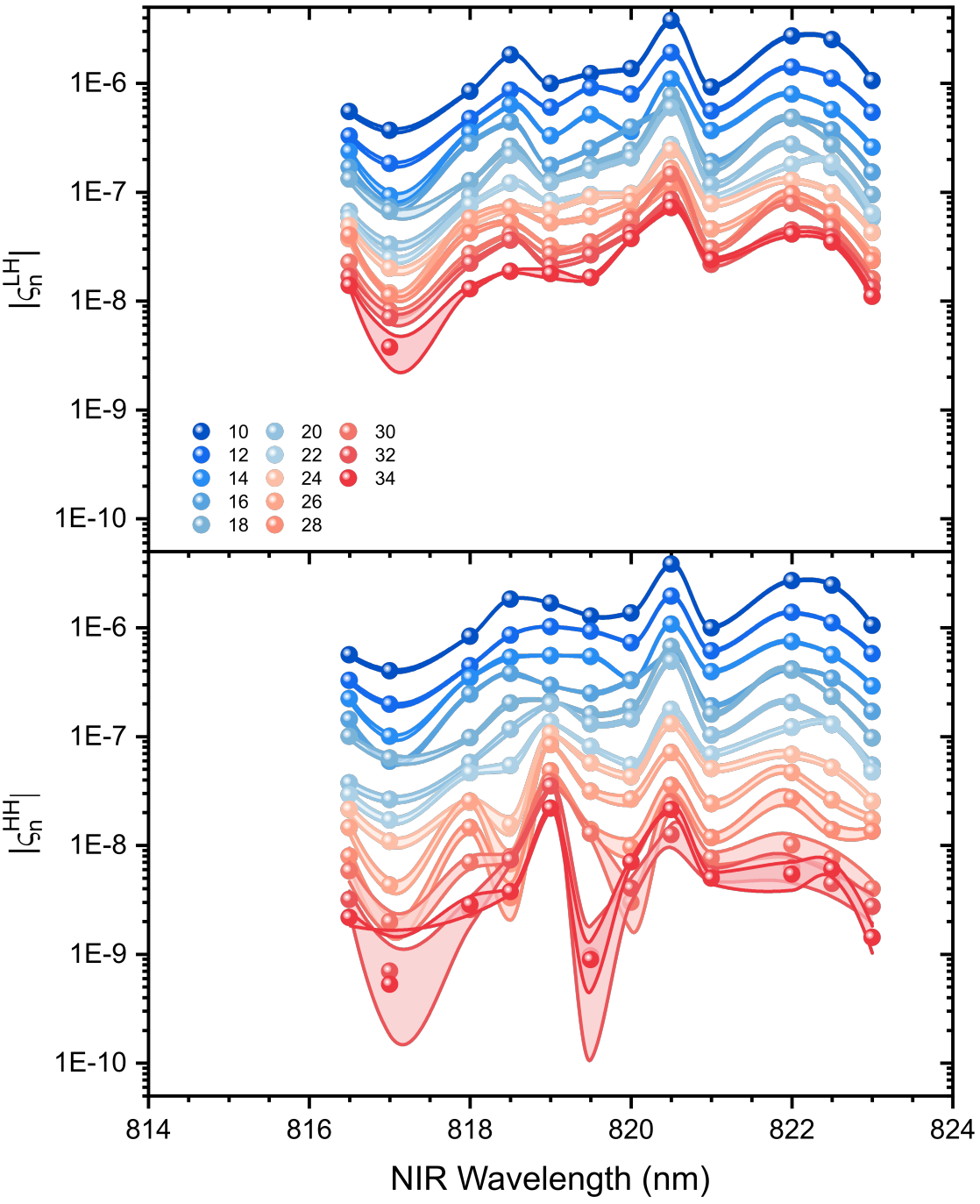

Figure 5.12 - Hole Propagator Magnitude Dependence on NIR.
The reconstructed $|\varsigma_n^{\nu}|$ as a function of NIR wavelength for Sample 2 at $\theta_{[110]} = 45$ degrees. Each colored band being different SB orders, indicated in the legend and following the color scheme of Figure 5.5.

other.

Data presented in this chapter demonstrates a lack of an overpopulation of one hole species through a selective excitation process. When the two hole states are adiabatically driven by the THz field, there is a theorized process of an absorbance spectra flattening in energy space, related to a phenomena called dynamical Fano resonance [98, 99]. This would not be the first demonstration of the large Terahertz field distorting the band structure of semiconducting systems [69, 100]. Future experiments have been proposed to observe or negate such a flattening of the optical response of our semiconductor. Should there be such a flattened response, this could perhaps explain the lack of an overpopulated band with the correct NIR resonant excitation, and the appearance of some blue and redshifted values for our fit sideband polarization signals.

Such a behavior appears to exists in our experimental data. Figure 5.12 displays the observed $|\varsigma_n^{\nu}|$ as a function of NIR wavelength, corresponding to data taken from the polarimetry scans from Figure 5.4. There is no clear wavelength in which one state is significantly more populated than the other. From everything we are seeing, something more than absorbance is occurring in our system.

Previous works have put forward the idea of strong electric fields adiabatically stabilizing excitonic wavefunctions [99]. Under such conditions, the density of states for the quasiparticles will spread out, akin to the absorbance lines in the material broadening. Such a phenomena is called Dynamical Fano Resonance [98]. While preliminary efforts have been proposed to observe such a phenomenon, to the best of our knowledge, no group, including our own, has observed such a phenomena in bulk GaAs. However,

behavior like that of the $|\varsigma_n^{\nu}|$ in Figure 5.12 provides further evidence such a phenomena exists.

5.3.3 Peak Splitting Parameter

Along with the increased quantitative agreement between experiment and theory, our data also demonstrates a qualitative behavior related to a non-zero value of the peak splitting. Figure 5.13 shows data taken at different field strengths, scaled with the $n \cdot \lambda^{-2/5}$ dependence predicted by the LIT approximation. If $\Delta_{NIR} = 0$, this scaling relationship should work in the limit of the approximation. However, if $\Delta_{NIR} \neq 0$, there is an additional $n \cdot \lambda^{-2}$ term present in expressions in Eq. 4.13. If $\delta_{\nu} = 0$, then tuning the NIR to the dynamical gap will make $\Delta_{NIR} = 0$ for both hole species, and $n \cdot \lambda^{-2/5}$ should generate the best overlap between data sets taken at different field strengths. If $\delta_{\nu} \neq 0$, then no NIR wavelength will result in zero detuning for *both* e-h species, as the splitting parameter creates a different dynamical gap for the two.

Figure 5.13 appears to demonstrate conditions where $\delta_{\nu} \neq 0$, as none of the NIR wavelengths used in experiment have field dependent data sets which collapse well with $n \cdot \lambda^{-2/5}$ scaling predicted by the LIT approximation. Each column is a data set taken at a different NIR wavelength, with the different colored curves representing data taken with different F_{THz} (F_{THz} = 70 kV/cm, green; F_{THz} = 52.5 kV/cm, blue, F_{THz} = 35 kV/cm, red). The top row displays the measured $l^2(n)$ values of the sideband electric field, and the bottom row displays $\phi(n)$. All the data were taken with Diagonally polarized NIR excitation pulses. No data set seems to demonstrate a clear overlap, despite the wide range of wavelengths tuned. In addition, there is no monotonic behavior which would

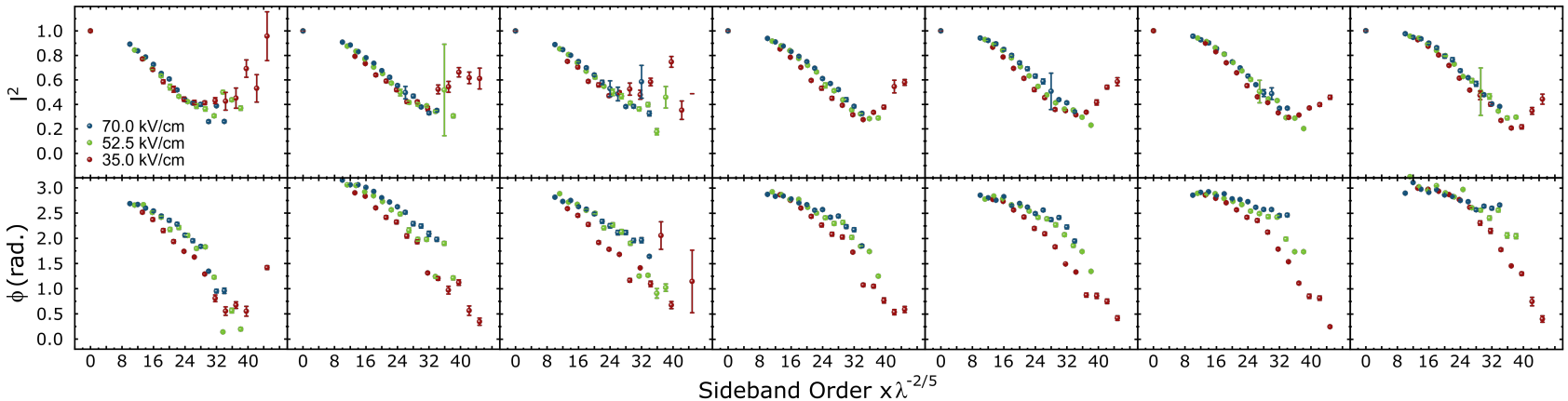

Figure 5.13 - Scaled Datasets at With Different NIR Excitations

Measurements of $\hat{\mathbf{E}}(n)$ as a function of sideband order, parameterized with $l^2(n)$ (top row) and $\phi(n)$(bottom row), from HSG experiments on Sample 1. For each of the curves, the NIR is LHCP polarized. The different colored curves are data taken at different F_{THz} (F_{THz} = 70 kV/cm, green; F_{THz} = 52.5 kV/cm, blue, F_{THz} = 35 kV/cm, red), scaled by the $n \cdot \lambda^{-2/5}$ factor predicted by the LIT when $\Delta_{NIR} = 0$. Each column contains data from experiments utilizing different NIR wavelengths (815 nm: first column, 817: second, 818: third, 819.5: fourth, 820.2: fifth, 820.6: sixth, 822: seventh).

indicate a direction to tune the NIR excitation which would eventually result in a $\Delta_{NIR} \neq 0$ condition. This qualitative analysis agrees with the preliminary quantitative analysis, detailed in section 5.3.3.

While this lack of overlap for all probed datasets makes the determination of Δ_{NIR} more difficult, this result is an encouraging reminder of the sensitivities of HSG polarimetry to perturbations from the Luttinger Hamiltonian on the meV scale. Future HSG experiments conducted on high SOC semiconductors will benefit from such precise measurements of the difference in dynamical gap between quasiparticles. For such materials, proposed to be a part of topological quantum computers [91, 92, 101], such precision will allow for the proper tuning of the Fermi energy into the topological phase of the heterostructure.

Chapter 6 — HaRφως: Hamiltonian Reconstruction through the Polarimetry of High Order Sidebands

By connecting a seemingly immeasurable quantum phase to a clearly measurable optical phase, there were many new avenues of experimentation. Reconstructing the effective Hamiltonians of quasiparticles was one of the more exciting and extensive novel lines of inquiry. The operators governing the behavior of our quasiparticles contain both real and imaginary components, making their measurement fundamentally impossible in most experiments sensitive to quantum mechanics. But they also govern the trajectories our quasiparticles take when being accelerated by the THz and the phases they accumulate

along the way. Developing a model of the Hamiltonian's influence on sideband polarization was an involved process. Developing an *analytical* model of this influence with experimentally extractable values of the effective Hamiltonian parameters would prove much more difficult than initially expected.

The one set of material parameters we have taken for granted in our analysis, so far, are the Luttinger parameters of bulk GaAs. For a well characterized material so thoroughly integrated in modern technology, this is not too dangerous of an assumption. One of the main goals of this experiment was not to discover some radically different values for the Luttinger parameters, but rather confirm the existing values using a new method which could be expanded to almost any system with a band gap. By demonstrating the reliability of the result on a reliable material, we hoped to extend the method to more exotic systems theorized to form the next generation of quantum electronics.

With that being said, there can be improvements in the current values. Most of the literature quotes the values of the Luttinger Hamiltonian without error bar [45], and rely of goodness-of-fit calculations to cyclotron resonance, where there are more variables than functions to fit. Surely the field of materials characterization should do better for the next generation of devices requiring a deeper understanding of the quantum nature of the quasiparticles present in the system at hand.

6.1 REDUCED MASS AS PROBE FOR LUTTINGER PARAMETERS

Going back to the expression for ς_n^{ν} in its most general form, conveyed in Eq. 3.12,

$$\varsigma_n^{\nu} = \sum_{s=\pm} \frac{i\omega d^2}{2\pi V\hbar} \int_0^{2\pi/\omega} e^{i(\Omega + n\omega)t} \int_{-\infty}^{t} dt' e^{iA_{\nu}(t,t')} e^{-i\Omega t'} \tag{6.1}$$

Even in this most general expression, we can argue there is a dependence on the angle between the THz electric field and the [110] crystal direction, labeled θ. Because this expression for the propagator, and all subsequent simplifications, is dependent on the dynamical phase of the quasiparticles, there is a dependence on the reduced mass of the quasiparticle pair. Going back to the initial expression for the dynamical phase

$$A_{\nu}(t,t') = \int_t^{t'} dt'' \left[E_c\left(\mathbf{k}(t)\right) - E_{\nu}\left(\mathbf{k}(t)\right) + i\Gamma_d \right] / \hbar \tag{6.2}$$

There is a clear dependence on the direction in *k*-space taken by the quasiparticles in the energy terms included in this expression.

Using the expressions for the dispersion relations of the conduction, heavy hole, and light hole band in bulk GaAs, this dynamical phase term can be put in terms of the reduced mass of the quasiparticle pair

$$A_{\nu}(t,t') = \int_t^{t'} dt'' \left[\hbar^2 k^2(t)(2\mu)^{-1} + i\Gamma_d \right] / \hbar \tag{6.3}$$

This reduced mass parameter, μ, is dependent on the specific path taken by the quasiparticle pairs, and the effective Hamiltonian which determines the dispersion relation near the band edge.

6.1.1 the Luttinger Parameters

In order to express the dispersion relations from the integral in Eq. 6.2 to the free-particle form in Eq. 6.3, the reduced mass term takes the form

$$\mu_{hh}(\theta) = m_0 \left(m_c^{-1} + 2\gamma_1 - \gamma_2 |\, \mathbf{n}(\theta) \,| \right)^{-1} \tag{6.4}$$

for the e-hh pair, where m_0 is the free electron mass, m_c is the conduction band effective mass for bulk GaAs, 0.067 m_0 [44], γ_1 & γ_2 are two of the Luttinger parameters, and $\mathbf{n}(\theta)$ is the spinor-like component used to express the block diagonal, $k_z = 0$ Luttinger Hamiltonian, taking the form

$$\mathbf{n}(\theta) = \left[\frac{\sqrt{3}}{2} \sin(2\theta), \frac{\sqrt{3}\gamma_3}{2\gamma_2} \cos(2\theta), -\frac{1}{2} \right] \tag{6.5}$$

With this form of $\mathbf{n}(\theta)$, we can say the reduced mass, and, as a result, the propagator ς_n^{ν} are all dependent on the THz-to-crystal angle θ, and the three values of the Luttinger parameters.

6.1.2 Propagators Differing With Hole Species

Looking at the form of the propagator we used in Chapter 4

$$\varsigma_n^{\nu} = \frac{i\omega d^2}{2\pi V \hbar} \exp\left[i\sqrt{3} \left(\frac{8}{15} n + (i\Gamma_d + \Delta_{NIR})(\hbar\omega)^{-1} \right) (2n E_{\gamma THz}/U_{p,\nu})^{1/4} \right] \tag{6.6}$$

there are a few variables which bring about differences in the relative phases and magnitudes of the hh and lh propagators. In the last chapter, we saw NIR dependent data which indicated the existence of splitting between the band edges of the hh and lh states. This would result in different detuning values for each hole species, $\Delta_{NIR,\nu}$, which manifests as different phases for the two propagators and contributes to the interference phenomena reported throughout this thesis. In addition to the splitting parameter, the ponderomotive energy factor in Eq. 6.6,

$$U_{p\nu} = \frac{e^2 F_{THz}^2}{4\omega^2 \mu_\nu} \tag{6.7}$$

will be different because the reduced masses for the e-hh and e-lh pairs take the form

$$\begin{aligned} \mu_{hh}(\theta) &= m_0 \left(m_c^{-1} + 2\gamma_1 - \gamma_2 |\,\mathbf{n}(\theta)\,| \right)^{-1} \\ \mu_{lh}(\theta) &= m_0 \left(m_c^{-1} + 2\gamma_1 + \gamma_2 |\,\mathbf{n}(\theta)\,| \right)^{-1} \end{aligned} \tag{6.8}$$

The addition versus the subtraction of the $\gamma_2 |\,\mathbf{n}(\theta)\,|$ term between the two hole species is enough for a lifting of a degeneracy of the hh and lh eigenstates away from the Γ point of the Brillouin zone, and enough for the observed Bloch-wave interferometry reported in Chapter 4.

In that chapter we tuned the ponderomotive energy of our quasiparticles, and thus the relative phase between the propagators, by tuning the F_{THz} value. Figure 4.4 demonstrates this toggling of field strength alters the sideband polarization, or interference signal. In this chapter, we modify the phases between the ς_n^ν by modifying the reduced mass term in the ponderomotive energy expression, which is accomplished by turning the direction in the Brillouin zone traversed by the quasiparticles, parameterized by θ.

6.1.3 Probing the Contribution of Luttinger Parameters To Sideband Signal

Given the dependence of ς_n^ν on θ, and how the Luttinger parameters modulate this change through the reduced mass term, HSG polarimetry at different crystal angles serves as a probe to the effective Hamiltonian parameters of the quasiparticles. This change as a function of angle should mirror the symmetry of the GaAs crystal, which, along with the

Luttinger Hamiltonian, has C_4 symmetry. Observing this symmetry and connecting the dependence of ς_n^ν to θ by the LIT model or some higher order expression for the propagator provides the opportunity for an isotropic, all optical probe of the effective Hamiltonian partakers of the quasiparticles driven far from equilibrium.

6.2 ANGLE DEPENDENT HSG POLARIMETRY

Polarimetry experiments which tune the crystal angle is difficult in the currently existing electro-optical setup. To acquire HSG polarimetry data at different crystal orientations, the sample has to be warmed up and macroscopically rotated, brought back to vacuum, and cooled to the same operating temperature. This takes on the order of ~5 hours, making each unique set of angular data a time consuming matter. All of this is to highlight the difficulty of running a controlled experiment, where the only difference run-to-run is the THz-to-crystal orientation. Even the data presented in Chapter 2 and [63] were not as longitudinal as the experiments of this chapter, as for that chapter each experimental run could be treated as an independent dataset. For the line of analysis proposed in this chapter to be effective, experiments need to be consistent among all data sets acquired.

In Eq. 6.4, the γ_1 Luttinger parameter has no angular dependence. Therefore, this variable cannot be reconstructed through angle modulation alone. Instead, the behavior of ς_n^ν as a function of sideband order must be used. Looking back at Chapter 4, we see the dephasing rate also plays an important role in the sideband polarization, and thus our measured ς_n^ν as a function of sideband order. As a result, in addition to angular dependent

HSG polarimetry, some F_{THz} dependent measurements were conducted to determine the role of dephasing in our signal.

Comparing a ratio of the two propagators will divide away the pre-factors in Eq. 6.1, which are the same for both the hh and lh. Because the dynamical phase and thus the Luttinger parameter contribution is in the complex exponential of the propagator, looking at the argument of the ratio will provide the most insight into the dependence on $\gamma_1, \gamma_2, \& \gamma_3$.

6.2.1 Angle Dependent Data With Broken C_4 Symmetry

Figure 6.1 displays experimental data taken at 13 different θ, displayed as discrete dots on the x-axis, using polarimetry data from the 10th (red) to 32nd (purple) order sideband. The values of $\mathrm{Arg}(\varsigma_n^{hh}/\varsigma_n^{lh})$ are reconstructed using data from four polarimetry scans at each angle, and measurements of the $|J_{xx,n}|$ parameter using the PMT calibration measurement detailed in section 3.2. The bands connecting the discrete datasets are B-Splines.

To begin, these data clearly vary with θ. For a given sideband order presented in Figure 6.1, there is a variance of 30 degrees between datasets taken at different angles. However, the data demonstrate a broken C_4 symmetry. If there were such a symmetry in the $\mathrm{Arg}(\varsigma_n^{hh}/\varsigma_n^{lh})$, then data sets close to $\theta_{[110]} = \pm 45^o$ would be equivalent. This is not the case, and instead the data demonstrates the C_2 of the THz field. Such symmetry breaking in the GaAs crystal probably occurred through anisotropic strain from the vdW bonding process. If this were the case, perturbed Hamiltonians incorporating these

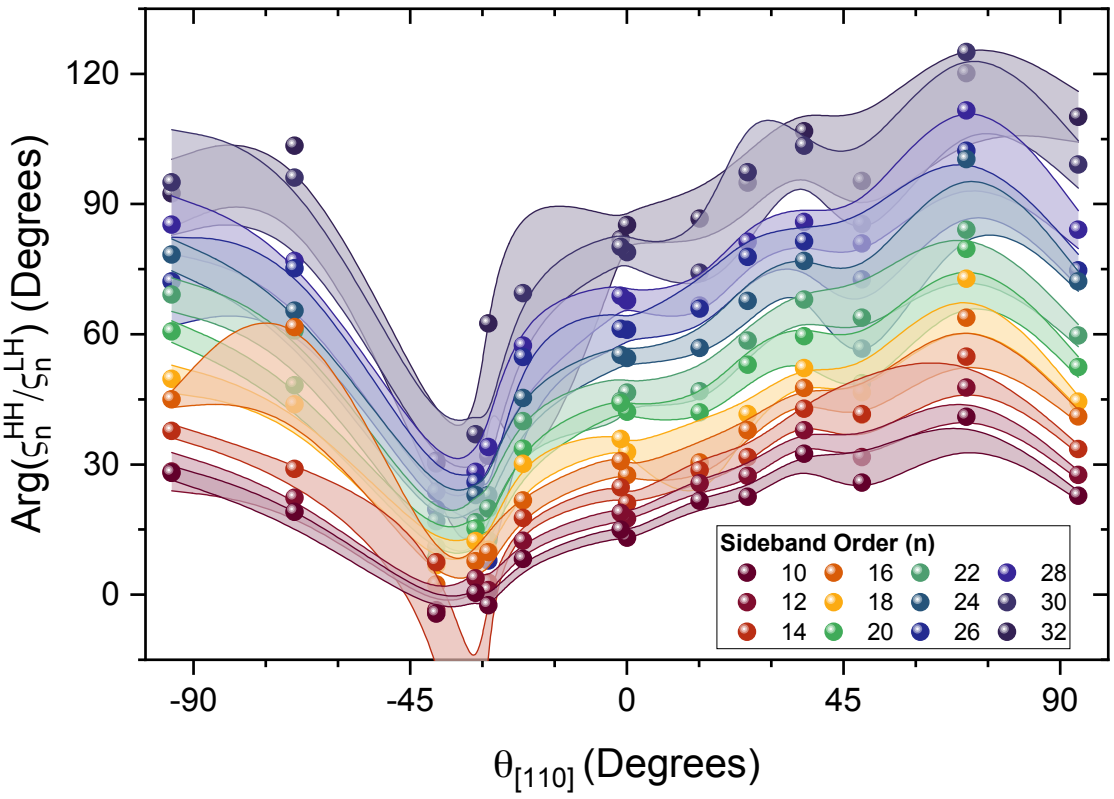

Figure 6.1 - Argument of Ratio of Propagators as a Function of THz-To-Crystal Angle Orientation
Measurements of Arg($\varsigma_n^{hh}/\varsigma_n^{lh}$) at sampled crystal orientations, θ, defined by the THz-to-[110] crystal axes orientation. Each color is a different sideband order, defined in the legend with red indicating the lowest order and purple indicating the highest order. The bands connecting the data are B-Splines.

distortions to the GaAs crystal and band structure are required in order to bring about better agreement between experiment an theory.

Figure 6.2 displays the magnitude of the ratio of these two propagators, $\left|(\varsigma_n^{hh}/\varsigma_n^{lh})\right|$, which gives information about the relative population differences at different sideband orders and trajectories along the crystal axes. The plotting conventions are the same as in Figure 6.2. A value of one indicates an equal population of hh and lh species producing a sideband of order *n*, a value greater than one indicates more hh than

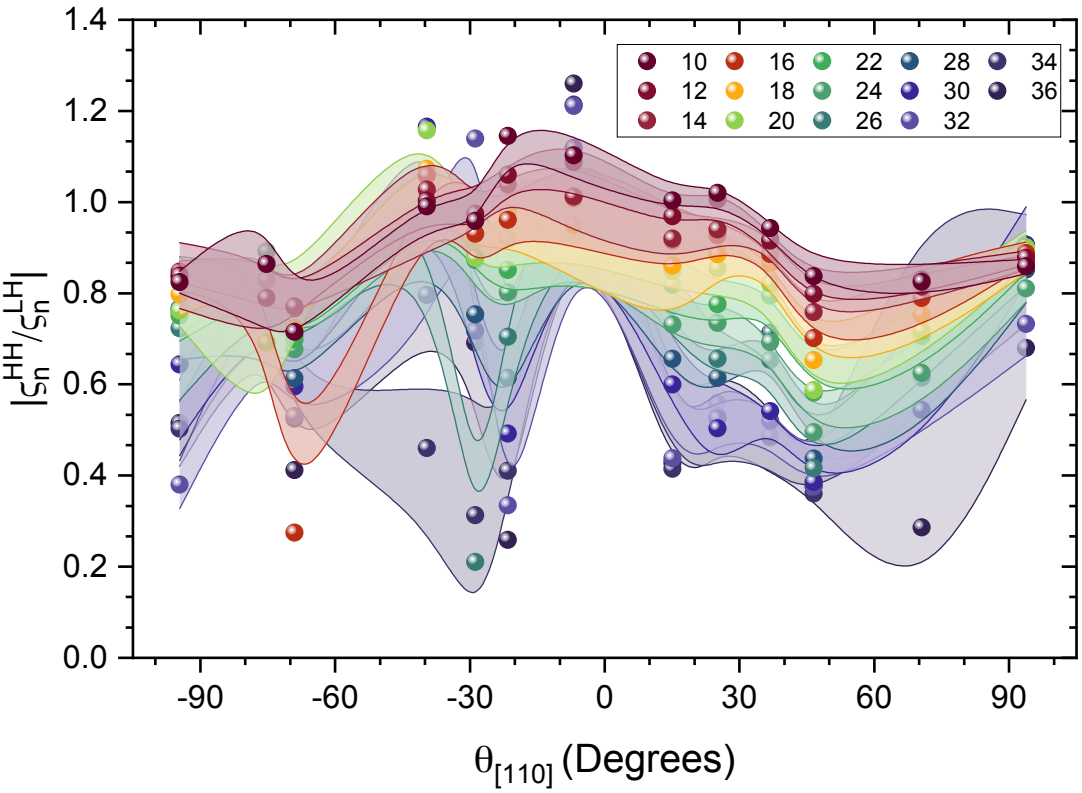

Figure 6.2 - Magnitude of Ratio of Propagators as a Function of THz-To-Crystal Angle Orientation

Measurements of $\left|(\varsigma_n^{hh}/\varsigma_n^{lh})\right|$ at sampled crystal orientations, θ, defined by the THz-to-[110] crystal axes orientation. Each color is a different sideband order, defined in the legend with red indicating the lowest order and purple indicating the highest order. The bands connecting the data are B-Splines. On this plot a value of one indicates an equal population of hh and lh species producing a sideband of order *n*, a value greater than one indicates more hh than lh pairs, and a value less than one indicates more lh than hh pairs.

lh pairs, and a value less than one indicates more lh than hh pairs. Due the difference in reduced mass of the e-hh and e-lh pairs, there should be more e-lh pairs at higher sideband orders. The acceleration time by the THz field, $\tau_{n,\nu}$ from Eq. 4.9, will be shorter for the e-lh pairs, meaning processes like dephasing will have less of an effect on these states. This would be analogous to the value of $\left|(\varsigma_n^{hh}/\varsigma_n^{lh})\right|$ going from 1 to 0 as a

function of sideband order, which is demonstrated for all angles probed in experiment. Also, because we are looking at the magnitude and not the angle between these two complex values, we should expect a phase shift between the the $\left|(\varsigma_n^{hh}/\varsigma_n^{lh})\right|$ and $\mathrm{Arg}(\varsigma_n^{hh}/\varsigma_n^{lh})$ data set. In Figure 6.2 the $\left|(\varsigma_n^{hh}/\varsigma_n^{lh})\right|$ data (especially the lower order sidebands) oscillating with C_2 symmetry with respect to the GaAs crystal axis, like the data in Figure 6.1, but with a 45 degree phase shift, which is the expected shift.

While both of these data sets demonstrate a dependence on crystal angle, they demonstrate a reduced symmetry (C_2) when compared to the GaAs crystal (C_4).

6.2.2 THz Field Measurements of Quasimomentum Dependent Dephasing

In an effort to make sense of the change in sideband polarization as a function of sideband index, we developed a method to compare HSG polarimetry data taken at two or more field strengths to build an effective model of the dephasing of the quasiparticles. By applying this method to each order, we are in effect reconstructing a quasi momentum dependent model for the dephasing.

First, a third order approximation of the THz field was developed to produce a form of the semiclassical version of ς_n^{ν}, dependent on a value for the reduced mass and dephasing rate, taking the form

$$\varsigma_n^{\nu} \propto \frac{1}{\sqrt{|\,q_{0,n}(\Gamma_d)\,|}} \exp\left[i\left(-\frac{n\pi}{2} + q_{1/4,n}(\Gamma_d)\left(\frac{\hbar\omega}{U_{p,\nu}(\mu)}\right)^{1/4} + q_{3/4,n}(\Gamma_d)\left(\frac{\hbar\omega}{U_{p,\nu}(\mu)}\right)^{3/4} \right) \right] \tag{6.9}$$

Here the quantum correction

$$q_0(\Gamma_d) = (a_n(\Gamma_d) - c_n(\Gamma_d)^5(a_n(\Gamma_d) + c_n(\Gamma_d))^2/24 - (a_N(\Gamma_d) - c_N(\Gamma_d))^7/216 \quad (6.10)$$

Where the coefficients

$$\begin{aligned} a_n(\Gamma_d) &= -18^{1/4}\frac{\sqrt{i\Gamma_d/(\hbar\omega)} - 2\sqrt{n + i\Gamma_d/(\hbar\omega)}}{3\sqrt{-\sqrt{i\Gamma_d/(\hbar\omega)} + \sqrt{n + i\Gamma_d/(\hbar\omega)}}} \\ a_n(\Gamma_d) - c_n(\Gamma_d) &= 18^{1/4}\sqrt{-\sqrt{i\Gamma_d/(\hbar\omega)} + \sqrt{n + i\Gamma_d/(\hbar\omega)}} \\ a_n(\Gamma_d) + c_n(\Gamma_d) &= 18^{1/4}\frac{\sqrt{i\Gamma_d/(\hbar\omega)} + \sqrt{n + i\Gamma_d/(\hbar\omega)}}{3\sqrt{-\sqrt{i\Gamma_d/(\hbar\omega)} + \sqrt{n + i\Gamma_d/(\hbar\omega)}}} \end{aligned} \quad (6.11)$$

The coefficient to the LIT approximation expression

$$\begin{aligned} &q_{1/4,n}(\Gamma_D) \\ &= n\,a_n(\Gamma_D) + i\frac{\Gamma_d}{\hbar\omega}(a_n(\Gamma_d) - c_n(\Gamma_d)) - (a_n(\Gamma_d) - c_n(\Gamma_d))^5/360 \\ &-(a_n(\Gamma_d) - c_n(\Gamma_d))^3(a_n(\Gamma_d) + a_n(\Gamma_d))^2/24 \end{aligned} \quad (6.12)$$

The third order expansion term $q_{3/4,n}(\Gamma_d)$ is even more involved. Because the derivation and use of these coefficients are not germaine to the scope of this thesis, they will not be presented. A more involved derivation and discussion is already present in the literature [29]. The inclusion of lower order coefficients is included to demonstrate the dependence on dephasing and the reduced mass of the quasiparticle pair.

To obtain the deposing rate of the sample as a function of μ, data displayed in Figure 6.3 uses magnitudes of individual hole species propagators, normalized to the 10th order sideband to divide away pre-factors. These normalized propagators are denoted

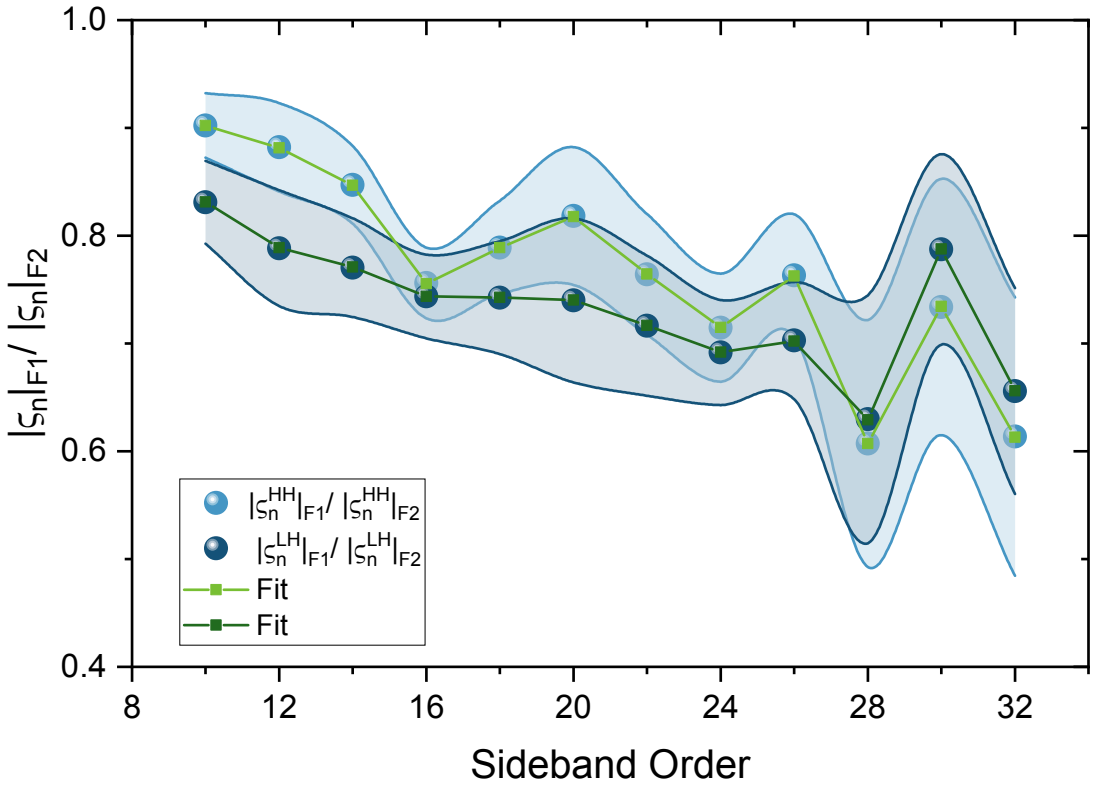

Figure 6.3 - Normalized Magnitude of Hole Propagators as a Function of Sideband Order

Measurements $|\tilde{\varsigma}_n^{hh}|_{F_1}/|\tilde{\varsigma}_n^{hh}|_{F_2}$ (light blue curve) and $|\tilde{\varsigma}_n^{lh}|_{F_1}/|\tilde{\varsigma}_n^{lh}|_{F_2}$ (dark blue curve), where the individual magnitudes of the propagators are normalized to the 10th order sideband to divide away refactors. The green curves (tough to see, as they basically overlay the blue curves) are reproduced using a qusimomentum dependent dephasing rate.

$|\tilde{\varsigma}_n^{\nu}|$. An analytical calculation can be used to calculate the dephasing value [29] from the ratio of two of these propagators taken at different field strengths. A subtlety of using the hole species specific propagators is the ability to reconstruct a hole-species specific value for dephasing, $\Gamma_{d,\nu}$. The calculated values of $|\tilde{\varsigma}_n^{\nu}|_{F_1}/|\tilde{\varsigma}_n^{\nu}|_{F_2}$ with this quasi momentum dependent dephasing are plotted as the green curves in Figure 6.3. The great overlap between experiment and theory could be indicative of an over-fit.

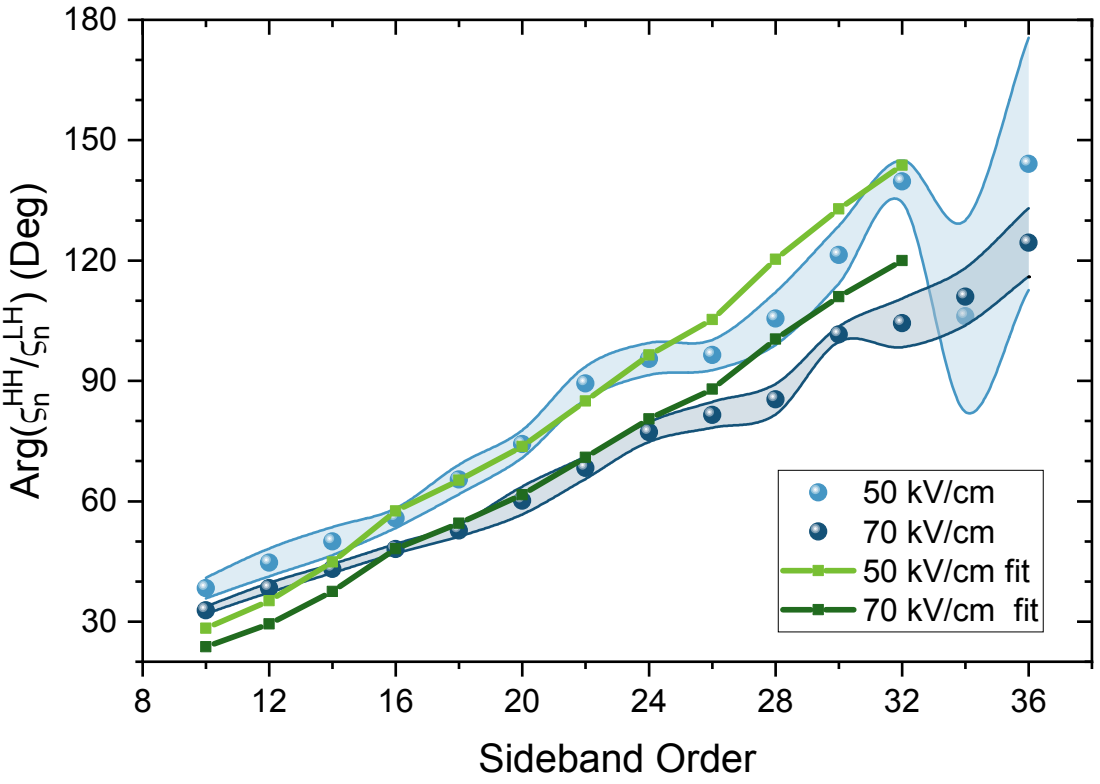

Figure 6.4 - Argument of Ratio of Propagators as a Function of Sideband Order, Dependent on THz Field Strength
Measurements of Arg($\varsigma_n^{hh}/\varsigma_n^{lh}$) (blue curves) as a function of sideband order, taken at θ = 50 degrees, at two different field strengths (F_{THz} = 70 kv/cm: dark, F_{THz} = 50 kV/cm: light). The green curves are values calculated by theory, using a semiclassical model of dephasing.

Figure 6.4 displays Arg($\varsigma_n^{hh}/\varsigma_n^{lh}$) values taken at one crystal angle (θ = 50 degrees) and two THz field strengths (F_{THz} = 70 kV/cm: dark, F_{THz} = 50 kV/cm: light). Using a cost function analysis,

$$\mathscr{C}(\mu_{hh},\mu_{lh}) = \frac{1}{n}\sum_{n}\left|\exp(i\,\mathrm{Arg}(\varsigma_n^{hh}/\varsigma_n^{lh}) - \exp(\mathrm{iArg}(\varsigma_n^{hh}/\varsigma_n^{lh})\right| \qquad (6.13)$$

a value of $\Gamma_{d,\nu}$ at each sideband order was determined to create the best agreement between the predicted values using equation 6.1 and the experimental data. The

calculated value with the best agreement, using the selected value of $\Gamma_{d,\nu}$, are displayed as the green curves. Beyond the ability for theory to well-reproduce the behavior of $\mathrm{Arg}(\varsigma_n^{hh}/\varsigma_n^{lh})$ at different field strengths, the experimental data also demonstrate the qualitative behavior expected by theory. The value of $\mathrm{Arg}(\varsigma_n^{hh}/\varsigma_n^{lh})$ should decrease with increasing field strength, in the same way the value of $l^2(n)$ and $\phi(n)$ should more rapidly with sideband order at lower field strengths. The argument for greater differences between the phases of the propagators with longer acceleration times due to a lower power THz field is the same. From this field dependent analysis, we were able to reconstruct a model of the dephasing which was *k* dependent, and specific to each hole species. Figure 6.5 displays such a reconstruction.

6.2.3 Angle Dependence of Sideband Polarization

Even with the success of this third order approximation of the semiclassical propagator reproducing the $\mathrm{Arg}(\varsigma_n^{hh}/\varsigma_n^{lh})$ and $|\tilde{\varsigma}_n^{\nu}|_{F_1}/|\tilde{\varsigma}_n^{\nu}|_{F_2}$, and reconstructing an effective model for $\Gamma_{d\nu}(\mathbf{k})$, there was no convincing reconstruction of the Luttinger parameters using this model. Some of these complications can be circumvented by introducing a simpler description of ς_n^{ν} through the LIT approximation. Going back to the discussions of Chapters 3 and 4, the LIT approximation has an analytical model for the behavior of ς_n^{ν}, $l^2(n)$ and $\phi(n)$ as a function of THz-to-crystal orientation. In order to apply the LIT, the data should show sideband polarization changing as a function of this crystal angle.

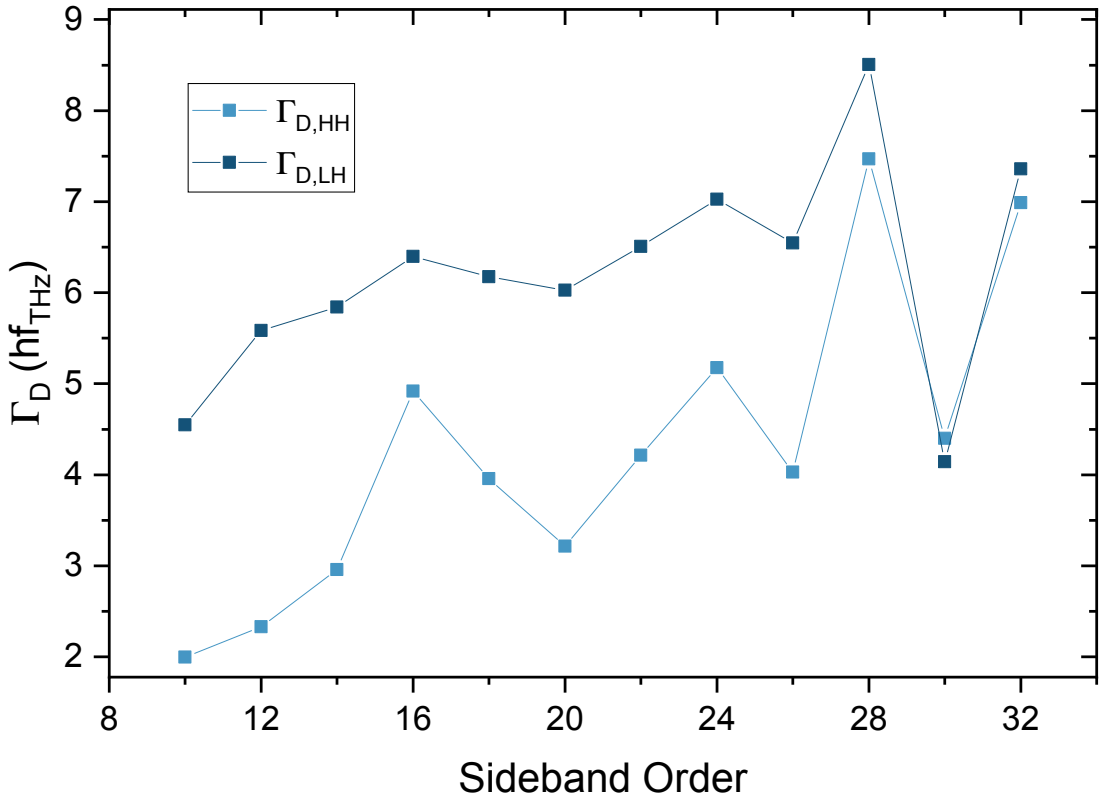

Figure 6.5 - Reconstructed Quasmomentum Dependent Dephasing Value From Sideband Data
Values of $\Gamma_{d,\nu}$ for the hh and lh pairs, as a function of sideband order (analogous to quasi momentum dependent). The dark blue curve is the lh dataset, and the light blue curve is the hh dataset. This reconstruction is derived from the data in Figures 6.3 and 6.4.

Figure 6.6 displays $l^2(n)$ and $\phi(n)$ observed at different crystal angles From the data, we can see there is a clear dependence on outgoing sideband polarization and the crystal angle, in accordance with the LIT model of the propagator and subsequent Jones matrix elements. The different colored curves are data at different θ, moving from θ = -135 degrees (red) to θ = 45 degrees (dark blue), defined in the legend and depicted in the upper inset. The upper row displays the observed $l^2(n)$ at these different crystal orientations, all of which vary with sideband order, just like the data presented in

Chapters 4 and 5. The rate at which $l^2(n)$ changes as a function of sideband order varies with crystal angle. This is equivalent to the difference in the reduced mass terms between the e-hh and e-lh pairs changing with crystal angle, as outlined in Eq. 6.4.

Figure 6.7 has a clearer depiction of the dependence of THz-to-crystal axis orientation dependence, with the x-axis in this plot being the crystal angle where the dataset was acquired. Here the different colored bands are the different sideband orders, from 10th (red) to the 34th order (purple). The different rows are data taken with different NIR polarizations (first from top: antidiagonal, second: diagonal, third: horizontal, fourth: vertical). There is a clear variance of the $\left|\hat{\mathbf{E}}(n)\right\rangle$ at different crystal angles, closely following the periodicity of the $\mathrm{Arg}(\varsigma_n^{hh}/\varsigma_n^{lh})$ data in Figure 6.1, especially the diagonal and antidiagonal data. For reasons unknown at the moment, the horizontal and vertical NIR excitations have a period and phase more closely resembling the $\left|(\varsigma_n^{hh}/\varsigma_n^{lh})\right|$ data in Figure 6.2.

This preliminary recasting of the data into the $\left|\hat{\mathbf{E}}(n)\right\rangle$ holds the promise of connecting a phenomena well described by the LIT approximation, the changing sideband polarization as a function of sideband order, to it's dependence on crystal orientation. With an analytical model more straightforward to evaluate, future analysis could yield the Luttinger parameters.

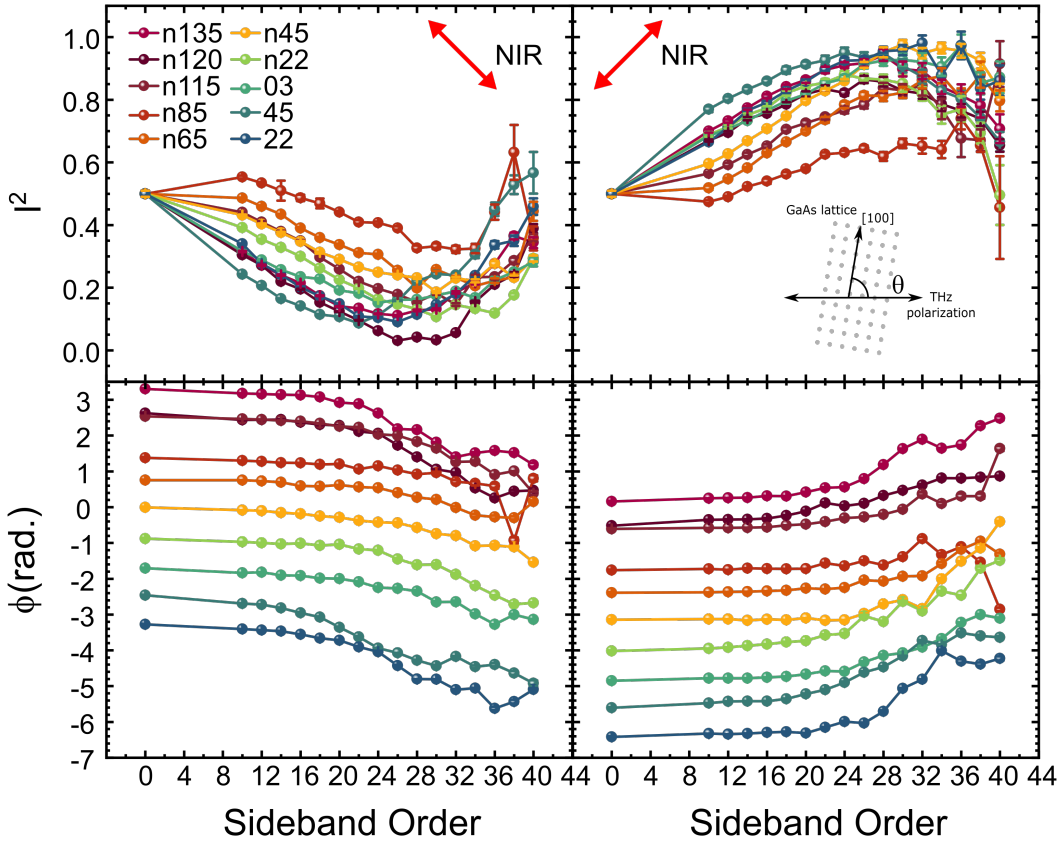

Figure 6.6 - Sideband Electric Field, Measured at Different Lattice Orientations With Respect to the THz Field

Observed $\left|\hat{\mathbf{E}}(n)\right\rangle$, parameterized by $l^2(n)$ and $\phi(n)$, The different colored curves are data from HSG experiments conducted at different THz-to-crystal axis orientations, depicted in the cartoon in the upper right square, defined in the legend. The upper row is the observed $l^2(n)$, and the lower row is the $\phi(n)$. The left column is data from HSG experiments with an antidiagonally polarized NIR excitation, and the right column is data from diagonally polarized NIR excitations.

6.3 APPLICATIONS TO FUTURE MATERIALS

Beyond bulk GaAs, there are plenty of materials on which HaRφως can be conducted. As Chapter 1 outlined in section 1.2.1, any gapped system is a potential system to host HSG, so long as the criteria outlined in that section are met. Other groups have conducted HSG experiments on quantum materials [39-41, 102, 103] and incorporated Stokes polarimetry

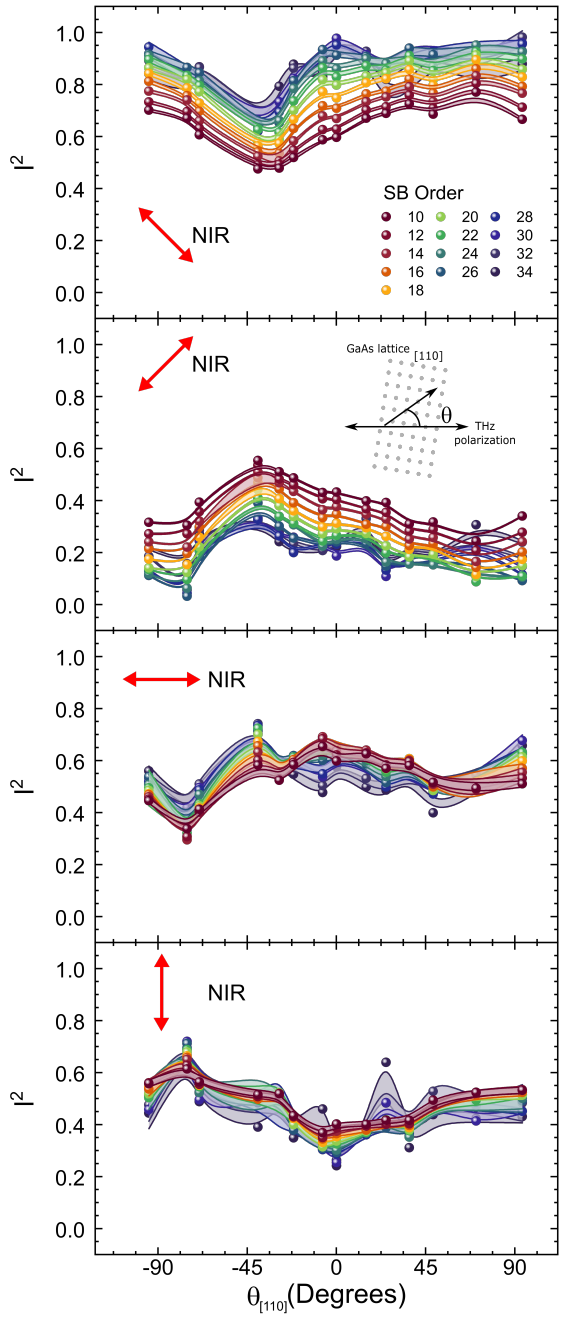

Figure 6.7 - Sideband $I^2(n)$ as a Function of Crystal Axis Orientations With Respect to the THz Field

Observed $I^2(n)$ at the different THz-to-crystal axis orientations probed in HSG experiments, depicted in the cartoon in the second panel from the top. Each colored band is a different sideband order, from the 10th (red) to the 34th (purple) order, defined in the legend in the top panel. Each panel is data taken with different NIR polarizations (first from top: antidiagonal, second: diagonal, third: horizontal, fourth: vertical).

on ultrafast THz experiments [88]. Incorporating HSG polarimetry experiments into ultrafast non-equilibrium experiments has the potential to reveal more about the microscopic physics of these quantum materials, down to the single-particle wavefunction level. The main bottleneck remains the theory, especially for materials more exotic than GaAs. However, as this thesis has demonstrated, there are many knobs to tune in HSG polarimetry in order to determine properties of the effective Hamiltonian governing quasiparticle dynamics in quantum condensed matter. Well controlled experiments which carefully probe the dependence on different Hamiltonian parameters through the adjustment of experimental conditions. Experiments testing the dependence on THz field strength, NIR excitation wavelength, the lattice temperature, and the quasiparticle trajectories through the Brillouin zone have yielded information about the Luttinger Hamiltonian in bulk GaAs and are posed to yield information about future quantum materials

Chapter 7 — Future Non-Equilibrium THz Polarimetry Experiments

Given the successes of HSG polarimetry reconstructing different components of the effective Hamiltonian of bulk GaAs, the question becomes to what other systems can this methodology be extended? Bulk GaAs is a workhorse of the modern electronics community [45] and is relatively well characterized, making it a great testbed for developing the method of HSG polarimetry. However, to increase the usefulness of the technique, more novel materials also need to be characterized. Also, some systems provide avenues of exploration unavailable in a topologically trivial system like unstrained bulk GaAs. In this chapter, I will detail what other systems could be feasibly probed by HSG polarimetry, and what unique questions could be answered in the process.

I hope this chapter provides context for the reader of what possibilities lie ahead for HSG experimentation, and inspiration for future graduate students seeking new research directions.

7.1 NIRED HSG ON MZM CANDIDATE MATERIALS

As the previous Chapter demonstrated, HSG polarimetry measurements are sensitive to the NIR excitation wavelength. The analytical model of quasiparticle propagators in bulk GaAs could be applied to related III-V materials of interest like InSb [91, 101]. The use of NIR excitation dependent (NIRED) measurements of sideband polarizations to reconstruct the dynamical gap of high SOC semiconductors, a material parameter of great importance for a key component of a topological quantum computer [90-94, 101, 104-106].

7.1.1 Knowledge (of the) Gap

In order to induce a topological state in a hybridized MZM system, the free energy of the quasiparticles needs to be tuned to a level predetermined by the effective Hamiltonian [92]. The Zeeman term, modulated by the Rashba SOC parameter in the semiconductor, coupled with the superconducting gap term, will determine the size of the topological gap [96, 107, 108]. Experimentally, the size of this gap needs to be known to determine the phase space of in-plane electric fields, set by a potential, and the out-of-plane magnetic field which have a topological gap. With this knowledge, a gate electrode can tune the Fermi surface to this gapped regime.

Previous works have speculated the value of the SOC parameters at their own peril, leading to untrustworthy results. For such highly calibrated systems, probing and accounting for disorder is also important [108], something transport measurements are not always equipped to measure. We know HSG is sensitive to disorder, and can probe the bulk-microscopic physics of a sample at the scale of the NIR beam spot. This sensitivity, coupled with the ability to resolve the dynamical gap of driven quasiparticles, makes HSG a powerful non-destructive probe of semiconductors theorized to be a part of MZM die.

7.1.2 Extrapolate NIRED Success on GaAs to More Novel Materials

HSG polarimetry is sensitive to the δ_ν expression in the dephasing, and is able to reconstruct properties of the Luttinger Hamiltonian, which is inherently a SOC effective Hamiltonian [45, 56, 58, 62]. By performing NIRED HSG on high-SOC semiconductors, we can measure the dynamical gap of the different valence bands, and with that the spin-orbit coupling parameters of the Hamiltonian. Such a result would be a major contribution to the material science community, providing an experimentally measured value for candidate materials for a topological quantum computer [91, 96, 101]. As a method, NIRED HSG will provide *in situ* characterization for materials incorporated into these systems, providing the precision required for fault-tolerant quantum computing.

7.2 MEASUREMENT OF TOPOLOGICAL HETEROSTRUCTURES

As bulk sensitive optical probes, HSG and HHG allow for a non-destructive measurement of behavior imbedded inside a heterostructure. One example of interest is a

topological superconducting state (TSC) at the interface of a topological insulator (TI) and superconductor (SC). Previous HHG polarimetry experiments have demonstrated sensitivity to topology, with a distinct shift in the harmonic frequency as a result of varying the carrier envelope phase (CEP) of the driving THz field [88]. This unique behavior, called non-integer HHG, with the top panel depicting the shift if harmonic frequency as a function of peak hight, and the bottom panel displaying the shift in frequency between the even and odd order harmonics. The top curve consists of experimental data, and the bottom curve is a calculation from the non-equilibrium semiconductor Bloch equations (SBEs). HSG experiments would resolve a microscopic picture of the quasiparticles and the effective Hamiltonian parameters of topological systems.

7.2.1 the Other Phase: Topological Phase

For adiabatically driven quasiparticles driven around regions of the Brillouin zone with non-trivial topologies, the wavefunction develops a path dependent phase, separate from the dynamical phase, called the geometric phase [109-111]. Along with the dynamical phase, of which HSG has demonstrated it's sensitivities [63, 112], sideband polarimetry should also be sensitive to the geometric phase.

7.2.2 Nontrivial Topologies at the Interface

Nonlinear harmonic experiments have already been conducted on the TI portion (Bi_2Se_3) of a TSC candidate [113], and polarimetry experiments of higher order harmonics will be a key building block to reconstructing the topological phases of carriers in Bi_2Se_3 and those of other topological systems.

Applying polarimetry experiments to engineered systems with theorized TSC will provide opportunities to (1) simultaneously characterize the topological nature of the observed superconductivity phenomena through unique photon phases and (2) characterize the microscopic phenomena which manifest the topological phase. The first will be evident in the non-integer nature of the HHG spectra [88], and the second through observed polarimetry measurements connected to SBEs and the system's effective Hamiltonian. Understanding the underlying mechanisms of TSC through HHG polarimetry will allow for greater engineering of systems in future device design, which would allow for greater control over parameters like qubit coherence and fidelity. All of these developments are of great interest to the quantum computing and material science community.

7.3 LOW GAP HSG

Whereas the last section detailed the contributions of HHG polarimetry to topological materials, previous and proposed, there is a clear gap in the possibilities of HSG experiments on topological systems. For one, most of these systems of interest either have no gap, or a gap on the THz energy scale. The two existing HSG apparatus both are configured with optical excitation pulses, meaning the photons provide too much energy, exciting the quasiparticles out of the topologically non-trivial region.

7.3.1 Probing Systems With Low to no Band Gap

The gapless nature of Weyl and Dirac fermions [114, 115], both or which are theorized to have non-trivial topological phases [105, 116-118] requires a retooling of

current HSG experimentation and a shift away from HHG experimentation of these systems in the broader condensed matter community. The latter motivates the former, and the latter is necessary due to insufficiencies in HHG experimentation. Given the high field strengths used for HHG experimentation, optical experiments are not able to disaggregate the contributions of quasiparticles occupying many levels of excited states in the system. The monochromatic nature of HHG means both interband and intraband currents contribute to the final polarization signal [29]. A two frequency experiment, like HSG, will be able to isolate the intraband dynamics of quasiparticles and resolve topological phases of the wavefunction.

In HSG experimentation, the THz path defines the trajectories taken by the quasiparticle through the Brillouin zone. In this way, our non-equilibrium drive can trace out different paths, of which the topological phase is dependent. In this way, HSG polarimetry would offer a richer exploration of the topological regions of interest when compared to linear optical experiments or transport measurements, which normally only probe averages of topological values over fractions or the entirety of the Brillouin zone [119, 120].

In any experimental method which has never been attempted, there are plenty of non-obvious situations for pitfalls. A known limiting factor of quasiparticle collisions in topological systems is the anomalous velocity from the geometric phase [121]. Acting like a magnetic field, the Berry curvature at the regions of non-trivial topology will push the quasiparticles of different effective masses in a way where annihilation is not guaranteed. Therefore, another external magnetic field would probably be required to

counteract the anomalous velocities and insure the quasiparticles collide. Knowledge of the driving field's polarization, subsequent quasiparticle trajectories, and the magnetic field required to balance the effects of Berry curvature should reveal information about the topological phases and effective masses of the quasiparticles in our system.

Citations

[1] D. J. Griffiths, Introduction to Quantum Mechanics. Upper Saddle River, NJ: Pearson, 1995.

[2] M. F. Crommie, C. P. Lutz and D. M. Elgler, "Imaging standing waves in a two-dimensional electron gas," Nature, vol. 363, pp. 524 - 527, 1993.

[3] Y. Hasegawa and P. Avouris, "Direct Observation of Standing Wave Formation at Surface Steps Using Scanning Tunneling Spectroscopy," Phys. Rev. Lett., vol. 71, pp. 1071 - 1074, 1993.

[4] E. J. Heller, M. F. Crommie, C. P. Lutz and D. M. Elgler, "Scattering and absorbtion of surface electron waves in quantum corrals," Nature, vol. 1994, pp. 464 - 466, 1994.

[5] B. L. Altshuler, D. Khmel’nitzkii, A. I. Larkin and P. A. Lee, "Magnetoresistance and Hall effect in a disordered two dimensional electron gas," Phys. Rev. B, vol. 22, pp. 5142 - 5153, 1980.

[6] G. Ndbashimiye, S. Ghimire, M. Wu, D. A. Browne, K. J. Schafer, M. B. Gaarde and D. A. Reis, "Solid-state harmonics beyond the atomic limit," Nature, vol. 534, pp. 520 - 523, 2016.

[7] H. Liu, Y. Li, Y. S. You, S. Ghimire, T. F. Heinz and D. A. Reis, "High-harmonic generation from an atomically thin semiconductor," Nat. Phys., vol. 13, pp. 262 - 265, 2017.

[8] Y. S. You, D. A. Reis and S. Ghimire, "Anisotropic high-harmonic generation in bulk crystals," Nat. Phys., vol. 13, pp. 345 - 349, 2017.

[9] D. N. Basov, R. D. Averitt and D. Hsieh, "Towards properties on demand in quantum materials," Nat. Mat., vol. 16, p. 1077, 2017.

[10] P. M. Paul, E. S. Toma, P. Breger, G. Mullot, F. Augé, P. Balcou, H. G. Muller and P. Agostini, "Observation of a Train of Attosecond Pulses from High Harmonic Generation," Science, vol. 292, pp. 1689 - 1692, 2001.

[11] N. Dudovich, O. Smirnova, J. Levesque, Y. Mairesse, M. Y. Ivanov, D. M. Villeneuve and P. B. Corkum, "Measuring and controlling the birth of attosecond XUV pulses," Nat. Phys., vol. 2, pp. 781 - 786, 2006.

[12] S. Ghimire, A. D. DiChiara, E. Sistrunk, P. Agostini, L. F. DiMauro and D. A. Reis, "Observation of high-order harmonic generation in a bulk crystal," Nat. Phys., vol. 7, p. 138, 2011.

[13] G. Vampa, C. R. McDonald, G. Orlando, D. D. Klug, P. B. Corkum and T. Brabec, "Theoretical Analysis of High-Harmonic Generation in Solids," Phys. Rev. Lett., vol. 113, p. 073901, 2014.

[14] M. Hohenleutner, F. Langer, O. Schubert, M. Knorr, U. Hunter, S. W. Koch, M. Kira and R. Huber, "Real-time observation of interfering crystal electrons in high-harmonic generation," Nature, vol. 523, pp. 572-575, 2015.

[15] T. T. Luu, M. Garg, S. Y. Kruchinin, A. Moulet, M. T. Hassan and E. Goulielmakis, "Extreme ultraviolet high-harmonic spectroscopy of solids," Nature, vol. 521, pp. 498-502, 2015.

[16] G. Vampa, T. J. Hammond, N. Thiré, B. E. Schmidt, F. Légaré, C. R. McDonald, T. Brabec and P. B. Corkum, "Linking high hamronics from gases and solids," Nature, vol. 522, pp. 462 - 464, 2015.

[17] G. Vampa, T. J. Hammond, N. Thiré, B. E. Schmidt, F. Légaré, C. R. McDonald, T. Brabec, D. D. Klug and P. B. Corkum, "All-Optical Reconstruction of Crystal Band Structure," Phys. Rev. Lett., vol. 115, p. 193603, 2015.

[18] N. Tancogne-Dejan, M. A. Sentef and A. Rubio, "Ultrafast Modification of Hubbard U in a Strongly Correlated Material: Ab initio High-Harmonic Generation in NiO," Phys. Rev. Lett., vol. 121, p. 097402, 2018.

[19] G. Vampa, S. Vasilyev, H. Liu, M. Mirov, P. Bucksbaum and D. A. Reis, "Characterization of high-harmonic emission from ZnO up to 11 eV with a Cr:ZnS high-repetition-rate source," Optics Letters, vol. 44, p. 259, 2019.

[20] E. Goulielmakis and T. Brabec, "High harmonic generation in condensed matter," Nat. Photo., vol. 16, pp. 411-421, 2022.

[21] L. Yue and M. B. Gaarde, "Introductoin to theory of high-harmonic generation in solids: tutorial," JOSAB, vol. 39, pp. 535-555, 2022.

[22] C. Heide, Y. Kobayashi, A. C. Johnson, T. F. Heinz, D. A. Reis, F. Liu and S. Ghimire, "High-harmonic generation from artificially stacked 2D crystals," Nanophotonics, 2023.

[23] M. Garg, M. Zhan, T. T. Luu, H. Lakhotia, T. Klostermann, A. Guggenmos and E. Goulielmakis, "Multi-petahertz electronic metrology," Nature, vol. 538, pp. 359 - 363, 2016.

[24] A. J. Uzan, G. Orenstein, Á. Jiménez-Galán, C. McDonald, R. E. F. Silva, B. D. Bruner, N. D. Kilmkin, V. Blanchet, T. Arusi-Parpar, M. Krüger, A. N. Rubtsov, O. Smirnova, M. Ivanov, B. Yan, T. Brabec and N. Dudovich, "Attosecond spectral singularities in solid-state high-harmonic generation," Nat. Photo., vol. 14, pp. 183-187, 2020.

[25] N. Yoshikawa, T. Tamaya and K. Tanaka, "High-harmonic generation in graphene enhanced by elliptically polarized light excitation," Science, vol. 356, pp. 736 - 738, 2017.

[26] A. J. Uzan-Narovlansky, Á. Jiménez-Galán, G. Orenstein, R. E. F. Silva, T. Arusi-Parpar, S. Shames, B. D. Bruner, B. Yan, O. Smirnova, M. Ivanov and N. Dudovich, "Observation of light driven band structure via multiband high-harmonic spectroscopy," Nat. Photo., vol. 16, pp. 428-432, 2022.

[27] D. Golde, T. Meier and S. W. Koch, "High harmonics generated in semiconductor nanostructures by the coupled dynamics of optical inter- and intraband excitations," Phys. Rev. B, vol. 77, p. 075330, 2008.

[28] L. Li, P. Lan, X. Zhu and P. Lu, "Huygens-Fresnel Picture of High Harmonic Generation in Solids," Phys. Rev. Lett., vol. 127, p. 223201, 2021.

[29] Q. Wu and M. S. Sherwin, "Explicit formula for high-order sideband polarization by extreme tailoring of Feynman path integrals," Phys. Rev. B, vol. 107, p. 174308, 2023.

[30] N. H. Linder, G. Refael and V. Galitski, "Floquet topological insulator in semiconductor quantum wells," Nat. Phys., vol. 7, p. 490, 2011.

[31] J.-Y. Shan, M. Ye, H. Chu, S. Lee, J.-G. Park, L. Balents and D. Hsieh, "Giant modulation of optical nonlinearity by Floquet engineering," Nature, vol. 600, pp. 235 - 239, 2021.

[32] Y. H. Wang, H. Steinberg, P. Jarillo-Herrero and N. Gedik, "Observation of Floquet-Bloch States on the Surface of a Topological Insulator," Science, vol. 342, p. 453, 2013.

[33] S. Ito, M. Schüler, M. Meierhoffer, S. Schlauderer, J. Freudenstein, J. Reimann, D. Afanasiev, K. A. Kokh, O. E. Tereshchenko, J. Güdde, M. A. Sentef, U. Höfer and R. Huber, "Build-up and dephasing of Floquet-Bloch bands on subscycle timescales," Nature, vol. 616, p. 696, 2023.

[34] C. Yang, I. Esin, C. Lewandowski and G. Refael, "Optical Cotnrol of Slow Topological Electrons in Moiré Systems," arXiv:2301.02248v4, 2023.

[35] R. B. Liu and B. F. Zhu, "High-order THz-sideband generation in semiconductors," AIP Conf. Proc., vol. 893, pp. 1455 - 1456, 2007.

[36] B. Zaks, R. B. Liu and M. S. Sherwin, "Experimental observation of electron - hole recollisions," Nature, vol. 483, pp. 580 - 583, 2012.

[37] B. Zaks, H. Banks and M. S. Sherwin, "High-order sideband generation in bulk GaAs," Appl. Phys. Lett., vol. 102, p. 012104, 2013.

[38] J. M. Ziman, Principles of the Theory of Solids. Cambridge: Cambridge University Press, 1964.

[39] F. Langer, C. P. Schmid, S. Schlauderer, M. Gmitra, J. Fabian, P. Nagler, C. Schüller, T. Korn, P. G. Hawkins, J. T. Steiner, U. Huttner, S. W. Koch, M. Kira and R.

Huber, "Lightwave valleytronics in a monolayer of tungsten diselenide," Nature, vol. 557, pp. 76 - 80, 2018.

[40] M. Borsch, C. P. Schmid, L. Weigl, S. Schlauderer, N. Hofman, C. Lange, J. T. Steiner, S. W. Koch, R. Huber and M. Kira, "Super-resolution lightwave tomography of electronic bands in quantum materials," Science, vol. 370, pp. 1204-1207, 2020.

[41] J. Freudenstein, M. Borsch, M. Meierhoffer, D. Afanasiev, C. P. Schmid, F. Sandner, M. Liebich, A. Girnghuber, M. Knorr, M. Kira and R. Huber, "Attosecond clocking of correlations between Bloch electrons," Nature, vol. 610, pp. 290 - 295, 2022.

[42] L. V. Keldysh, "Ionization in the field of a strong electromagnetic wave," Sov. Phys. JTEP, vol. 20, p. 1307, 1965.

[43] K. B. Nordstrom, K. Johnson, S. J. Allen, A.-P. Jauho, B. Birnir, J. Kono, T. Noda, H. Akiyama and H. Sakaki, "Excitonic Dynamical Franz-Keldysh Effect," Phys. Rev. Lett., vol. 81, p. 457, 1998.

[44] I. Institute. http://www.ioffe.ru/SVA/NSM/Semicond/GaAs/bandstr.html#Basic (accessed 04/05, 2023).

[45] I. Vurgaftman, J. R. Meyer and L. R. Ram-Mohan, "Band parameters for III-V compund semiconductors and their alloys," J. Appl. Phys., vol. 89, pp. 5815 - 5875, 2001.

[46] T. Cheiwchanchamnangij and W. R. Lambrecht, "Quasiparticle band structure calculation of monolayer, bilayer, and bulk MoS2," Phys. Rev. B., vol. 85, p. 205302, 2012.

[47] A. M. Jones, H. Yu, N. J. Ghimire, S. Wu, G. Aivazian, J. S. Ross, B. Zhao, J. Yan, D. G. Mandrus, D. Xiao, W. Yao and X. Xu, "Optical Generation of excitonic valley coherence in monolayer WSe2," Nat. Nano., vol. 8, p. 634, 2013.

[48] J. S. Ross, S. Wu, H. Yu, N. J. Ghimire, A. M. Jones, G. Aivazian, J. Yan, D. G. Mandrus, D. Xiao, W. Yao and X. Xu, "Electrical control of neutral and charged excitons in a monolayer semiconductor," Nat. Comm., vol. 4, 1474, 2013.

[49] M. M. Ugeda, A. J. Badley, S. F. Shi, F. H. da Jornada, Y. Zhang, D. Y. Qui, W. Ruan, S. K. Mo, Z. Hussain, Z. Y. Shen, F. Wang, S. G. Louie and M. F. Crommie, "Giant bandgap renormalization and excitonic effects in a monolayer transition metal dichalcogenide semiconductor," Nat. Mat., vol. 13, p. 1091, 2014.

[50] A. Arora, M. Koperski, K. Nogajewski, J. Marcus, C. Faugeras and M. Potemski, "Excitonic resonances in thin films of WSe2: from monolayer to bulk materials," Nanoscale, vol. 7, p. 10421, 2015.

[51] A. Arora, K. Nogajewski, M. Molas, M. Koperski and M. Potemski, "Exciton band structure in layered MoSe2: from a monolayer to the bulk limit," Nanoscale, vol. 7, p. 20769, 2015.

[52] D. C. Valovcin, "High-Order Sideband Generation for Creating Optical Frequency Combs and Probing Bloch Wavefunctions," Physics, Univeristy of California, Santa Barbara, 2019.

[53] R. W. Boyd, Nonlinear Optics. Academic Press.

[54] Y. R. Shen, The principles of nonlienar optics. New York: John Wiley & Sons, Inc., 1984.

[55] A. G. Markelz, N. G. Asmar, E. G. Gwinn, M. S. Sherwin, C. Nguyen and H. Kroemer, "Subcubic power dependence of third-harmonic generation for in-plane, far infrared excitaoitn of InAs quantum wells," Semicond. Sci. Technol., vol. 9, p. 634, 1994.

[56] J. M. Luttinger and W. Kohn, "Motion of Electrons and Holes and Perturbed Periodic Fields," Phys. Rev., vol. 97, pp. 869 - 883, 1955.

[57] J. M. Luttinger, "Quantum Theory of Cycloton Resonance in Semiconductors: A General Theory," Phys. Rev., vol. 102, p. 1030, 1956.

[58] P. Y. Yu and M. Cardona, Fundamentals of Semiconductors; Physics and Materials Properties (Graduate Texts in Physics). Heidelberg: Springer.

[59] G. Dresselhaus, "Spin-Orbit Coupling Effects in Zinc Blende Structures," Phys. Rev., vol. 100, p. 580, 1955.

[60] N. W. Ashcroft and N. D. Mermin, Solid State Physics. Toronto, Canada: Brooks/ Cole, 1976.

[61] J. H. Davies, The Physics of Low-Dimensional Semiconductors. Cambridge, England: Cambridge Univeristy Press, 1998.

[62] L. C. Lew Yan Voon and M. Wllatzen, The k*p Method; Electronic Properties of Semiconductors. Berlin: Springer, 2009.

[63] J. B. Costello*, S. D. O'Hara*, Q. Wu*, D. C. Valovcin, L. Pfeiffer, K. West and M. S. Sherwin, "Reconstruction of Bloch wavefucntions of holes in a semiconductor," Nature, vol. 599, pp. 57 - 61, 2021.

[64] G. Ramian, "The new UCSB free-electron lasers," Nuclear Instruments and Methods in Physics Research A, vol. 318, pp. 225-229, 1992.

[65] J. Burghoorn, J. P. Kaminski, R. C. Strijbos, T. O. Klaassen and W. T. Wenckebach, "Generation of subnanosecond high power far infrared pulses using a FEL pumped passive resonator," Nuclear Instruments and Methods in Physics Research A, vol. 92, p. 85, 1922.

[66] J. P. Kaminski, J. S. Spector, C. L. Felix, D. P. Enyeart, D. T. White and G. Ramian, "Far-infraret cavity dumping coupling of the UC Santa Barbara free-electron laser," Appl. Phys. Lett., vol. 57, p. 2770, 1990.

[67] M. F. Doty, B. E. Cole, B. T. King and M. S. Sherwin, "Wavelength-specific laser activated switches for improved contrast ratio in gneeration of short THz pulses," Rev. Sci. Instrum, vol. 75, p. 2921, 2004.

[68] S. Takahashi, G. Ramain, M. S. Sherwin, L.-C. Brunel and J. van Tol, "Submegahertz linewidth at 240 GHz from an injection-locked free-electron laser," Appl. Phys. Lett., vol. 91, p. 174102, 2007.

[69] S. G. Carter, J. Cerne and M. S. Sherwin, in Terahertz Spectrostopy, Principles and Applications, S. L. Dexheimer Ed., (Optical Science and Engineering, B. J. Thomson, Ed. Boca Raton, Florida: CRC Press, 2008, ch. Optical Response of Semiconductor Nanostructures in Terahertz Fields Generated by Electrostatic Free-Electron Lasers.

[70] S. Takahashi, G. Ramian and M. S. Sherwin, "Cavity dumping of an ingection-locked free-electron laser," Appl. Phys. Lett., vol. 95, p. 234102, 2009.

[71] S. Takahashi, L.-C. Brunel, D. T. Edwards, J. van Tol, G. Ramian, S. Han and M. S. Sherwin, "Pulsed electron paramagnetic resonance spectroscopy powered by a free-electron laser," Nature, vol. 489, p. 409, 2012.

[72] A. Einstein, "Über einen die Erzeugung und Verwandlung des Lichtes betreffenden heuristischen Gesichtspunkt," Ann. Phys., vol. 17, pp. 132 - 148, 1905.

[73] A. Einstein, "Zur Elektrodynamik bewegter Körper," Ann. Phys., vol. 17, pp. 891 - 921, 1905.

[74] J. P. Kaminski, J. S. Spector, C. L. Felix, D. P. Enyear, D. T. White and G. Ramian, "Far-infraret cavity dumping coupling of the UC Santa Barbara free-electron laser," Appl. Phys. Lett., vol. 57, p. 2770, 1990.

[75] S. Takahaski, L.-C. Brunel, D. T. Edwards, J. van Tol, G. Ramian, S. Han and M. S. Sherwin, "Pulsed electron paramagnetic resonance spectroscopy powered by a free-electron laser," Nature, vol. 489, p. 409, 2012.

[76] H. Banks, Q. Wu, D. C. Valovcin, S. Mack, A. C. Gossard, L. Pfeiffer, R. B. Liu and M. S. Sherwin, "Dynamical Birefringence: Electron-Hole Recollisions as Probes of Berry Curvature," Phys. Rev. X, vol. 7, p. 041042, 2017.

[77] R. C. Jones, "A New Calculus for the Treatment of Optical Systems," J. O. S. A., vol. 31, p. 488, 1941.

[78] G. P. Thomson and A. Reid, "Diffraction of Cathod Rays by a Thin Film," Nature, vol. 119, p. 890, 1927.

[79] C. J. Davisson and L. H. Germer, "Reflection of Electrons by a Crystal of Nickel," PNAS, vol. 14, pp. 317 - 322, 1928.

[80] A. A. Michelson and E. W. Morley, "On the Relative Motion of the Earth and the Luminiferous Ether," American Journal of Science, vol. 203, p. 333, 1887.

[81] B. P. Abbot, "Observation of Graviational Waved from a Binary Black Hole Merger," Phys. Rev. Lett., vol. 116, p. 061102, 2016.

[82] O. Carnal and J. Mlynek, "Young's Double-Slit Experiment with Atoms: A Simple Atom Interferometer," Phys. Rev. Lett., vol. 66, pp. 2689 - 2692, 1991.

[83] C. Solaro, C. Debavelaere, P. Cladé and S. Guellati - Khelifa, "Atom Interferometer Driven by a Picosecond Frequency Comb," Phys. Rev. Lett., vol. 129, p. 173204, 2022.

[84] A. Zaïr, M. Holler, A. Guandalini, F. Schapper, J. Biegert, L. Gallmann, U. Keller, A. S. Wyatt, A. Monmayrant, I. A. Walmsley, E. Cormier, T. Auguste, J. P. Caumes and P. Salières, "Quantum Path Interferences in High-Order Harmonic Generation," Phys. Rev. Lett., vol. 100, p. 143902, 2008.

[85] R. Atanasov, A. Haché, J. L. P. Hughes and H. M. van Driel, "Coherent Control of Photocurrent Generation in Bulk Semiconductors," Phys. Rev. Lett., vol. 76, no. 10, pp. 1703 - 1706, 1996.

[86] N. Yoshikawa, K. Nagai, K. Uchida, Y. Takagushi, S. Sasaki, Y. Miyata and K. Tanaka, "Interband resonant high-harmonic generation by valley polarized electron-hole pairs," Nature Communications, 2019.

[87] H. K. Avetissian, G. F. Mkrtchian and K. Z. Hatsagortsyan, "Many-body effects for excitonic high-order wave mixing in monolayer transition metal dichalcogenides," Phys. Rev. Research, vol. 2, p. 023072, 2020.

[88] C. P. Schmid, L. Weigl, P. Grössing, V. Junk, C. Gorini, S. Schlauderer, S. Ito, M. Meierhoffer, N. Hofman, D. Afanasiev, J. Crewse, K. A. Kokh, O. E. Tereshchenko, J. Güdde, F. Evers, J. Wilhelm, K. Richter, U. Höfer and R. Huber, "Tunable non-integer high-harmonic generation in a topological insulator," Nature, vol. 593, pp. 385 - 390, 2021.

[89] H. Banks, B. Zaks, F. Yang, S. Mack, A. C. Gossard, R. B. Liu and M. S. Sherwin, "Terahertz Electron-Hole Recollisions in GaAs/AlGaAs Quantum Wells: Robustness to Scattering by Optical Phonons and Thermal Fluctuations," Phys. Rev. Lett., vol. 111, p. 267402, 2013.

[90] A. Y. Kitaev, "Fault-tolerant quantum computation by anyons," Ann. Phys., vol. 303, pp. 2-30, 2003.

[91] J. Alicea, "Majorana fermions in a tunable semiconductor device," Phys. Rev. B, vol. 81, p. 125318, 2010.

[92] Y. Oreg, G. Refael and F. von Oppen, "Helical Liquids and Majorana Bound States in Quantum Wires," Phys. Rev. Lett., vol. 105, p. 177002, 2010.

[93] C. Nayak, S. H. Simon, A. Stern, M. Freedman and S. Das Sarma, "Non-Abelian anyons and topological quantum computation," Rev. Mod Phys., vol. 80, pp. 1083 - 1159, 2008.

[94] C. Knapp, M. Zaletel, D. E. Liu, M. Cheng, P. Bonderson and C. Nayak, "The Nature and Correction of Diabatic Errors in Anyon Braiding," Phys. Rev. X, vol. 6, p. 041003, 2016.

[95] E. Majorana, "Teoria simmetrica dell'elettrone e del positrone," Cimento, vol. 14, p. 171, 1937.

[96] M. Quantum, "InAs-Al Hybrid Devices Passing the Topological Gap Protocol," arXiv:2207.02472v3, 2022.

[97] F. Arute, K. Arya, R. Babbush, D. Bacon, J. C. Bardin, R. Barends, R. Biswas, S. Boixo, F. G. S. L. Brandao, D. A. Buell, B. Burkett, Y. Chen, Z. Chen, B. Chiaro, R. Collins, W. Courtney, A. Dunsworth, E. Farhi, B. Foxen, A. Fowler, C. Gidney, M. Giustina, R. Graff, K. Guerin, S. Habegger, M. P. Harrigan, M. J. Hartmann, A. Ho, M. Hoffmann, T. Huang, T. S. Humble, S. V. Isakov, E. Jeffrey, Z. Jiang, D. Kafri, K. Kechedzhi, J. Kelly, P. V. Klimov, S. Knysh, A. Korotkov, F. Kostritsa, D. Landhuis, M. Lindmark, E. Lucero, D. Lyakh, S. Mandrà, J. R. McClean, M. McEwen, A. Megrant, X. Mi, K. Michielsen, M. Mohseni, J. Mutus, O. Naaman, M. Neeley, C. Neill, M. Y. Niu, E. Ostby, A. Petukhov, J. C. Platt, C. Quintana, E. G. Rieffel, P. Roushan, N. C. Rubin, D. Sank, K. J. Satzinger, V. Smelyanskiy, K. J. Sung, M. D. Trevithick, A. Vainsencher, B. Villalonga, T. White, Z. J. Yao, P. Yeh, A. Zalcman, H. Neven, and J. M. Martinis, "Quantum supremacy using a programmable superconducting processor," Nature, vol. 574, no. 7779, pp. 505-510, 2019/10/01 2019, doi: 10.1038/s41586-019-1666-5.

[98] U. Fano, "Effects of Configureation Interaction on Intensities and Phase Shifts," Phys. Rev., vol. 124, p. 1866, 1961.

[99] R.-B. Liu and B. F. Zhu, "Adiabatic stabilization of excitons in an intense terahertz laser," Phys. Rev. B, vol. 66, p. 033106, 2002.

[100] J. Černe, A. G. Markelz, M. S. Sherwin, S. J. Allen, M. Sundaram, A. C. Gossard, P. C. van Son and D. Bimberg, "Quenching of excitonic quantum-well photoluminesence by intense far-infrared radiation: Free-carrier heating," Phys. Rev. B, vol. 51, p. 5253, 1995.

[101] J. D. Sau, R. M. Lutchyn, S. Terari and S. Das Sarma, "Generic New Platform for Topological Quantum Computation Using Semiconductor Heterostructures," Phys. Rev. Lett., vol. 104, p. 040502, 2010.

[102] F. Langer, M. Hohenleutner, C. P. Schmid, C. Poellmann, P. Nagler, T. Korn, C. Schüller, M. S. Sherwin, U. Huttner, J. T. Steiner, S. W. Koch, M. Kira and R. Huber, "Lightwave-driven quasiparticle collisions on a subcycle timescale," Nature, vol. 533, pp. 225 - 229, 2016.

[103] S. Schlauderer, C. Lange, S. Baierl, T. Ebnet, C. P. Schmid, D. C. Valovcin, A. K. Zvezdin, A. V. Kimel, R. V. Mikhaylovskiy and R. Huber, "Temporal and spectral fingerprints of ultrafast all-coherent spin switching," Nature, vol. 569, pp. 383 - 387, 2019.

[104] S. Das Sarma, M. Freedman and C. Nayak, "Topologically Protected Qubits from a Possible Non-Abelian Fractional Quantum Hall State," Phys. Rev. Lett., vol. 94, p. 166802, 2005.

[105] L. Fu and C. L. Kane, "Superconducting Proximity Effect and Majorana Fermions at the Surface of a Topological Insulator," Phys. Rev. Lett., vol. 100, p. 096407, 2008.

[106] R. M. Lutchyn, J. D. Sau and S. Das Sarma, "Majorana Fermions and a Topological Phase Transition in Semiconductor-Superconductor Heterostructures," Phys. Rev. Lett., vol. 105, p. 077001, 2010.

[107] Y. A. Bychkov and E. I. Rashba, "Oscillatory Effects and the Magnetic Susceptibility of Carriers in Inversion Layers," J. Phys. C., vol. 17, p. 6039, 1984.

[108] H. Pan and S. Das Sarma, "Physical Mechanisms for zero-bias conductance peaks in Majorana nanowires," Phys. Rev. Research, vol. 2, p. 013377, 2020.

[109] Y. Aharanov and D. Bohm, "Significance of Electromagnetic Potentials in the Quantum Theory," Phys. Rev., vol. 115, pp. 485 - 491, 1959.

[110] M. V. Berry, "Quantal phase factors accompanyting adiabatic changes," Proc. R. Soc. Lond. A, vol. 392, pp. 45 - 57, 1984.

[111] D. Vanderbilt, Berry Phases in Electronic Structure Theory. New York: Cambridge University Press, 2018.

[112] S. D. O'Hara, J. B. Costello, Q. Wu, K. West, L. Pfeiffer and M. S. Sherwin, "Bloch-Wave Interferometry of Driven Quasiparticles in Bulk GaAs," arXiv:2305.1225, 2023.

[113] J. Stensberg, X. Han, S. Lee, S. McGill, J. Paglione, I. Takeuchi, C. L. Kane and L. Wu, "Observation of the Superconducting Proximity Effect from Surface States in SmB6/YB6 Thin Film Heterostructures via Terahertz Spectroscopy," Phys. Rev. Lett., vol. 130, p. 096901, 2023.

[114] P. A. M. Dirac, "The Quantum Thoery of the Electron," Proc. R. Soc. Lond. A, vol. 117, p. 610, 1928.

[115] H. Weyl, "Gravitation and the electron," PNAS, vol. 15, p. 323, 1929.

[116] C. L. Kane and E. J. Mele, "Quantum Spin Hall Effect in Graphene," Phys. Rev. Lett., vol. 95, p. 226801, 2005.

[117] B. A. Bernevig, T. L. Hughes and S. C. Zhang, "Quantum Spin Hall Effect and Topological Phase Tansition in HgTe Quantum Wells," Science, vol. 314, p. 1757, 2006.

[118] N. P. Armitage, E. J. Mele and A. Vishwanath, "Weyl and Dirac semimetals in three-dimensional solids," Rev. Mod Phys., vol. 90, p. 015001, 2018.

[119] K. F. Mak, K. L. McGill, J. Park and P. L. McEuen, "The valley Hall effect in MoS2 transistors," Science, vol. 344, p. 1489, 2014.

[120] Q. Ma*, S.-Y. Xu*, H. Shen*, D. MacNeill, V. Fatemi, T. R. Chang, A. M. Mier Valdivia, S. Wu, Z. Du, C. H. Hsu, S. Fang, Q. D. Gibson, K. Watanabe, T. Taniguchi, R. Cava, E. Kaxiras, H. Z. Lu, H. Lin, L. Fu, N. Gedik, and P. Jarillo-Herrero, "Observantion of the nonlinear Hall effect under time-reversal-symmetric conditions," Nature, vol. 565, p. 337, 2019.

[121] D. J. Thouless, M. Kohmoto, M. P. Nightingale and M. den Nijs, "Quantized Hall Conductance in a Two-Dimensional Periodic Potential," Phys. Rev. Lett., vol. 49, p. 405, 1982.

[122] H. Banks, "Electron-Hole Recollisions in Driven Quantum Wells," Physics, Physics, Univeristy of California, Santa Barbara, 2016.

[123] E. Yablonovitch, T. J. Gmitter, J. P. Harbison and R. Bhat, "Extreme selectivity in the lift-off of epitaxial GaAs films," Appl. Phys. Lett., vol. 51, p. 2222, 1987.

[124] E. Yablonovitch, D. M. Hwang, T. J. Gmitter, L. T. Florez and J. P. Harbison, "Van der Waals bonding of GaAs epitaxial liftoff films onto arbitrary substrates," Appl. Phys. Lett., vol. 56, p. 2419, 1990.

[125] G. D. Cole, W. Zhang, M. J. Martin, J. Ye and M. Aspelmeyer, "Tenfold reduction of Brownian noise in high-relfectivity optical coatings," Nat. Photo., vol. 7, p. 644, 2013.

[126] G. D. Cole, W. Zhang, B. J. Bjork, D. Follman, P. Heu, C. Deutsh, L. Sonderhouse, C. Franz, A. Alexandrovski, O. H. Heckl, J. Ye and M. Aspelmeyer, "Advancements in Substrate-Transferred Crystalline Coatings," Optica, 2016.

[127] R. Cohen, "Come Back, New York, All Is Forgiven," in The New York Times, ed, 2020.

Appendices

In the spirit of the Sherwin group, here is my attempt at a robust addendum to the thesis, geared mostly towards future HSG students hoping to repeat the success and avoid the failures of the past. As such I will detail three key pieces of experimental information, one comical aside, and one more in depth derivation of the theory imbedded in this work.

A. 1 - EXPERIMENTAL SETUP

Nothing of note was added to the optical experimental setup during my PhD. As such, I will only detail *how* we pulse NIR light on our sample, and not get into many of the details, as these are well covered in the theses of Darren Valovcin and Hunter Banks [52, 122]. The diagram of the optical table from [52] is reproduced in Figure A.1.1 as a visual

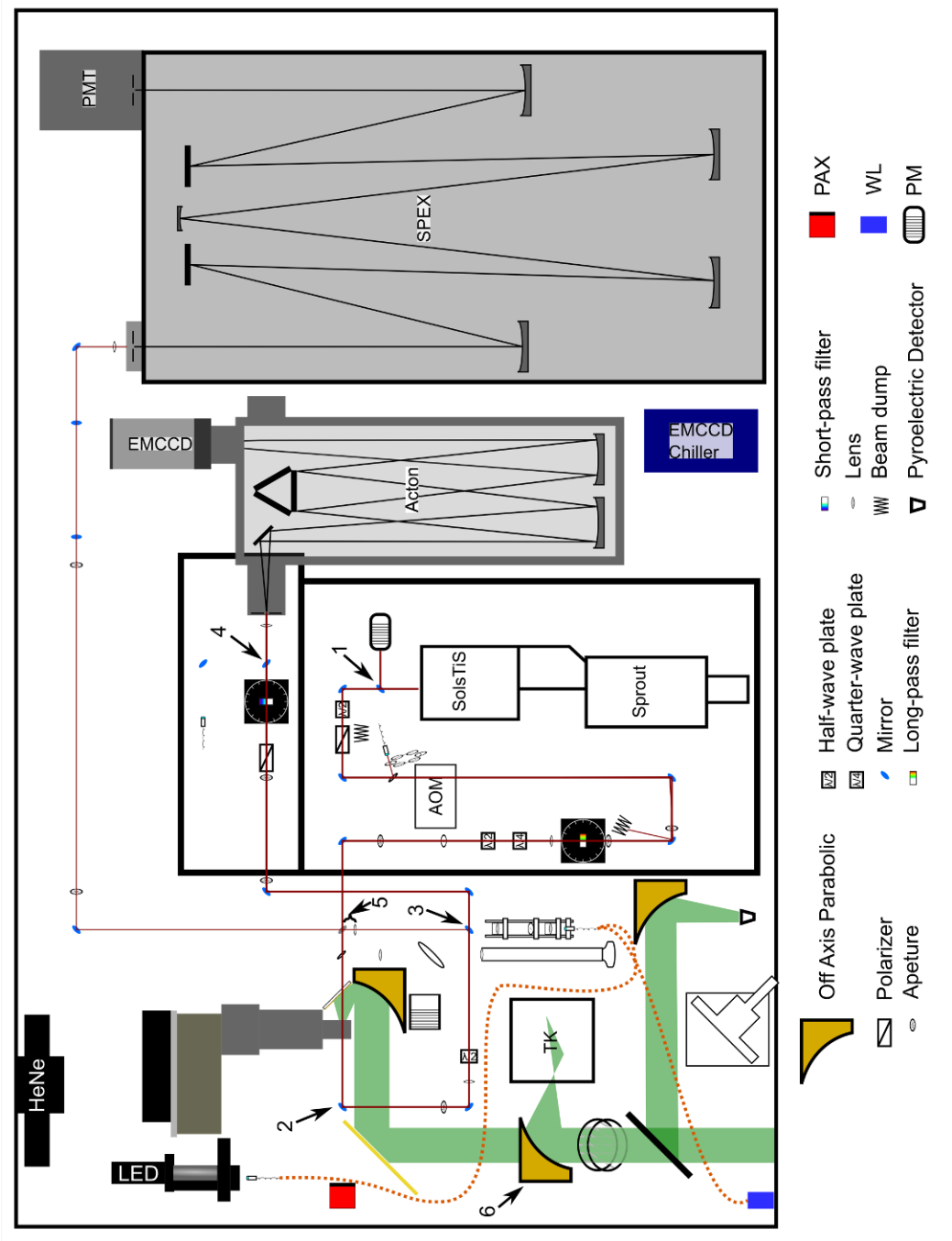

Figure A.1.1 - NIR and THz Optical Table (Reproduced From the Thesis of Daren Valovcin)

A depiction of the components used to co-linearly and simultaneously couple NIR and THz radiation into the sample cryostat and detect the NIR sidebands. The narrow, red beam path are the NIR laser and subsequent sidebands. The wide, green path is the THz field. Components which are detachable and semi-permanent are numbered 1 through 6. This diagram is further detailed in [52].

aid. Then, I will detail a few optical components which should be tuned to maximize the

detected sideband signal in HSG experimentation.

A.1.1 NIR Pulse on Sample

The FEL outputs at a 1.07 Hz repetition rate, so the quasi continuous-wavefront (cw), 40 ns output is incredibly low duty cycle ($\sim 10^{-5}\,\%$). To ensure the NIR is only on the sample when the THz field is also on, we incorporate an Acusto-Optical Modulator (AOM) into our NIR beam path. Given the narrow time domain of the NIR "on time", and the long repetition rate, this is more effective than using a pulsed NIR source.

The NIR radiation is generated by coupling a 7W, 532 nm, cw Sprout YAG pump laser into a Ti:Sapphire (Ti:Sapph) cavity. The M2 SolTiS cavity, modulated by piezoelectric actuators, offers a cw output of NIR radiation with a tunable wavelength. This wavelength is monitored by a wavemeter, which is continuously displaying the measured wavelength, allowing the user to adjust the Ti:Sapph cavity to the proper wavelength at all times. Afterwards, the NIR laser line is sent into the AOM.

The AOM is modulated with a radio frequency pulse, which is turn triggered by a TTL pulse output by a signal generator, which is triggered by the FEL pulse. The TTL pulse is tuned in the time domain to have the NIR on the sample when the THz is present on the sample, determined by a time-resolved measurement of the sideband intensity on the Photomultiplier tube (PMT). The NIR is coupled into the AOM such that the 1st order deflected beam is at its maximum possible power. This 1st order beam is present during modulation and absent when not modulated by the TTL.

The first order beam is then reflected into the rest of the NIR setup, eventually reaching the sample in the cryostat. From here, optics on the table are used to couple NIR sidebands into the PMT and CCD detection mechanisms.

A.1.2 ITO Slide

The THz and NIR beam paths are able to propagate co-linearly onto the sample through the use of an Indium-Tin-Oxide (ITO) slide, which is reflective to THz but transmissive to NIR radiation. In order for sidebands to be generated, the NIR and THz radiation need to be coincident on the same part of the sample. To insure this is the case, the ITO slide is tuned like a mirror, the difficulty being the light which is being reflected is not visible and only on for 40 ns. Other signals must be used to tune the THz alignment onto the sample.

If the ITO slide is gravely misaligned, to the point where the NIR and THz are no longer coincident on one another, detectors which are sensitive to FIR radiation can be used. We often employ a pyrocam, which can detect both NIR and pulsed THz radiation. By triggering the camera with the FEL trigger pulse, the pyrocam can image the THz beam spot after the ITO slide. By greatly attenuating the NIR laser line, the NIR can also be imaged on the pyrocam without damage to the instrument. In this way, the ITO slide can be turned until it is confirmed the THz and NIR are coincident on the sample.

When the ITO slide is well enough aligned as to have the THz and NIR lasers produce sidebands, HSG optical detection can be used as a feedback mechanism. Historically, the measured intensity of the 2nd and 4th order sideband on the PMT were used to fine-tune the ITO slide position. By tuning the tip and tilt of the slide to the

positions which produces the largest signal for these two low order sidebands, the ITO is said to be optimally aligned for experimentation.

Recently, I have incorporated a more finely-tuned method for peaking up the ITO alignment, which incorporates the intensities of higher order sidebands on the CCD. By coupling the sideband photons into the CCD and binning pixels using best practices, a single-shot (1 second) acquisition can be used to better align the ITO slide. By making smaller adjustments to the tip and tilt knobs on the slide's mount, and using the measured intensity of the sideband photons as a feedback mechanism, the THz can be more optimally aligned onto the sample. Shot to shot power fluctuations of the FEL THz output should be taken into consideration when tuning the ITO slide, and many single-shot acquisitions should be observed before the altered ITO position is determined to be better or worse. After this fine-tuned adjustment maximizes the intensity of high-order sidebands, the ITO slide can be said to be maximally aligned.

A.1.3 Snap-out NIR Mirror

When setting the polarization of the NIR laser on the sample using the PAX polarimeter, a mirror is snapped out of a magnetic mount. This is the mirror is labeled #2 in Figure A.1.1. This mirror is not known to repeatedly snap back precisely, which why it is standard practice to peak up the alignment each time it is snapped in and out.

If the mirror snaps back into its mount and appears to be grossly misaligned, iris apertures downstream on the beam path can be used to coarsely align the optic. For finer adjustments, single-shot sideband intensities work best. Because the goal is returning the NIR beam path to its initial alignment, binning should not change in this process.

Additionally, it is mostly the x-position of the NIR and HSG beam path which is altered. Detecting sidebands in the continuous acquisition mode, carefully tune the x-adjustment knob on the mirror mount until the highest intensity of the sideband photons on the CCD are observed.

A.1.4 - Rotating Wiregrid Polarizer

Over the course of time when we collected the data for the experiments discussed in Chapters 4 through 6, I noticed the motor which rotated the wire grid polarizer would sometimes slip. This means the position reading read out on the GUI did not correspond to the actual orientation of the wire grids. Since this is now a known issue, I would recommend the occasional calibration of the wire grids. This is possible in the Instrument Launcher program on the lab PC. The wire grid is rotated from 0 to 90 degrees while the FEL power is measured after the polarizers using the TK meter. The trigonometric function which determines the attenuation of the FEL THz intensity with respect to the polarizer orientation is fit to the measured data. This allows for the zero offset between the motor portion and the true zero position of the polarizer orientation to be determined.

A.2 - CIRCULAR SAMPLE FABRICATION

With the need for samples with a more uniform strain profile, the development of a circular sample fabrication became an important part of the experimental process. Below is a detailed account of such a fabrication.

A.2.1 - Sample Growth

The 500 nm GaAs epilayer used in all the experimentation detailed in this thesis was grown via molecular beam epitaxy at Princeton University. To create a uniform, unbuckled epilayer, a 100 nm lattice-match layer was grown on top of the initial 500 μm GaAs substrate wafer, followed by a 300 nm thick $Al_{0.72}Ga_{0.28}As$ (AlGaAs) etch-stop layer. This etch stop layer will allow for preferential chemistries in the sample fabrication processes, allowing for clearly defined stoping points at different layers of the sample for different etchants. After the etch stop layer, the 500 nm epilayer was grown.

A.2.2 - Sapphire Substrate Preparation

C-axis grown sapphire is a wide band gap material transparent to NIR and THz frequencies, with comparable thermal expansion coefficients to that of bulk GaAs. This makes is a preferable mechanical support for the GaAs epilayer. In addition, a well grown indium tin oxide (ITO) layer will be reflective to THz frequencies and transparent to the NIR frequencies of sidebands. Overall, this allows for a field enhancement of 50% for standing wave frequencies of the ITO/sapphire system. Vector Network Analyzer (VNA) measurements allow for the measurement of these standing waves in the THz domain, allowing for the proper selection of THz frequency out of the FEL.

Prior to deposition, the 488 μm thick sapphire wafer was cleaned using a Turgetol soap solution, followed by the standard Acetone/IPA/DI water solvent clean process. A subsequent descum process with an O2 purge and 200 W UV lamp removed any inorganic matter from the wafer. The wafer was placed in a electron-beam deposition chamber, where a high surface quality, 250 nm thick ITO layer was deposited. By toggling the fluence of the electron beam, the deposition rate was calibrated to the lowest possible value, enabling a good bond between the initial ITO/sapphire interface and increasing the ITO surface quality. A silicon wafer was also in the deposition chamber. Using the Filmetrics proprietary thin film interference experiment, the thickness of the ITO film was determined to be 250 nm. After the deposition, the sheet resistance of the ITO film was measured using the four point probe in the nano fabrication facility. For the sapphire wafer used in experiment, the sheet resistance was 12 Ω per square.

Due to the impedance differences between the sapphire/ITO/vacuum interfaces, there are significant Fabry-Pérot oscillations in the NIR range. To create a buffer between the low impedance ITO film and the ambient impedance of the vacuum, a SiO_2 anti-reflection coating was grown on top of the ITO using electron beam deposition. The deposited SiO_2 had a thickness of 150 nm, again measured on a reference silicon wafer using the Filmetrics tool. With both films deposited on the sapphire wafer, the substrate was diced into 10 mm X 7 mm rectangles for individual sample fabrication using the dicing saw at the UCSB nano fabrication facility.

A.2.3 - Circular Mesa Etch

The GaAs wafer was cleaved into subsamples close to 10 mm x 10 mm in size. The flat edge referencing the [100] crystal axes was continued onto these subsamples by marking the back end of the subsample with an X|, with the flat line in the direction of the flat edge. This orientation was noted throughout the sample fabrication process, as it provides the THz-to-crystal axis orientation for HSG experimentation.

A properly sized and marked subsample was then prepared for the circular mesa etch, first by solvent cleaning the side of the wafer with the GaAs epilayer. Differential microscope images were taken to insure to organic or inorganic matter was present after the solvent clean/descum.

Negative photoresist was spin-coated onto the epilayer side of the subsample. Using a 7 mm inner-diameter washer as a mask, the photoresist was flood exposed with UV light, with the inner-diameter defining the future mesa structure of the epilayer. The exposed resist was then heated for an additional minute, and again flood exposed (without the washer). The photoresist was developed, leaving behind a circular mesa pattern.

The subsample was then dipped into a $H_3PO_4/H_2O_2/H_2O$ (1:1:1) solution for 45 seconds. This etch works fast. In the 45 seconds the sample is submerged in the solution, the etchants work through all 500 nm of the epilayer, the AlGaAs etch stop layer, the lattice match layer, and some of the GaAs substrate. Using confocal microscopy measurements, the height of the mesa was measured to consistently be 6.5 - 7 μm. An image of this mesa etched sample is depicted in Fig A.2.1. Because the final sample

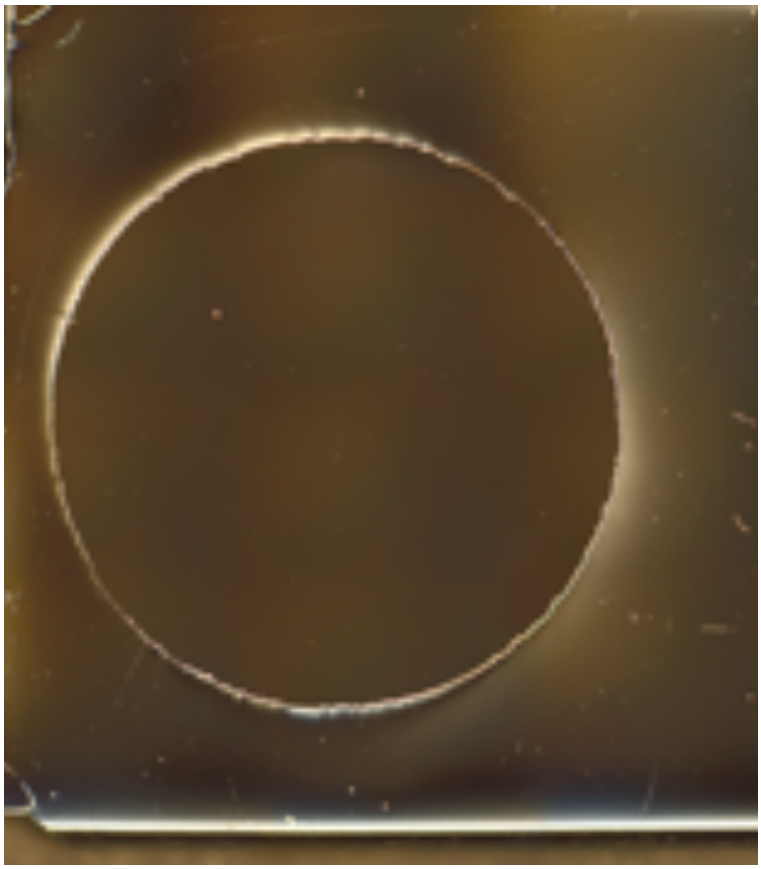

Figure A.2.1 - Circular Mesa Etch Epilayer
The sample and Epi-layer after the circular mesa etch process. The 7mm diameter mesa in the center has a height of ~ 7 μm. Taken with the Differential contrast microscope in the UCSB nano fab.

thickness is completely determined by the epilayer, the only important feature of the mesa is the height being greater than 0.5 μm. The fast etch rate preferentially along the [100] direction minimizes the undercutting of the photoresist, leading to a well defined circular pattern after the photoresist is removed by solvents.

A.2.4 - Epilayer Back Etch

With a well defined circular mesa, the back end of the wafer was removed from a modified process detailed in other theses and papers [63, 76, 123-126]. Apiezon Wax W (colloquially called Black Wax) was applied to the epilayer mesa to protect the layer

while the GaAs substrate and AlGaAs layers were removed via chemical etching. The sample and black wax were mechanically supported and handled using a combination of a plastic dipper stick, a plastic vacuum O-ring component, and maximum tackiness Gel-Pak slips. Most of the GaAs substrate was removed by dipping the sample in the etchant solution H_2O_2/NH_4OH (10:1) for 50 minutes. After the faster etchant, the more dilute H_2O_2/NH_4OH (30:1) solution was used to etch away the remaining GaAs substrate. The more dilute solution preferentially etches the GaAs substrate compared to the AlGaAs etch stop layer.

After about 50 minutes to one hour in the slower etchant, an interference pattern is present on the sample, which is a Newton ring effect between the thin AlGaAs/GaAs epilayer interface. When the entire sample takes on this appearance, the sample is done with the slower etchant and ready for the removal of the etch stop layer using 49% HF. After a total of one minute submerged in the HF, only the 500 nm GaAs epilayer should remain, and the sample is ready for a van-der-Waals (VDW) bond.

A.2.5 - Van-Der-Waals Bond

In parallel with the GaAs epilayer preparation, the diced sapphire substrate was solvent cleaned and descumed for the VDW bonding process. The sapphire was on top of a Berkshire fiberless tip to maintain cleanliness throughout the cleaning process. After the sapphire was cleaned and the GaAs sample completely backside etched, the two were gently pushed into contact, beginning the VDW bond process. The sample was left overnight in a vented fume hood to minimize particle contamination and allow the bond more time to form.

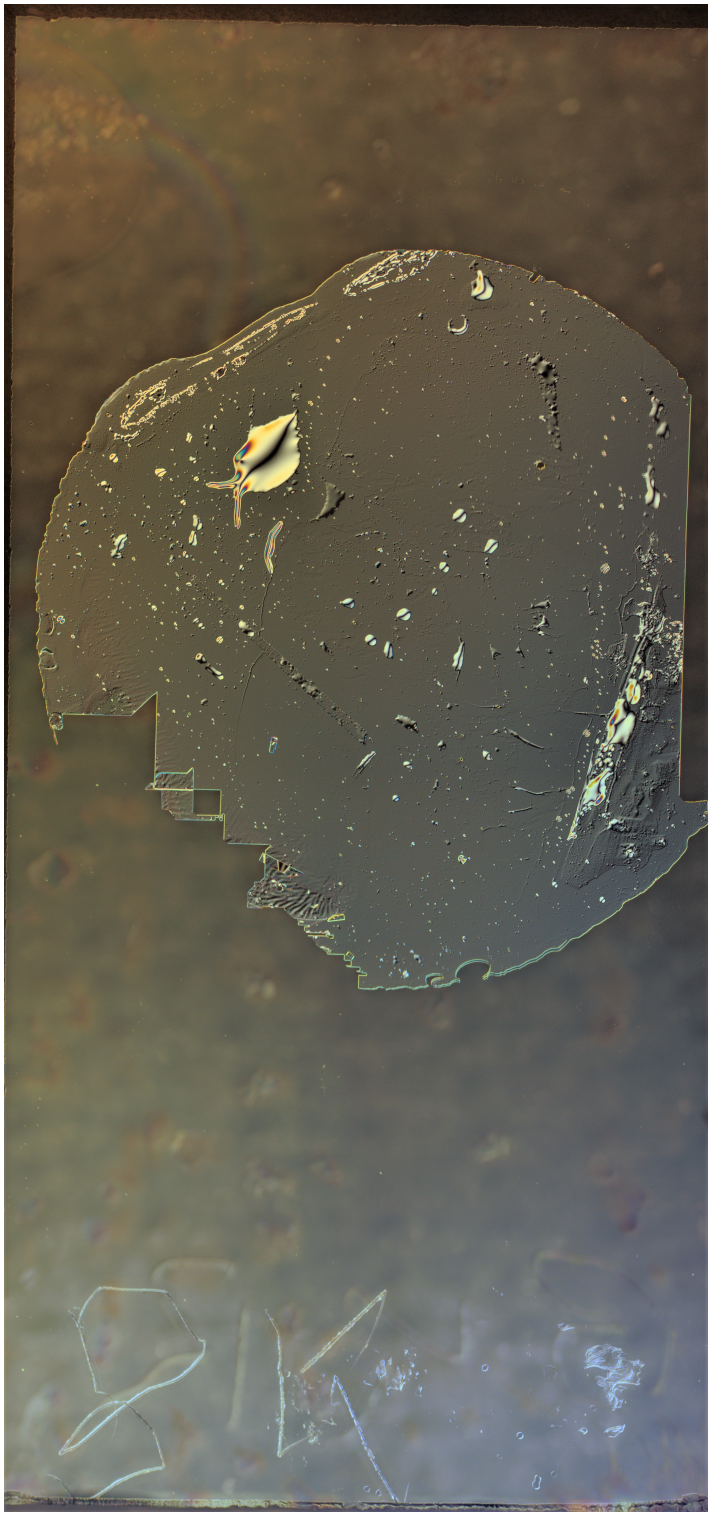

Figure A.2.2 - Final Sample After VdW Bond
The epi-layer bonded to the sapphire substrate. The ITO orientation is indicated by the markings on the bottom left. For scale, the width of the sapphire is 7mm and the height is 15 mm. This was the sample used for data in Chapter 2.

After the overnight bond, the Black Wax is relaxed by heating it up to a temperature close to, but below it's melting point, allowing the whole epilayer to bond with the sapphire. When the sample has cooled down to room temperature, the Black Wax is removed using chloroform. The sample was gently scrubbed clean using solvents and O_2 descummed before being brought out of the nano fabrication facility. Figure A.2.2 shows an example of final sample.

A.3. - THE FEL SAGA

In the summer of 2019, major repairs were required to get the FEL lasing again. Along with scheduled maintenance to components in the accelerator tank, attempts were made to repair the folding mirror for the cavity dump mode of the FEL. This mirror folds in and out of the THz beam path. When it is out of the way, it allows for the THz to couple out of the beam line through a mirror with a hole in a center of it. This is called the "hole coupler" mode, which produces low power, long duration (~μs) THz pulses.

When the mirror is in the path of THz propagation, it forms a node in a "J"-looking cavity. This cavity reflects the THz radiation generated by the FEL back and forth until the THz is dumped out by the triggering of a Silicon mirror by a flash of green laser light. In the "cavity dump" mode, the FEL produces high power, 40 ns pulses of cw THz radiation, a truly unique source of light. In order for the FEL to laze in this mode, the folding mirror needs to be well positioned in order to reflect THz light in the cavity.

Through decades of use, and, in my mind, the incorporation of overpowered nematic actuators, the folding mirror was taken off it's axis of rotation, meaning the FEL would not laze in the cavity dump mode. Aligning a THz optics component is never easy. The problem gets more difficult when the THz is only on when a source of radiation is active, as is the FEL accelerator. The problem becomes near impossible when the component which needs adjusting is located in high vacuum, sandwiched between two parts of a THz waveguide which are welded together. Fortunately for the powers that be at the ITST, getting this component to work was essential to taking data which was essential to my nascent scientific career, so we found a solution.

A.3.1 - I Forgive You FEL

Shortly after the resolution of the FEL saga, we were hit with the COVID 19 pandemic. Rattled by the sudden shut down of New York City in the early stages of the virus, a New York Times writer wrote a love letter to the City [127], a plea for the return of the bustling metropolis he had taken for granted for too long. Inspired by his work, I composed something similar for the FEL, as it laying dormant for months gave me a newfound appreciation for the machine. Before going into the details of the repair, here is my poem:

I forgive you, FEL.
I forgive you your groan when we first turn on the Pels,
Your dying breaths after a long day.
Like a racehorse many years past its prime
I forgive you your temperamental fits and starts.
I forgive you your day-to-day inconsistencies.

All is forgiven if you will only return:
The pump that has broken in the OTS,
The blown-out capacitors and resistors,
Jerry's slap box, with it's connections dangling in free space,
The tank filled with SF6
The hum of pumps and chain in the vault,

A hum I thought would never cease,

Until it did.

I forgive you. I forgive you now and forever.

How could I ever begrudge your homemade style,

Your rag-tag manner,

Your ad-hoc solutions,

Your perfect imperfections and your comical flaws,

When I known all along your great strength was your unconventionality?

A mirror of the scientists and engineers who have lovingly assembled and disassembled you throughout the years.

Only come back and all is pardoned:

The clutter of room B,

The damp air in the OTS,

The South West GVM we can't access without climbing on pipes,

The 500 mW green alignment laser which is always on,

The folding mirror which, like the rest of you, is good enough to work,

But broken enough to drive us crazy.

I forgive you the Lab View program,

The planned obsolescence of National Instruments components,

And Field Point requiring us to run Windows XP,

The fact we can't load a new file without restarting the computer.

I forgive you Steering Coil S57, which is wired in reverse of all the other coils,

The filament, which turns up to 11.

The filament, which is probably dying because we turn it up to 11.

I forgive you the broken dipole power supply,

The helical undulatory which is always a few months away from lasing

The arc, which stops my hear

I forgive you the way you persuade scientists starting an experiment at 5pm is OK behavior

Please, do not be proud.

I know, we curved you with irresponsible abandon.

Please forgive us, as I forgive you.

We took you too much for granted.

Yes, forgive us for not giving daily praise for the miracle of the FEL.

I know I did not thank you enough for the light you produce

And the science you enable

I don't treat you as the marvel you are,

How there is nothing else in the world lie you

How we can see Sidebands

Frankly, too many sidebands,

Because of all you can do.

I did not thank you enough for the way you make me feel,

When I walk in the vault and think this is *lab*,

Allowing us to do science no one else can do.

Being a young scientist, I was in an hurry.

I was forgetful.

You get that.

Please forgive me.

Please forgive us all.

I'll throw in Brad's eraser shavings.

Forgive you for every one of Brad's eraser shavings on the collaboration table.

And his unfinished coffee.

Just come back, just return, please. I know we can make a deal.

A.3.2 - Aligning the Folding Mirror

Like any other laser, the onset of lasing will occur when the gain in the cavity is greater than the losses [cite Eberly]. For the FEL, the optical gain is determined by the ability for the free electron beam to generate THz radiation, and for optical elements in the cavity to reflect THz radiation such that collective, coherent modes of radiation

dominate, producing laser-like THz output. The loss is determined by the amount of radiation coupled out of the cavity on a relative time-scale.

When you have one of three optical elements misaligned, rather grossly, you will not have any gain to brag about. Put plainly, your cavity will not lase. No THz for you. When Joe and I first encountered these problems, Darren was incredulous, thinking certainly the new graduate students had forgotten to do some obvious thing, preventing lasing in the cavity. While Joe and I were certainly green FEL tuners, his blame quickly redirected when he moved the folding mirror in and out of the cavity dump mode and felt the mirror drag against the wave guide.

After much consternation and dismissal, we all eventually determined the cavity mirror was misaligned, grossly, and serious repairs were in order to allow this high power mode of FEL operation to lase again. Highly-engineered operations with the goal of re-adjusting the folding mirror into place produced little improvement. Witnessing the despair and fatigue brought on by the faulty folding mirror, our long-in-the-teeth FEL virtuoso Dave one day became determined to put us out of our misery. Walking over to the folding mirror, with a (albeit poorly aligned) alignment laser Dave ball parked by eye where the laser should be, based on his know how. From there, we were able to get the FEL to lase.

A.3.3 - Lasing At 240 GHz

With the cavity dump mirror properly placed, we had enough gain in our cavity to tune the FEL at a lower energy mode. For reasons beyond the scope of this thesis, the millimeter FEL (MM FEL) has the highest gain when generating THz in the 240 GHz

range. Therefore, getting the 240 GHz (or 8 cm^{-1}, read *wavenumber*) mode operating was the easiest and first priority. Additionally, the silicon slab in the THz beam path is known to deflect the beam, reducing the gain in the cavity by misaligning the cavity mirrors. To counteract that deflection, we removed the Si slab from the cavity arm, meaning we had no method of out coupling the THz. Instead, we would rely on the characteristic bump in the electron beam recirculation signal.

After approximately one week of tuning, we were able to get the FEL to lase at 240 GHz with no Si inserted. This process involved fine tuning the FEL beam to maximize recirculation. Given the lower beam energy, Coulomb interaction between different free electrons spreads out the beam compared to higher frequency operation. This makes running longer e-beam pulses more difficult at 240 GHz, which is normally not necessary, given the high gain of the cavity at this wavenumber. However, when cavity components need to be tuned in order to induce lasing, this becomes a necessary but difficult process.

With the cavity lasing at 8 cm^{-1}, we had the gross alignment of the folding mirror and two end mirrors basically fixed. By making fine adjustments, and determining if such adjustments pushed up the lasing time, we could fine tune the mirror positions. However, the Si slab produces and observable deflection to the THz beam path, so fine adjustments are negated and thus not necessary at this point in the process. By reintroducing the Si slab into the cavity, we were preparing the cavity dump mode of the FEL to couple out THz again.

Introducing the slab initially destroyed the lasing process in the cavity. The pulse width was increased again, and we worked through different components to regain lasing. By adjusting through the parameter space in the following order, we were able maximize the gain of the cavity at 8 cm^{-1}:

Coarse adjustment of cavity end-mirrors — Due to the deflection induced but the Si slab, the end mirrors needed to be coarsely adjusted in order to regain lasing. After each coarse adjustment, we let multiple e-beam pulses run through the FEL to make sure poor pulses were not interfering with our cavity tuning.

The position of the end mirrors are measured through two trim-pots, which measures the rotation of knobs determining the x and y deflection of the component. During the process of tuning, we realized the voltage reported on the NI interface was not the correct value. Instead of relying on this measurement, best practice is using a multimeter to measure the voltage from ground to the tuning potential of each trim-pot, which has been determined to be repeatable. As a failsafe, a caliper can also be used to measure the mechanical deflection, set by the two knobs. At the end of the day of FEL operation, if lasing was induced, these values should be recorded, along with the frequency of operation. The next time the FEL is run at that frequency, the user should insure the cavity end-mirrors are at these positions before starting FEL tuning.

Fine adjustment of end mirrors and folding mirror — After coarse adjustments induce lasing at the earliest possible time, finer adjustments of both the cavity end mirrors and the folding mirror can be made to have the largest gain,

measured by the time of lasing onset. The folding mirror has been adjusted in the past through a DC voltage applied to an actuator attached to the mirror, with an RV rearview camera used to view the tuning in real time. The position of the folding mirror is read out by a micrometer, displayed in Figure A.3.1. Given the delicate alignment of this component, such precision is required to not damage component and preserve all the alignments done to date.

Adjustment of the free-electron beam path — As always, tuning the alignment and focus of the free-electrons into the FEL cavity can increase the gain. With the more coarse adjustments having established lasing in the cavity, it is worthwhile to occasionally revisit the beam tuning and insure the gain is maximized.

Adjustment of the Si position — The silicon angle can fine-tune the alignment of the THz in the cavity, and will determine the power coupled out when the cavity is dumped. When all of the other components are properly tuned, this angle should be adjusted, using LabVIEW, to maximize the parameters stated above.

By working through this parameter space, we were able to get the FEL to operating in the Cavity Dump mode at 8 cm^{-1}. With this in order, tuning at higher frequencies was the next goal.

A.3.4 - Lasing At 450 GHz

The THz field generated by the FEL at higher energies of operation are more narrow in profile, for reasons beyond this thesis. This narrower profile requires finer tuning in order to induce lasing for the higher frequency modes of operation. Normally,

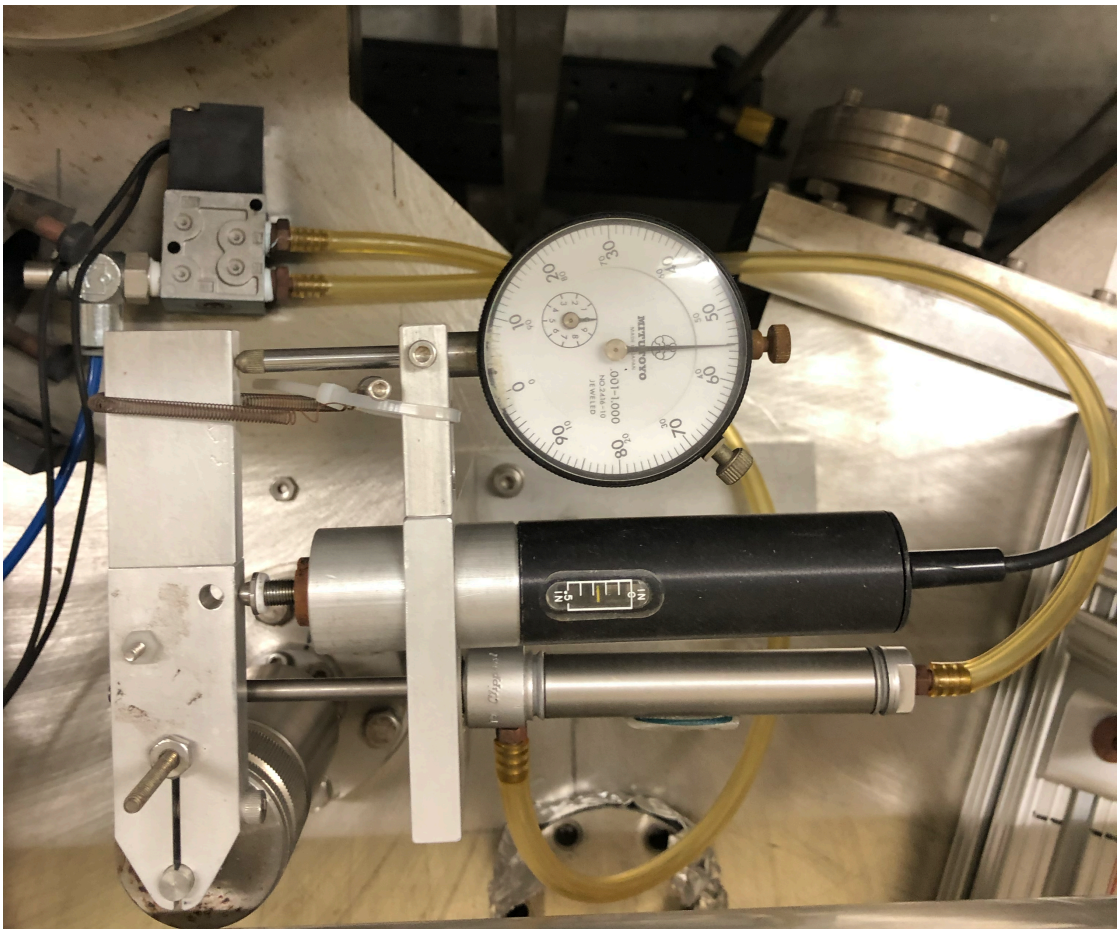

Figure A.3.1 - Micrometer and Actuator Manipulating Folding Mirror Position
The actuator at the bottom of this image can flip the folding mirror in and out of position to switch between hole-coupling and cavity dump mode. The black cylinder is a voltage controlled screw which can finely adjust the folding mirror position, which is read out by the micrometer at the top of the image.

this includes running the FEL at longer e-beam pulses and tuning the parameter space outlined in the previous section.

At the current mode of operation, it would appear the e-beam needs to be slightly misaligned going into the undulator in order to induce lasing. When tuning the beam through the beam line initially, at e-beam pulse widths of ~2 μsec, e-beam recirculation can be tuned to greater than 95%, which is historically a good value, and more than sufficient for long-term operation. However, as the pulse width is increased beyond the

times where lasing is expected to occur (8 - 10 μsec) there is no characteristic bump in the recirculation curve on the CP measurement. In order to induce lasing, the e-beam needs to be deflected from the optimal alignment, which we historically do by adjusting the y-deflection on one of first three steering coils with one large click in the negative direction. Only one (sometimes two) should be necessary to induce lasing. If more are required, there may be other cavity parameters which are not optimized, or further downstream e-beam alignment is compromised.

A.3.5 - Failed Attempt at 540 GHz

Operating at a frequency with lower gain in the MM FEL like 540 GHz required some creativity. Even at normal operation, this mode could be difficult to maintain given the large electrostatic potential of the accelerator (4.6 MV) and long e-beam widths required for lasing (~6 μsec). With the misaligned folding mirror, this frequency proved extra difficult. When pulse widths on the order of 20 μsec did not induce lasing, Gerry recommended using a higher beam current, as this would also correspond to higher gain in the cavity. In the same way we think of the current in a wire being proportional to the electron density in a conductor, so too the beam current in the FEL is related to the number of free electrons in the pulse. Through modulating mechanisms in the accelerator beyond the scope of this thesis, the LabVIEW program can tune the beam current for a given FEL pulse.

With a larger beam current, the electrostatics in the accelerator become more unreliable. With more electrons in a pulse, the beam is inherently larger due to Coulomb

repulsion of the electrons. These two factors make tuning at a higher beam current more difficult; you don't get the extra gain for free.

After one day tuning at 1.5 Amps of beam current, we sent through a 1.5 cycle e-beam pulse with the best circulation we could achieve. The FEL arced in a way we've never heard, putting the fear of God in all involved. We shut down the FEL, never to try the high current mode of operation again.

A.3.6 - Maximizing Output THz Power Into Lab Rooms.

Even with the FEL lasing in the cavity dump mode, we were still not receiving maximum power in the lab rooms. Working backwards, we intuited this is because the misaligned folding mirror was sending the THz through a new beam path once it was coupled out of the cavity. Fortunately, there is an elliptical mirror after the switched Si which can adjust the beam path. Unfortunately, the mirror is located in the vault, meaning coarse, discrete adjustments are all that is possible. We did notice rotations no larger than a quarter to a half of a rotation of the knobs produced measurable increases or decreases in power detected in the user labs. With an hour of tuning these optical elements, we were able to introduce THz fields into the lab space which were on par with historical values at the respective modes of operation.

A.3.7 - Switching Between Modes of Operation

As mentioned before, the LavVIEW program has a faulty readout voltage of potentiometers controlling the motion of various elements in the cavity. Given the low gain of the cavity at its current mode of operation, confirming these elements are in the right position manually before switching over to a new frequency of operation is

essential. At the very least, it confirms the cavity is set in a position which is historically lasing, and is not the cause of any issues experienced.

It is worth mentioning that the EPR experiment which often runs the 8 cm^{-1} mode has a different desired FEL THz output, compared to the HSG experiment which often runs the 15 cm^{-1} mode. As a result, switching between frequencies of operation often involves a significant repositioning of the Si.

A.4 - MAKING A GOOD CUP OF COFFEE IN LAB

For reasons beyond my understanding, making a decent cup of coffee escapes the capabilities of some of my lovely lab mates. For future generations of ITST scientists, I am leaving behind a few straightforward rules which will produce a good cup of coffee in a typical Mr.-Coffee-style maker.

It starts with the beans — The ceiling on your cup of coffee is normally set by the quality of beans you use to make your cup. Making a pot with Albertson's store brand is never going to be as good as one made with locally roasted beans.

Measure out the beans — Even though it takes only 20 seconds, and we are experimental physicists governed by empirical measurements, the act of measuring out the proper volume of beans is too much for some of my colleagues. I shouldn't be too critical, as any coffee snob would tell you weight is a better determinant of the right amount of grounds for a pot of coffee. I default to volume as there is no conveniently accessible scale in lab with the proper tolerance for grams of coffee beans.

Fully ground the beans — Again, even though it only takes 20 -30 seconds, have the electrical grinder fully ground all of the beans. When a physicists, or engineer, does not take the time to ensure all the beans are ground, the coffee comes out significantly weaker as the exposed surface area for caffeine extraction is greatly reduced. You will know when all the beans are ground by a change in pitch of the mechanical whirling sounds of the grinder. For those keeping score at home, the

extra 40-60 seconds taken by the coffee maker greatly enhances the experiences of the whole lab group, setting the tone for the morning and the day to come.

8 oz. to 10 oz. Ratio — For every 8 fluidic ounces of water, include 10 fluidic ounces of unground beans. This should provide a strong but balanced coffee, if this and the previous steps are followed.

Best of luck.

A.5 DERIVATION OF SIDEBAND POLARIZATION FROM HOLE-SPECIES BASIS

In this section, starting from the LIT expression for ς_n^ν, the expected Jones matrix elements and sideband polarization are calculated. Given the analytical nature of the LIT approximation, this provides lines of inquiry for dependence on experimental and material parameters.

A.5.1 Hole Basis Propagator as an Oscillating Wave

By expressing the propagator ς_n^ν as a complex exponential, the interference between the hh and lh states becomes more clear, and there are less variables to carry around in each expression, simplifying expressions. Starting with Eq. 4.12 and 13

$$\varsigma_n^\nu \propto e^{i\Theta_\nu(n)} e^{-\Gamma_d \tau_{n,\nu}\hbar^{-1}} \tag{A.1}$$

Here

$$\begin{aligned}\Theta_\nu(n) &\equiv n\omega t_{f,n,\nu} + A_{n,\nu} + \Delta_{NIR}\tau_{n,\nu}\hbar^{-1} \\ &= \left(8n/15 + \Delta_{NIR}/\hbar\omega\right)\sqrt{3}(2nE_{\gamma THz}/U_{p,\nu})^{1/4}\end{aligned} \tag{A.2}$$

A.5.2 LIT Approximated Jones Matrix Elements

We can express the expected Jones Matrix elements in the circular basis, following Eq. 3.14

$$\begin{aligned}T_{++,n} = T_{--,n} &\propto \frac{2+n_z}{3} e^{i\Theta_{hh}(n)} e^{-\Gamma_d \tau_{n,hh}\hbar^{-1}} + \frac{2-n_z}{3} e^{i\Theta_{lh}(n)} e^{-\Gamma_d \tau_{n,lh}\hbar^{-1}} \\ T_{+-,n} &\propto \frac{n_x + i n_y}{\sqrt{3}} \left(e^{i\Theta_{hh}(n)} e^{-\Gamma_d \tau_{n,hh}\hbar^{-1}} - e^{i\Theta_{lh}(n)} e^{-\Gamma_d \tau_{n,lh}\hbar^{-1}} \right)\end{aligned} \tag{A.3}$$

$$T_{+-,n} \propto \frac{n_x - in_y}{\sqrt{3}} \left(e^{i\Theta_{hh}(n)} e^{-\Gamma_d \tau_{n,hh} \hbar^{-1}} - e^{i\Theta_{lh}(n)} e^{-\Gamma_d \tau_{n,lh} \hbar^{-1}} \right)$$

From this, we can look at the Jones matrix expression, using the circular basis we utilized in Chapter 4, to express the expected $r^2(n), l^2(n), \& \phi(n)$ in terms of these LIT approximated propagators. Starting with Eq 4.4

$$\begin{pmatrix} r(n)e^{i\phi_r(n)} \\ l(n)e^{i\phi_l(n)} \end{pmatrix} = \begin{pmatrix} T_{++,n} & T_{+-,n} \\ T_{-+,n} & T_{--,n} \end{pmatrix} \begin{pmatrix} r_{NIR} \\ l_{NIR}e^{i\phi_{NIR}} \end{pmatrix} \tag{A.4}$$

We can express the two circular components of the sideband electric field as

$$r(n)e^{i\phi_r(n)} = T_{++,n} r_{NIR} + T_{+-,n} l_{NIR} e^{i\phi_{NIR}} \tag{A.5}$$

$$\begin{aligned} r(n)e^{i\phi_r(n)} \propto & \left[\frac{2 + n_z}{3} e^{i\Theta_{hh}(n)} e^{-\Gamma_d \tau_{n,hh} \hbar^{-1}} + \frac{2 - n_z}{3} e^{i\Theta_{lh}(n)} e^{-\Gamma_d \tau_{n,lh} \hbar^{-1}} \right] r_{NIR} + \\ & \left[\frac{n_x + in_y}{\sqrt{3}} \left(e^{i\Theta_{hh}(n)} e^{-\Gamma_d \tau_{n,hh} \hbar^{-1}} - e^{i\Theta_{lh}(n)} e^{-\Gamma_d \tau_{n,lh} \hbar^{-1}} \right) \right] l_{NIR} e^{i\phi_{NIR}} \end{aligned} \tag{A.6}$$

and

$$l(n)e^{i\phi_l(n)} = T_{-+,n} r_{NIR} + T_{--,n} l_{NIR} e^{i\phi_{NIR}} \tag{A.7}$$

$$\begin{aligned} l(n)e^{i\phi_l(n)} \propto & \left[\frac{n_x - in_y}{\sqrt{3}} \left(e^{i\Theta_{hh}(n)} e^{-\Gamma_d \tau_{n,hh} \hbar^{-1}} - e^{i\Theta_{lh}(n)} e^{-\Gamma_d \tau_{n,lh} \hbar^{-1}} \right) \right] r_{NIR} \\ & \left[\frac{2 + n_z}{3} e^{i\Theta_{hh}(n)} e^{-\Gamma_d \tau_{n,hh} \hbar^{-1}} + \frac{2 - n_z}{3} e^{i\Theta_{lh}(n)} e^{-\Gamma_d \tau_{n,lh} \hbar^{-1}} \right] l_{NIR} e^{i\phi_{NIR}} \end{aligned} \tag{A.8}$$

A.5.3 Expected Sideband Polarization States

With these expressions, we can derive the expressions for $r^2(n), l^2(n), \& \phi(n)$

$$
\begin{aligned}
r^2(n) &= |\, r(n)e^{i\phi_r(n)}\,|^2 \\
l^2(n) &= |\, l(n)e^{i\phi_l(n)}\,|^2 \\
\phi(n) &= \mathrm{Arg}\left(r(n)e^{i\phi_r(n)}\right) - \mathrm{Arg}\left(l(n)e^{i\phi_l(n)}\right) \\
&= \phi_r(n) - \phi_l(n)
\end{aligned}
\tag{A.9}
$$

From this representation, and Eqs. A.1,6, and 8, we can calculate the expected polarization states often sidebands. As an exercise, we can work through the algebra to an explicit expression for the right handed polarization for the sideband field, to learn more about why the sideband polarization changes in terms of the phase of the quasiparticle propagator.

$$
\begin{aligned}
r^2(n) \propto |\frac{1}{3}\left[\left(2+n_z\right) r_{NIR} + \left(\sqrt{3}n_x + i\sqrt{3}n_y\right) l_{NIR}e^{i\phi_{NIR}}\right] e^{i\Theta_{hh}(n)}e^{-\Gamma_d\tau_{n,hh}\hbar^{-1}} \\
+\frac{1}{3}\left[\left(2-n_z\right) r_{NIR} - \left(\sqrt{3}n_x + i\sqrt{3}n_y\right) l_{NIR}e^{i\phi_{NIR}}\right] e^{i\Theta_{lh}(n)}e^{-\Gamma_d\tau_{n,lh}\hbar^{-1}}\,|^2
\end{aligned}
\tag{A.10}
$$

Which can be represented as

$$
r^2(n) \propto \left|\left(a_r + ic_r\right)e^{i\Theta_{hh}(n)} + \left(b_r + id_r\right)e^{i\Theta_{lh}(n)}\right|^2
\tag{A.11}
$$

Where

$$
\begin{aligned}
a_r &= \frac{1}{3}\left[\left(2+n_z\right) r_{NIR} + \sqrt{3}\left(n_x\cos\phi_{NIR} - n_y\sin\phi_{NIR}\right) l_{NIR}\right] e^{-\Gamma\tau_{n,hh}\hbar^{-1}} \\
b_r &= \frac{1}{3}\left[\left(2-n_z\right) r_{NIR} - \sqrt{3}\left(n_x\cos\phi_{NIR} - n_y\sin\phi_{NIR}\right) l_{NIR}\right] e^{-\Gamma\tau_{n,lh}\hbar^{-1}} \\
c_r &= \frac{1}{3}\left[\sqrt{3}\left(n_y\cos\phi_{NIR} + n_x\sin\phi_{NIR}\right) l_{NIR}\right] e^{-\Gamma\tau_{n,hh}\hbar^{-1}} \\
d_r &= -\frac{1}{3}\left[\sqrt{3}\left(n_y\cos\phi_{NIR} + n_x\sin\phi_{NIR}\right) l_{NIR}\right] e^{-\Gamma\tau_{n,lh}\hbar^{-1}}
\end{aligned}
\tag{A.12}
$$

Allowing us to express the polarization as

$$r^2(n) \propto a_r^2 + b_r^2 + c_r^2 + d_r^2 + 2(a_r b_r + c_r d_r)\cos\left(\Theta_{hh}(n) - \Theta_{lh}(n)\right) + 2(a_r d_r - b_r c_r)\sin\left(\Theta_{hh}(n) - \Theta_{lh}(n)\right) \tag{A.13}$$

Which can be expressed as

$$
\begin{aligned}
& r^2(n) \propto \\
& \frac{1}{9} e^{-2\Gamma_d \tau_{n,hh} \hbar^{-1}} \cdot \\
& \left[\left(4 + 4n_z + n_z^2\right) r_{NIR}^2 + 4\sqrt{3} \left(2n_x \cos\phi_{NIR} - 2n_y \sin\phi_{NIR} + n_z n_x \cos\phi_{NIR} + n_z n_y \sin\phi_{NIR}\right) r_{NIR} l_{NIR} + 3\left(n_x^2 + n_y^2\right) l_{NIR}^2 \right] \\
& + \frac{1}{9} e^{-2\Gamma_d \tau_{n,lh} \hbar^{-1}} \cdot \\
& \left[\left(4 - 4n_z + n_z^2\right) r_{NIR}^2 - 4\sqrt{3} \left(2n_x \cos\phi_{NIR} - 2n_y \sin\phi_{NIR} - n_z n_x \cos\phi_{NIR} + n_z n_y \sin\phi_{NIR}\right) r_{NIR} l_{NIR} + 3\left(n_x^2 + n_y^2\right) l_{NIR}^2 \right] \\
& + \frac{1}{9} e^{-\Gamma_d (\tau_{n,hh} + \tau_{n,lh}) \hbar^{-1}} \cdot \\
& \left[\left(4 - n_z^2\right) r_{NIR}^2 + 4\sqrt{3} \left(n_x n_z \cos\phi_{NIR} - n_y n_z \sin\phi_{NIR}\right) r_{NIR} l_{NIR} - 3\left(n_x^2 + n_y^2\right) l_{NIR}^2 \right] \cos\left(\Theta_{hh}(n) - \Theta_{lh}(n)\right) \\
& + \frac{1}{9} e^{-\Gamma_d (\tau_{n,hh} + \tau_{n,lh}) \hbar^{-1}} \cdot \\
& \left[4\sqrt{3} \left(n_y \cos\phi_{NIR} + n_x \sin\phi NIR\right) r_{NIR} l_{NIR} \right] \sin\left(\Theta h\, h(n) - \Theta_{lh}(n)\right)
\end{aligned}
\tag{A.14}
$$

There are two limits where this expression is greatly simplified. The first is not possible given the physics of quasiparticles in bulk GaAs, $\tau_{n,hh} = \tau_{n,lh}$, but in the limit of $\tau_{n,lh} \approx \tau_{n,hh}$, we can learn more about the structure of this equation, which takes the form

$$
\begin{aligned}
r^2(n) \propto & \frac{1}{9} e^{-2\Gamma_d \tau \hbar^{-1}} \cdot \\
& \left[\left(8 + 2n_z^2\right) + \left(8 - 2n_z^2\right) \cos\left(\Theta_{hh}(n) - \Theta_{hh}(n)\right) \right] r_{NIR}^2 \\
& + \left[3\left(n_x^2 + n_y^2\right) \left(1 - \cos\left(\Theta_{hh}(n) - \Theta_{hh}(n)\right)\right) \right] l_{NIR}^2 \\
& + \left[4\sqrt{3} \left((1 - n_z) n_y \sin\phi_{NIR} + (1 + n_z) n_x \cos\phi_{NIR} \right) \cdot \right. \\
& \left. \left(\cos\left(\Theta_{hh}(n) - \Theta_{hh}(n)\right) + \sin\left(\Theta_{hh}(n) - \Theta_{hh}(n)\right) \right) \right] r_{NIR} l_{NIR}
\end{aligned}
\tag{A.15}
$$

In this reduced, the influence of the sine and cosine terms is more evident, with the first two terms acting like cosine waves which oscillate as a function of the difference between the propagator phases, $\Theta_\nu(n)$. Also visible are the contributions from the composition of the NIR electric field, through the incorporation of the l_{NIR}, r_{NIR}, & ϕ_{NIR} terms. Finally, the influence of the composition of the Bloch waves, which are described by the propagator, are present with the n_i terms.

A more physical simplification is setting either r_{NIR} or l_{NIR} to zero, which can occur in experiment by exciting the sample with either RHCP or LHCP polarization. If we set l_{NIR} to zero, the polarization takes the form

$$r^2(n) \propto \frac{1}{9}\left(e^{-2\Gamma_d \tau_{n,hh}\hbar^{-1}}\left(4+4n_z+n_z^2\right)+e^{-2\Gamma_d \tau_{n,lh}\hbar^{-1}}\left(4-4n_z+n_z^2\right)+ e^{-\Gamma_d(\tau_{n,hh}+\tau_{n,lh})\hbar^{-1}}\left(4-n_z^2\right)\cos\left(\Theta_{hh}(n)-\Theta_{lh}(n)\right)\right) \quad \text{(A.16)}$$

From this, we can see how the difference in acceleration time of the two quasiparticles, manifest in the damped exponential term, coupled with the difference in phase of the two quasiparticles, contained in the cosine term, lead to a change in sideband polarization as a function of sideband order. This matches the behavior observed in experiment when we excite with fully RHCP light.

The calculation of the left handed component of the sideband field is similar, and left as an exercise to the reader. With a calculation of the form of the left handed component, using the condition $l^2(n)+r^2(n)=1$ can be used to convert the expressions in equations A.13-16 from proportionalities to equivalencies. If we express the acceleration times in the exponential terms as $\tau_{hh}+\tau_{lh}=\tau_n$, $2\tau_{hh}=\tau_n+\tau_\Delta$, $2\tau_{lh}=\tau_n-\tau_\Delta$, and use the relation $r_{NIR}^2+l_{NIR}^2=1$, we can simplify the expression for $r^2(n)+l^2(n)$ to.

$$
\begin{aligned}
&r^2(n) + l^2(n) = \\
&\frac{\beta^2}{9} e^{-\Gamma_d \tau_n/\hbar} \Bigg[e^{-\Gamma_d \tau_\Delta/\hbar} \Big((2+n_z)^2 + 3(n_x^2 + n_y^2) + \dots \\
&\qquad 4\sqrt{3}(2+n_z)(n_x \cos\phi_{NIR} - n_y \sin\phi_{NIR}) r_{NIR} l_{NIR} \Big) + \dots \\
&\qquad e^{\Gamma_d \tau_\Delta/\hbar} \Big((2-n_z)^2 + 3(n_x^2 + n_y^2) + \dots \\
&\qquad 4\sqrt{3}(2-n_z)(n_x \cos\phi_{NIR} - n_y \sin\phi_{NIR}) r_{NIR} l_{NIR} \Big) + \dots \\
&\qquad \Big(4\sqrt{3}(1+n_z)(n_x \cos\phi_{NIR} - n_y \sin\phi_{NIR}) r_{NIR} l_{NIR} + \dots \\
&\qquad 4 - n_z^2 + 3(n_x^2 + n_y^2) \Big) \cos\left(\Theta_{hh}(n) - \Theta_{lh}(n)\right) + \dots \\
&\qquad 4\sqrt{3}(1-n_z)(n_x \cos\phi_{NIR} - n_y \sin\phi_{NIR}) \sin\left(\Theta_{hh}(n) - \Theta_{lh}(n)\right) \Bigg]
\end{aligned}
\tag{A.17}
$$

Here the β term is used as a normalization constant such that $r^2(n) + l^2(n) = 1$. Using hyperbolic sines and cosines for the τ_Δ exponentials, and the relation $n_z^2 + n_y^2 + n_x^2 = 1$, Equation A.17 simplifies to

$$
\begin{aligned}
&r^2(n) + l^2(n) = \\
&\frac{\beta^2}{9} e^{-\Gamma_d \tau_n/\hbar} \Bigg[\cosh(\Gamma_d \tau_\Delta/\hbar) \Big(7 - 2n_z^2 + 8\sqrt{3}(n_x \cos\phi_{NIR} - n_y \sin\phi_{NIR}) r_{NIR} l_{NIR} \Big) + \dots \\
&\qquad \sinh(\Gamma_d \tau_\Delta/\hbar) \Big(4n_z(1+\sqrt{3})(n_x \cos\phi_{NIR} - n_y \sin\phi_{NIR}) r_{NIR} l_{NIR} \Big) + \dots \\
&\qquad \Big(4\sqrt{3}(1+n_z)(n_x \cos\phi_{NIR} - n_y \sin\phi_{NIR}) r_{NIR} l_{NIR} + \dots \\
&\qquad 7 - 4n_z^2 + \Big) \cos\left(\Theta_{hh}(n) - \Theta_{lh}(n)\right) + \dots \\
&\qquad 4\sqrt{3}(1-n_z)(n_x \cos\phi_{NIR} - n_y \sin\phi_{NIR}) \sin\left(\Theta_{hh}(n) - \Theta_{lh}(n)\right) \Bigg]
\end{aligned}
\tag{A.18}
$$

Again, this general case is more complicated than specific instances, such as r_{NIR} or $l_{NIR} = 0$, in which case

$$\beta^{-2} = 9e^{-\Gamma_d \tau_n/\hbar}\left[2\cosh(\Gamma_d \tau_\Delta)(7 - 2n_z) + (7 - 4n_z^2\cos\left(\Theta_{hh}(n) - \Theta_{lh}(n)\right)\right] \quad \text{(A.19)}$$

Which results in

(A.20)

$$r^2(n) = \left[2\cosh(\Gamma_d \tau_\Delta/\hbar)(4 + n + {}_z^2) + 8n_z\sinh(\Gamma_d \tau_\Delta/\hbar) + (4 - n_z^2)\cos\left(\Theta_{hh}(n) - \Theta_{lh}(n)\right)\right] \cdot \left[2\cosh(\Gamma_d \tau_\Delta/\hbar)(7 - 2n_z^2) + (7 - 4n_z^2)\cos\left(\Theta_{hh}(n) - \Theta_{lh}(n)\right)\right]^{-1}$$

From these calculations, we can see how we get the specific form of the sideband polarization field from the quasiparticle propagator, arriving at a specific analytical expression dependent on experimental and material parameters, present in the $n_i, \tau_{n\nu}$, & $\Theta_\nu(n)$ terms.

The calculation of the phase of the electric field is beyond the current scope of this thesis, and the topic of future works. In addition, the calculation of derivatives of these expressions will be useful for future analysis, where the dependence on other parameters like the NIR wavelength or the THz to crystal axis orientation could be used to fit material parameters of the quasiparticle-crystal system. As data from Chapter's 4 through 6 demonstrate, this observed sideband polarization changes with different material and experimental parameters, can can be connected to how $\Theta_\nu(n)$ changes with different parameters through derivates. In this way we can fully leverage the analytical nature of our model for sideband polarization and quasiparticle propagation.